Institute of Low Temperature and Structure Research PAS

Doctoral dissertation

Preparation and investigation of spectroscopic properties of $YXZO_4$, where X and Z - P^{5+}, V^{5+}, As^{5+}, doped with rare-earth ions and co-doped with s^2 type ions

Author

M.Sc. Marta Kardach

Supervisor

Prof. dr hab. Rafał J. Wiglusz

Co-supervisor

Dr. Adam Watras

Wroclaw 2023

Acknowledgments

To the supervisor, prof. dr hab. Rafał J. Wiglusz, for the support and assistance in conducting the research, analysing the results, and with writing the scientific articles.

To the co-supervisor, dr Adam Watras, for the insight and support in conducting the research, analysing the results, and with writing the scientific articles. For the scientific collaboration that inspired me to pursue doctoral studies.

To the research team for the kindness, support, and advice in many aspects of life, not just the academic one. The time spent in the always-warm Miami atmosphere will forever put a smile on my face.

To the staff and Ph.D. students of the Division of Biomedical Physicochemistry and the Division of Optical Spectroscopy.

To all the co-authors of scientific publications and the people whose contribution made their creation possible. Especially to Prof. Philippe Boutinaud of the University of Clermont Auvergne in Clermont-Ferrand, France.

To my immediate family, without you, this moment would not have happened.

To my dear husband Michal, you always believed in me and encouraged me. It is all thanks to you and for you.

To the project, *Multidisciplinary doctoral studies – nanotechnology in biomedicine* project with the National Centre for Research and Development, POWR.03.02.00-00-I030/17-00 for the financial support

To the project*, Preparation and modulation of spectroscopic properties of $YXZO_4$, where X and Z – P^{5+}, V^{5+}, As^{5+}, doped with 's^2-like' ions and co-doped with rare earth ions*, OPUS 17, UMO-2019/33/B/ST5/02247, for the financial support

Contents

The aim of the study

The research study aimed to obtain and characterise the physicochemical properties of the materials series with a general formula of $YXZO_4$ where X and Z are arsenic, phosphorus, and vanadium elements. The obtained materials were doped with rare-earth ions and s^2-type ions. Particular attention was paid to the studied materials' characterisation of the spectroscopic properties. Additionally, the influence of the matrix composition on the dopant luminescent properties was researched.

Yttrium orthovanadate, yttrium orthovanadate-arsenate, and yttrium orthovanadate-phosphate belong to the$YXZO_4$ compound group. The matrices were doped with optically active ions Eu^{3+}, Tb^{3+}, Er^{3+}-Yb^{3+} pair, Tm^{3+}-Yb^{3+}, and Eu^{3+}-Bi^{3+} pairs, respectively. The co-precipitation method was chosen as the synthesis of each listed compound. The conditions and description of the synthesis route are included in each scientific publications accompanying this dissertation.

The following research techniques were used to achieve the intended purpose: X-ray diffraction – for crystal structure analysis, the scanning electron microscopy and transmission electron microscopy – for the morphology, size and agglomeration analysis, the inductively coupled plasma – optical emission spectroscopy – for the elemental composition confirmation, the optical spectroscopy techniques – for structure analysis (infrared spectroscopy) and luminescent properties (emission excitation, emission and luminescence lifetimes).

The base of the dissertation is four thematically coherent scientific articles. These articles have been published in respected international scientific journals with an impact factor from 4.177 to 6.371. The thesis consists of a theoretical and experimental introduction being an overview and a statement of the current state of science in the subject matter of this thesis. In this dissertation, in the form of four scientific articles an in-depth analysis of the physicochemical properties of the obtained $YXZO_4$ materials are presented. The first focuses on YVO_4 doped with Eu^{3+} ions, the synthesis process optimization, and the synthesis impact on the spectroscopic properties. The second article encompasses the influence of changing the arsenic-to-vanadium ratio in $YV_xAs_{1-x}O_4$ and its effect on the quenching process of the Tb^{3+} ions luminescence. The third and fourth articles focus on the $YV_xP_{1-x}O_4$ matrix, the occurring structural changes and their influence on the dopant luminescent properties. The third article concentrates on the up-conversion processes between two sets of up-converting pairs of Er-Yb

and Tm-Yb ions. The fourth and final article includes an analysis of energy transfers between optically active ions V-Bi-Eu and the emission in the room and liquid helium temperatures.

Introduction

Inorganic $REXO_4$ compounds

The inorganic $REAsO_4$, $REVO_4$, and $REPO_4$ compounds are found in nature in form of eleven minerals. Among them are monazites-(La), -(Ce), -(Nd), -(Sm), gasparite-(Ce), two xenotimes-(Y), -(Yb), pretulite-(Sc), chernovite-(Y), and two wakefieldites-(Y), -(Ce). These minerals crystallize with the monazite-type monoclinic system in the $P2_1/n$ space group or with the zircon-type tetragonal system in the $I4_1/amd$ space group symmetry. [1]

In comparison to the number of publications on vanadates and phosphates, relatively few papers describe the structural and physico-chemical properties of $REAsO_4$. The search engine built in scopus.com website provides 5,388 results for the phrase "YVO_4", 698 results for "YPO_4" and only 29 results for "$YAsO_4$". The zircon-type structure is observed in the case of Y, Sc, Sm – Lu. [2,3] The monazite-type structure is observed for La-, Ce-, Pr-, and $NdAsO_4$. [3,4]

$REPO_4$ crystalizes with two crystalline structures, monazite- and zircon-type. The crystal structure depends on the RE ion size. Large rare earth ions cause crystallization with the monazite-type structure. Small rare earth ions (Y^{3+}, Sc^{3+}) cause crystallization with a zircon-type structure. [3] In the case of $GdPO_4$, $TbPO_4$, $DyPO_4$, and $HoPO_4$, two crystalline forms are observed. The structure of monazite is referred to as metastable for $DyPO_4$ and $TbPO_4$, while the stable form is zircon-type that is also often observed after additional heat-treatment.

$REVO_4$ compounds mostly crystallize with the zircon-type structure. It is reported that La-, Ce-, Pr-, and $NdVO_4$ can be synthesized with a monazite-type structure. [3]

Yttrium orthoarsenates

Sparse publications have been found on the spectroscopic properties of $YAsO_4$. Despite its well-studied crystallographic structure, the compound has not gained popularity among researchers to such an extent as other compounds in the YXO_4 group, namely YPO_4 or YVO_4.

Yttrium orthoarsenate crystallizes in a zircon-type tetragonal system with $I4_1/amd$ space group symmetry. The $YAsO_4$ unit cell consists of two Y^{3+} ions and two AsO_4^{3-} groups. [5] With

the doping of the crystallographic structure, Y^{3+} ions are statistically replaced by RE^{3+} ions in D_{2d} site.

For the first time, nanocrystalline $YAsO_4$ doped with Eu^{3+} ions was obtained by R.J. Wiglusz et al. [2] via the precipitation synthesis method. The researchers conducted a thorough study of the effect of $YAsO_4$ structure and dopant ion concentration on emission. Herein, the Eu^{3+} ions were applied as a luminescent probe and indicated change in the local chemical environment by lowering the point symmetry.

Continuing the research on the spectroscopic properties of nanocrystalline yttrium orthoarsenate is crucial. It is necessary to the further understand the occurring physico-chemical changes.

Yttrium orthophosphates

Yttrium orthophosphate gained immense popularity as a matrix for RE^{3+} luminescence investigation. Nanocrystalline YPO_4 can be synthesised via multiple synthesis routes: precipitation [6,7], the sol-gel method [8], the microemulsion synthesis [9], and hydrothermal method [10].

L. van Pieterson contributed to the popularity of yttrium orthophosphate by describing the $4f^n \rightarrow 4f^{n-1}5d$ transitions for light- [11] and heavy-lanthanides (Tb^{3+}, Dy^{3+}, Ho^{3+}, Er^{3+}, Tm^{3+}, and Yb^{3+}) [12] in YPO_4, in the VUV part of the spectrum (100-250 nm). Additionally, much interest in yttrium orthophosphate was brought about by the 1967 work of G. Blasse and A. Bril on energy transfers between Sb^{3+}, Bi^{3+}, Ce^{3+} and Sm^{3+}, Eu^{3+}, Tb^{3+}, Dy^{3+} ions [13].

Yttrium orthophosphates can find potential applications as, i.e.: persistent luminescence phosphors [14], bimodal optical sensors for nanothermometry and nanomanometry [15], and fluorescent labels [16].

Yttrium orthovanadates

Yttrium orthovanadates, similarly to yttrium orthophosphates, have been a topic of many scientific papers. The wide range of applications, especially the initial use of YVO_4 as effective laser materials [17–22], and red-emitting phosphor for cathode-ray tubes and plasma screens

[23], has contributed to the current level of interest in YVO_4. Nowadays, YVO_4 doped materials are applied in, i.e., drug delivery systems [24], optical bioprobes [25], light-emitting diodes [26], sub-tissue heating and thermal sensing [27], as well as thermal and pressure sensing [28].

Nanocrystalline YVO_4 can be obtained via multiple synthesis routes: precipitation [29], the modified Pechini's method [30], hydrothermal method [31], solvothermal method [32], and microemulsion [33]. It was found that with changing synthesis conditions a variety of yttrium orthovanadate particles's shapes and sizes can be obtained. The pH of the synthesis medium is especially important. [34] The variation of the pH leads to obtaining tailored sizes of individual particles. A lower number of nucleation sites occurs in acidic pH. Hence, particles are typically larger in acidic pH conditions. Additionally, nucleation and growth of the nanocrystal can be influenced by organic solvents. The particles's shapes and sizes depend on the applied solvent. [34]

Yttrium orthovanadate shows an absorption peak in the UV spectral region with a maximum of about 320 nm. Upon the NUV excitation YVO_4 broad emission peak is observed at around 450 - 475 nm. The VO_4^{3-} groups are responsible for this emission. [35] Additionally, this emission band is temperature dependent and becomes prominent in low temperatures. [36,37]

Solid solution compounds

The solid solution (or solid-state solution) consists of isostructural compounds with a basic formula of $A_{1-x}B_x$. The principle defining the changes occurring in the crystal structure of the solid solutions, at a constant temperature, were postulated by Lars Vegard in 1921. [38] Vegard stated that the lattice parameters of the new compound change linearly with respect to the continuous substitution of element A with element B:

$$l(A_{1-x}B_x) = (1-x)l_A + xl_B = l_A + x(l_B - l_A) \quad (1)$$

where l_A – lattice parameter of element A (solvent), l_B – lattice parameter of element B (dissolvent), x – the concentration of element B. This law assumes a statistical substitution of element A for element B. The additivity principle of molecular volumes is omitted in the case of Vegard's law. The deviations from the Vegard's law have been noted. Nevertheless, it does not deny the emergence of solid solutions with a continuous variation in $A_{1-x}B_x$ structure. Moreover, positive and negative deviations from the law are observed. [39] The deviation from

the Vegard's law may stem from: atomic size, valence electron density, electrochemical potential divergences, Brillouin zone effects, and unit cell volumes. [40] For some solid solutions, atomic size mismatches can be diminished by positive interactions between elements. This can result in compatibility under Vegard's law. [41]

By the number of papers published about the solid solutions of $YXZO_4$, where X and Z are As, P, and V, it can be stated that there is a scope for research to accurately determine the physicochemical properties of such systems. On the contrary, an immense interest is being put in YVO_4, YPO_4 doped and codoped with RE or transition metals. Thus, it is desirable to know and describe the physicochemical properties of continuous solid solutions with variable X and Z ions. For the $YV_{1-x}P_xO_4$ system doped with europium ions T. Minakova et al. [42] showed a shift of XRD peaks toward larger angles and confirmed the formation of the $YV_{0.9}P_{0.1}O_4:Eu^{3+}$ and $YV_{0.8}P_{0.2}O_4: Eu^{3+}$ solid solutions. G. Pan et al. [43] observed the XRD peak broadening for solid solutions that indicates a structural disorder created by the statistical substitution of the (VO_4) group with the (PO_4) one, caused by the ion size mismatch between V^{5+} and P^{5+} ions. It was shown, that the occurring structural changes led to visible alterations in the luminescence properties. Additionally, E. Cavalli et al. presented a paper on $YV_{1-x}P_xO_4$ complete solid solutions doped with Bi^{3+} ions. [44] Herein, the luminescence properties were influenced by the structural surrounding of the optically active ion. Thus, it is important to continue the research and proceed with a thorough analysis of the continuous solid solution impact on the luminescence properties of different optically active ions.

Nanomaterials

The term "nanomaterials" is used for materials with building blocks are particles, with one of their dimensions being up to 100 nm. Based on dimensionality, nanomaterials can be divided into four categories: zero-dimensional (0-D), one-dimensional (1-D), two-dimensional (2-D), and three-dimensional (3-D). In zero-dimensional nanomaterials, e.g., quantum dots, each dimension is expressed in nanometres. In one-dimensional nanomaterials (e.g., nanotubes), one is nanometric, and the other two are arbitrary. In two-dimensional nanomaterials (e.g., nanowires), only two dimensions are nanometric. In three-dimensional nanomaterials (e.g. core-shell systems or nanocomposites), each dimension exceeds 100 nm and the material consists of various 0-D, 1-D, or 2-D structures. [45]

The interest in research, development, and application of nanomaterials is due to their unique properties. The material's properties remain the same with reducing the size from bulk to micrometric. In contrast, a drastic change in the physical and chemical properties of the material occurs when the size changes from micro to nano.

In the case of nanometric materials, the external surface area of the material is significantly larger when compared to the volume of the particle. The development and modification of the surface have led to an increased interest in the use of nanomaterials, i.e., catalysts or adsorbents, as the shape and size of the particles can influence the activation energy, turnover rates, and selectivity. [46] With the change in size and morphology of a particle its photoluminescent properties can be modulated. It is important to underline the impact of the surface states.

When the size of an individual nanoparticle decreases, two so-called size effects can be distinguished. The first one concerns the comparability of the particle's size to the exciton Bohr radius and the exhibiting electron's confinement inside this particle, then the quantisation of the electron motion occurs. The quantum size effect is observed for particle sizes ranging from 10 Å to several hundred Å. [47] The second concern is the ratio of atoms making up the surface-to-volume atoms of the particle. To some extent this effect is scalable. [48]

To obtain nanoparticles with tailored physicochemical properties a set of sophisticated synthesis methods is utilized. The synthesis route needs to provide good-quality nanomaterials while being reproducible. Consequently, methods of synthesis that provide continuous control of process conditions, and the ability to modify materials during the process, are of great interest. Nanomaterials can be obtained via two general pathways, top-down and bottom-up. In the top-down technique, nanoparticles are obtained by grinding or other solid material decomposition processes. In the bottom-up technique, the nanomaterial is created by a chemical reaction or assembling of atoms or molecules. Additionally, the nanoparticles synthesis methods can be divided into: physical, biological, and chemical techniques. [49] The Following chemical routes have been used to obtain the nanomaterials: solvothermal synthesis [50,51], microwave-assisted hydrothermal synthesis [52,53], the sol-gel synthesis [54,55], the microemulsion technique [56,57], the co-precipitation synthesis [58,59] or the continuous flow technique [60,61].

Luminescence of lanthanide ions

The lanthanide period includes fifteen chemical elements from lanthanum (^{57}La) to lutetium (^{71}Lu). One may also encounter the term "rare earth elements" applied to grouping lanthanides with two elements from the scandium group, yttrium (^{39}Y) and scandium (^{21}Sc). The common name of rare earth elements originated from the coexistence of these elements in nature as minerals. In the periodic table, lanthanides occupy the *f*-block. Excluding promethium, lanthanides have stable isotopes and are not classified as radioactive. Lanthanide ions appear mainly in the 3rd oxidation state, with exceptions occurring in the 2nd (Eu, Nd, Pm, Sm, Tm, Yb) or the 4th (Ce, Dy, Pr, Tb) oxidation states. Hence, the most common electronic configuration for RE^{3+} ions is [Xe]$4f^{n-1}$. The 4*f* valence orbitals are nested in the ion core, shielded by the filled 5*s* and 5*p* outer orbitals.

In polyelectron atoms or ions, the electron states are ascribed via terms. Terms for an atom with *i* electrons are defined with quantum numbers in the following format:

$$^{2S+1}L_J, \tag{2}$$

$$S = \sum_i s_i,\ s_i = 1/2, \tag{3}$$

$$L = \sum_i l,\ M_L = -L, \dots, L, \tag{4}$$

$$J = L + S, L + S - 1, \dots, |L - S|. \tag{5}$$

where S – the total spin angular momentum quantum number, s – the spin quantum number, L – the total orbital angular momentum quantum number, M_L – the total magnetic orbital angular momentum, and J – the spin-orbit coupling [62]

With the following Hund rules the ground states of the lanthanide ions can be determined. The ground state is the one with:

- the largest total spin angular momentum (S) and the quantum number S can take half-integer or integer values.
- the largest orbital angular momentum (L) and the quantum number L takes only integer values assigned to a letter of the Latin alphabet, e. g., $S = 0$, $P = 1$, $D = 2$, $F = 3$, $G = 4$.
- if the valance electron shell is:

- not half-filled, the total angular momentum takes on the smallest value: $J=|L+S|$.
- more than half-filled, the total angular momentum takes on the highest value: $J=|L+S|$.

According to Laporte's parity rule intraconfigurational 4*f*-4*f* transitions are forbidden. If the parity between the transitions with respect to the inversion centre is not conserved, the transition is allowed. The electronic transition must follow the spin rule, where the spin of excited and ground states remains unchanged. For several lanthanide ions, the change in spin accompanies the 4*f*-4*f* transition. However, this rule is relaxed by the spin-orbit coupling. [62,63] The inner 4*f*-4*f* transitions are of electric dipole (ED), magnetic dipole (MD), or electric quadrupole (EQ). The ED transition is an odd parity transition, contrary to the MD and EQ transitions, which are of even parity. The intensity of the transition is the lowest for the electronic quadrupole. When RE^{3+} ions are doped in a solid matrix, the spherical symmetry is broken. Additionally, if the crystal structure of the matrix does not have an inversion centre the interactions between orbitals occur and partially mix. Therefore, the parity rule is somewhat relaxed and an electric dipole transition becomes allowed. In this case the "forced dipole transition" term is used. The intensity of this transition is lower by orders of magnitude in comparison to the allowed electric dipole transitions. [64] Dieke's scheme of the energy levels of the lanthanide ions is presented in Figure 1. [65] The structure of the energy levels was computed for lanthanum fluoride as the matrix material. The specified levels allow for an accurate analysis of the experimental results despite the use of other matrices, as the values remain almost constant. [66]

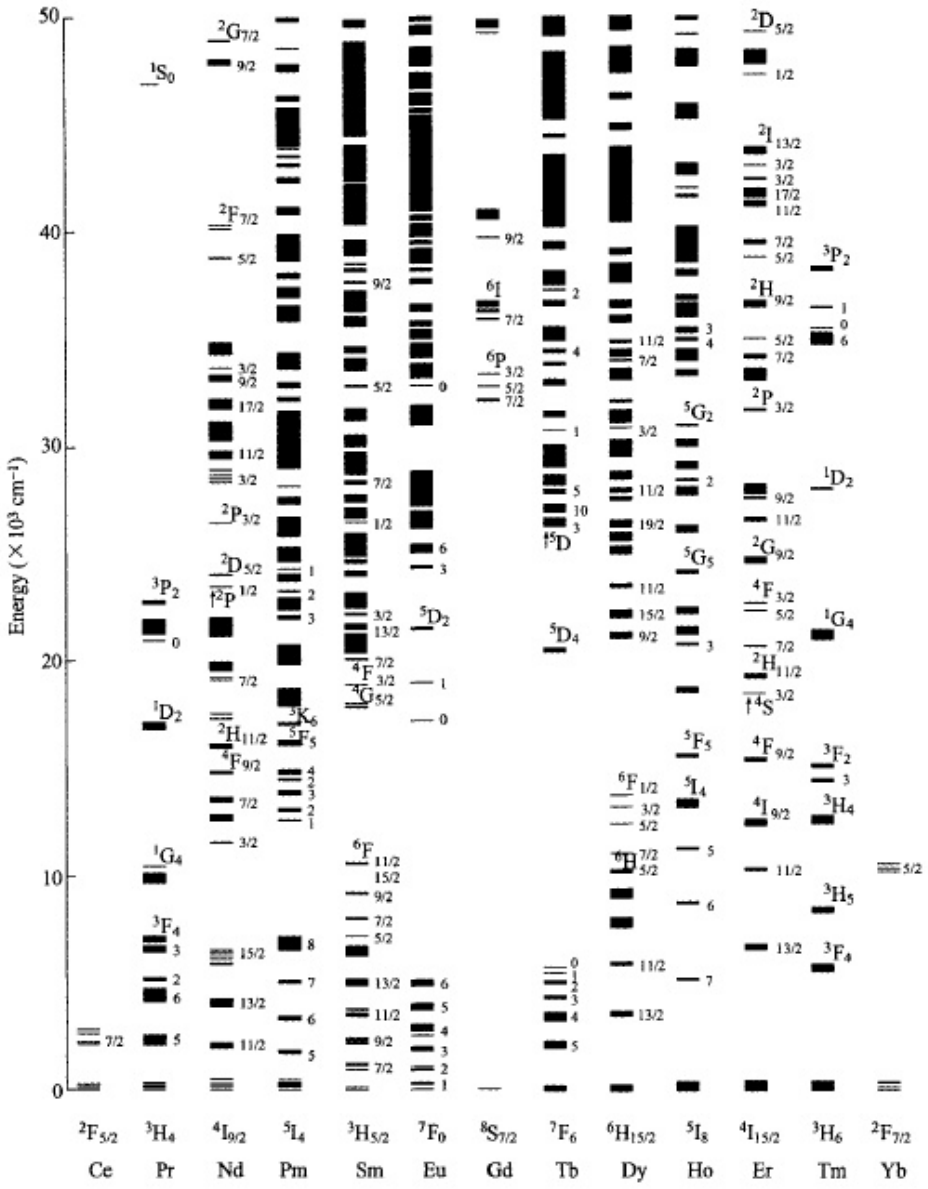

Figure 1. The energy levels scheme of RE^{3+} ions: LaF_3. [65]

The interconfigurational 4*f*-5*d* transitions in lanthanide ions are allowed by Laporte's parity selection rule. When compared to 4*f*-4*f* transitions, 4*f*-5*d* appear much broader. As mentioned previously, the 5*d* orbitals are the outer orbitals shielding 4*f* orbitals. Hence, 5*d* orbital is sensitive to crystal-site symmetry changes and interacts with the ligand. The 4*f*-5*d* transitions are the high-energy transitions. In the literature the most observed ones are those of Ce^{3+}, Pr^{3+}, and Tb^{3+} ions. The energies of their 4*f*-5*d* transitions are the lowest out of all the lanthanide ions. [67]

The charge transfer (CT) transitions are high-energy allowed transitions and can be divided into ligand-metal charge transfer (LMCT), metal-ligand charge transfer (MLCT), or

metal-metal charge transfer (MMCT). These transitions are often used as a pathway for sensitization of lanthanide ions luminescence. As mentioned before, the intensity of the forced dipole transition is very low. For this reason, alternative routes of luminescence excitation are considered. The charge transfer efficiency can be affected by competitive non-radiative processes, for example back energy transfer. The energy transfers between lanthanide ions constitute a topic of ongoing research [68] and occur between, i.e., Ce^{3+}-Tb^{3+}, Tb^{3+}-Eu^{3+}, Tm^{3+}-Dy^{3+}, Sm^{3+}-Eu^{3+}, Ce^{3+}-Dy^{3+}, Ce^{3+}-Nd^{3+}, and Ho^{3+}-Yb^{3+}, Er^{3+}-Yb^{3+}, Tm^{3+}-Yb^{3+}.

If one were to design an ideal system containing all lanthanide ions, an emission spectrum with peaks spanning the entire UV-Vis-NIR spectrum would be obtained. The exceptions are La^{3+} and Lu^{3+} which are not luminescent. The emission peaks of the lanthanide ions have narrow bands and small Stokes shifts.

Europium ions luminescence

The europium element classifies as a light lanthanide. Upon excitation with UV radiation, it exhibits strong red luminescence, with emission lines in the 575 – 725 nm spectral range. The photoluminescent properties of Eu^{3+} ions have been researched in multiple inorganic matrices, organic complexes as well as glasses. A careful evaluation of both the shape and intensity of the lines in the absorption and emission spectra is extremely important. The apparent changes may indicate disruptions in the local crystallographic environment surrounding the europium ion in the matrix. Spectroscopic measurements of the Eu^{3+} ion carry a plethora of information. Therefore, the ion has gained popularity and wide range of applications. [69–76]

Europium ion (Eu^{3+}) has [Xe]$4f^6$ electronic configuration, and the $4f$ orbital is shielded by $5s^2$ and $5p^6$ outer orbitals. Europium doped compounds present intense red emission due to the ${}^5D_0 \rightarrow {}^7F_J$ transitions, where $J = 0, 1, 2, 3, 4, 5, 6$. The commonly observed in the Vis part of spectrum are the ${}^5D_0 \rightarrow {}^7F_{0,1,2,3,4}$ transitions. Additionally, transitions from other Eu^{3+} excited states can be observed. These are the higher excitation states: ${}^5D_1$, ${}^5D_2$ and ${}^5D_3$. Nevertheless, the spectral lines corresponding to the transitions from these states are not as commonly observed as the ones from the lower ${}^5D_0$ state. Two types of transitions occur in Eu^{3+} ions the forced electric dipole (ED) transitions (the ${}^5D_0 \rightarrow {}^7F_{0,2,3,4}$) and the magnetic dipole (MD) transition (the ${}^5D_0 \rightarrow {}^7F_1$). The intensity of the ${}^5D_0 \rightarrow {}^7F_1$ MD transition is mainly independent of the crystal site symmetry, as its intensity appears strong. The ED transitions are influenced

by the environment. The $^5D_0 \rightarrow {}^7F_0$ transition is rarely observed, only in C_n, C_{nv} and C_s symmetries. [77] The $^5D_0 \rightarrow {}^7F_2$ transition is a very strong transition classified as hypersensitive. There is a significant environmental impact on the shape and intensity of this transition. The intensity of the $^5D_0 \rightarrow {}^7F_3$ is very weak, as it is a forbidden transition. Although, the $^5D_0 \rightarrow {}^7F_4$ transition, is not classified as a hypersensitive transition, it is also affected by the environment. The intensity of this transition is medium to strong.

Visible in the excitation spectra, the $^7F_0 \rightarrow {}^5L_6$ transition having its maximum at about 397 nm is the most intense transition of the europium(III) ions. This transition is most used for the direct excitation into the *f* terms of Eu^{3+} ions.

Although, as mentioned before, Eu^{3+} ions red emission can be efficient compared to other lanthanide ions, many researchers seek after the highest possible efficiencies.. To overcome the problems associated with the poor light absorption of lanthanide ions, co-doping with other optically active ions that are specific luminescence sensitizers is used. As Eu^{3+} sensitizers Bi^{3+} [13,78,79] and Pb^{2+} [80,81] ions can be used.

Terbium ions luminescence

The terbium element is classified as a heavy lanthanide. Upon excitation with UV or near UV radiation, it exhibits green luminescence, with emission lines in the 450 – 650 nm spectral range. The photoluminescent properties of Tb^{3+} ions have been researched in various inorganic [82–84] and organic matrices [85,86], and glass [87,88].

The standard emission excitation spectrum of Tb^{3+} ions in an inorganic matrix consists of $4f^8$-$4f^7 5d^1$ at around 240-280 nm, and at slightly lower energies the 4*f*-4*f* transitions occur: the $^7F_6 \rightarrow {}^5H_7$, the $^7F_6 \rightarrow {}^5L_7$, the $^7F_6 \rightarrow {}^5L_8$, the $^7F_6 \rightarrow {}^5L_9$, the $^7F_6 \rightarrow {}^5D_3$, and the $^7F_6 \rightarrow {}^5D_4$.

Most commonly, upon 375 nm excitation, the emission spectra of Tb^{3+} ions consist of the $^5D_4 \rightarrow {}^7F_J$ transitions, where $J = 3, 4, 5, 6$. Additionally, the $^5D_3 \rightarrow {}^7F_{5,4}$ transitions can be observed, but with substantially lower intensity. Typically, the most intense transition is the $^5D_4 \rightarrow {}^7F_5$ with its maxima at 545 nm. [89]

Up-conversion luminescence

Up-conversion luminescence involves the emission of a photon with significantly higher energy than that carried by the incident photon. Schematically, the UC process can be characterised as a transition between three states. The first state is the ground state and the next two are two consecutive excited metastable states. This process is observed when the energy difference between the ground state and the first excited state, and the energy difference between the first excited state and the second excited state are equivalent. In addition, the lifetime of the first excited state must be adequate for further excitation to take place, as radiation-free relaxation to the ground state cannot occur during this time. The up-conversion process can occur not only within one ion, but also between two different types of ions. When two ions are involved in the up-conversion process, one ion plays the role of the sensitizer and the other of the activator. In addition to those mentioned, new requirements must be met if ions of two different elements are used. The first is the degree of spectral overlap between the sensitizer's emission band and the activator's absorption band. The second is the ratio between and the sensitizer and the activator content in the matrix, because non-radiative energy transfer requires shorter distances between two ions compared to radiative energy transfer. The up-conversion processes include energy transfer up-conversion (ETU), excited state absorption (ESA), cooperative sensitization up-conversion, and photon avalanche (PA). The two ion pairs most used for up-conversion process generation are Er^{3+}-Yb^{3+} and Tm^{3+}-Yb^{3+}. These two ion pairs have gained popularity for being the most effective. Excluding the photon avalanche (PA), the up-conversion processes in general are highly inefficient. [90]

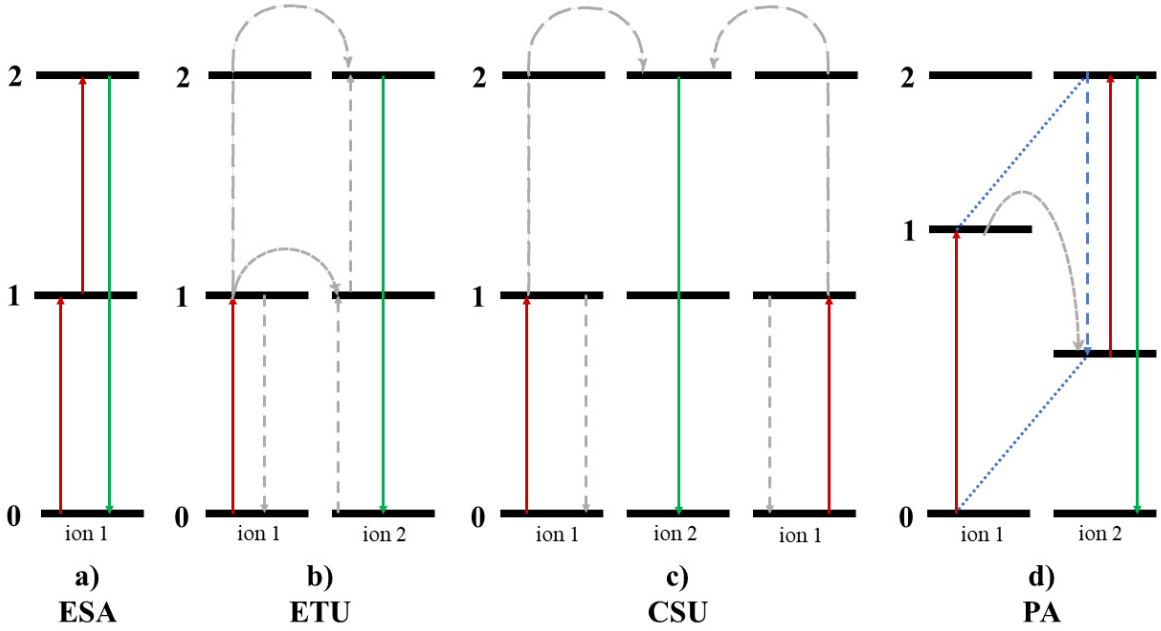

Figure 2. Up-conversion processes: Excited State Absorption (a), Energy Transfer Up-conversion (b), Cooperative Sensitization Up-conversion (c), and Photon Avalanche (d).

The "excited state absorption" (ESA) (Figure 2a) process name coincides with the mechanism, that involves the successive absorption of the *n* photons by *n* subsequent states (1, 2) in one ion. The subsequent excited states (1, 2) must be equidistant by an identical energy value. This process occurs in ions with evenly spaced terms, a ladder-like structure, i.e., Er^{3+}, Ho^{3+}, Nd^{3+}, and Tm^{3+} ions. [91]

The energy transfer up-conversion (ETU) (Figure 2b) involves two ions, sensitizer (ion 1) and activator (ion 2). The sensitizer is excited from a ground state (0) to a metastable state (1). Subsequently, the energy is transferred to the activator, causing its excitation to first excited state (1). While the sensitizer (ion 1) simultaneously returns to the ground state. Finally emission occurs within the activator (ion 2). This process occurs between, i.e., Ho^{3+}-Yb^{3+}, Er^{3+}-Yb^{3+} pairs (ions).

The cooperative sensitization up-conversion (CSU) (Figure 2c) process similarly to ETU occurs between two different ions (ion 1 and ion 2). The incident beam causes two ions of the same element (ion 1) to be simultaneously excited from the ground state to an excited state (1). Thereafter, the energy of the two excited states is somewhat combined and transferred to the activator's ion (ion 2), causing its direct excitation to a higher energy excited state (2). Activator emits high energy photon, while returning to the ground state.

Photon avalanche (PA) (Figure 2d) involves series of ESA and the cross-relaxation processes occurring between ions of the same element. For the cross-relaxation phenomenon to take place, the ions must be near each other in the crystallographic structure. Hence, the concentration of the optically active ion is crucial. The PA process begins with the ground state absorption within one of the ions (ion 1). Through the cross-relaxation energy is transferred to different ion (ion 2) causing population of the first excited state (1), while ion 1 returns to the ground state. The second excited (2) state of ion 2 is populated by ESA process. The process can looped until all of the ion 2 types are in the same excited state.

Luminescence of s^2 type ions

The ns^2 group includes transition metal ions such as Bi^{3+} ($6s^2$), Pb^{2+} ($6s^2$), Sb^{3+} ($5s^2$), and Tl^{+} ($6s^2$). When free ions with electron confluence s^2 are concerned, the ground state $^1S_0$ and subsequent excited states with increasing energy: $^3P_0$, $^3P_1$, $^3P_2$ and $^1P_1$ are observed. The $^1S_0 \rightarrow {}^3P_0$ transition is strictly forbidden. The occurrence of the transitions to two following excitation states ($^1S_0 \rightarrow {}^3P_{1,2}$) is based on the spin-orbit mixing. [92] The high energy transition, the $^1S_0 \rightarrow {}^1P_1$, is a spin-allowed transition. The emission spectra of s^2 ions are temperature-dependent. At low temperatures, the $^1S_0 \rightarrow {}^3P_0$ forbidden transition is detectable [93], but with increasing temperature the emission from the $^3P_1$ level becomes dominant. The photoluminescent properties of the s^2 ions emission depends on the applied matrix and site symmetry. The $6s^2$ ions (i.e. Bi^{3+} ion) occupy octahedral or preferentially asymmetric coordination. [94] Additionally, absorption bands derived from the CT transition from the host material's metal to the s^2 ion are observed. It is explained by the formation of the metal-to-metal charge transfer (MMCT) state between electronic levels of Bi^{3+} and metal ions (M^{n+}) with $d^{0\text{-}10}$ configuration. It is described as a transition from the $^1S_0$ (Bi^{3+}) ground state to the conduction band (CB) states of the host material. [95]

Experimental

This paragraph is focuses on the theory and mechanisms behind applied measurement techniques. The operating conditions and measurement ranges used to characterise the materials by the following techniques were always adjusted to the analysed material. These parameters were included in the experimental description section of each presented scientific paper accompanying the dissertation. In addition, a description of the synthesis method for each material was also included in the experimental section of each paper.

X-ray diffraction

A careful analysis of diffraction patterns of the X-rays on a material's crystal lattice and an analysis of the resulting diffractograms allows for qualitative and quantitative characterisation of the monocrystalline as well as polycrystalline materials. The use of the X-ray diffraction method makes it possible to determine the type of crystal structure of the analysed crystalline material. Each crystalline substance forms a characteristic and unambiguous diffraction pattern. Thus, by utilizing the X-ray diffraction technique, it is possible to characterise the substance as a mixture component and a pure crystalline phase. The advantage of phase analysis is that the crystalline form of a chemical compound can be unambiguously characterised rather than its elemental composition. With the XRD technique, it is possible to distinguish polymorphic varieties of the crystalline systems under investigation. X-ray powder diffraction is a fundamental technique of structural X-ray radiography, finding applications in scientific fields such as physics, chemistry, metallurgy, and materials science. By the use of X-ray powder diffraction, it is possible to determine the size of crystallites, lattice constants, phase boundaries, internal stresses, and textures. [96]

In the X-ray diffraction method, a beam of monochromatic parallel X-rays falls on a crystalline preparation. [96] The crystalline preparation can be a powder formed into thin (0.2-0.3 mm) rods or plates. [96] Incident X-rays diffract of the crystalline planes that are in position according to the Bragg equation:

$$2d_{hkl}\sin\theta = n\lambda, \tag{6}$$

where: d_{hkl} – inter-plane distance, λ – wavelength of radiation, n – diffraction order, θ – angle of reflection.

The use of a powder material leads to a differential alignment of the lattice planes, where the highest number of planes in reflective positions is observed. The reflecting position is the one in which the incident and reflected ray co-form an angle of 2θ.

A sliding scintillation counter is used to register the signal with the registration of reflections taking place gradually (one after the other). The result of the X-ray diffraction measurement is a plot of intensity as a function of angle (2θ). As a radiation source, the following lamps can be used: Co ($\lambda = 1.79$ Å), Cu ($\lambda = 1.54$ Å), Cr ($\lambda = 2.29$ Å), Fe ($\lambda = 1.94$ Å), Mo ($\lambda = 0.71$ Å).

Electron microscopy

The principle of microscope operations can be simplified to the transformation of the observed object to an image. Two types of electron microscopy techniques were used to analyse the materials scanning electron microscopy (SEM) and transmission electron microscopy (TEM). For all microscopes, parameters such as resolution, magnification, depth of field, depth of focus and lens aberration are required to be defined and specified. In the case of electron microscopy, the interaction of the electron beam with the material is of great importance.

The scanning electron microscopy (SEM) measurement involves scanning the sample with an electron beam and detecting the scattered radiation. The incident electron beam carries energy between 1 and 30 keV. Images obtained via SEM provide an information about the external structure of the material (morphology and shape), the size up to 1-20 nm and the size distribution.

The transmission electron microscopy (TEM) measurement involves detection and analysis of the electrons diffracted and transmitted through the sample. The energy of the incident electron beam is above 100 keV. Application of high energy allows for higher resolution. The transmission electron microscopy provides information about the internal structure of the material, fine structure of crystals, size and distribution. Two working modes can be differentiated for TEM: the bright-field and the dark-field. For these modes, different types of electrons are passed through the aperture. The bright-field mode is based on transmitted electrons, contrary to the dark-field mode which is based on diffracted electrons. [97]

Inductively coupled plasma - optical emission spectroscopy

The inductively coupled plasma - optical emission spectroscopy (ICP-OES) technique allows for the determination of the elemental composition. Advantages of this technique include high signal-to-background noise ratio, repeatability, high sensitivity of 0.1-100 [ng/mL] for most elements, ionisation capacity of more than 70 elements.

A liquid sample is injected into an argon plasma with a nebulizer. The analysed sample in the form of a mist reaches the plasma. Thereafter rapid drying and evaporation take place. The emission excitation is induced by collisions at high temperature (up to 10,000 K) in plasma. Further, the atomic emission is analysed. It is possible to measure a single element as well as multiple elements simultaneously (up to 70). The analytical performance of such a system is competitive in terms of measurement sensitivity and sample throughput. [98] Based on the energy carried by emitted photon rays, the elemental composition is determined. In contrast, the intensity of the signal allows the content to be determined precisely.

Infrared spectroscopy

Infrared spectroscopy allows for determination of the functional groups building structural framework of the molecules. Functional groups can be differentiated due to the absorption of the infrared radiation by chemical bonds. The absorption frequency for the functional groups remains constant regardless of the analysed material, as it depends on the geometry of the atoms, the mass of the atoms and the force constants of the chemical bonds. Therefore, by using this technique, the structural changes that occur can be identified. [99]

In order to observe the absorption of molecules, the selection rule must be fulfilled, and a change in the electric dipole moment must occur. The change in the electric dipole moment of a molecule is directly related to rotations and vibrations. The vibration movements are generally divided to stretching and bending. Further, stretching vibrations can be symmetric or asymmetric. Bending vibrations can be differentiated to deformation, rocking, twisting and wagging. Additionally bending vibrations can occur in-plane and out-of-plane. [100]

Potassium bromide (KBr) is a compound used in infrared spectroscopy technique to dilute powder materials by mixing and forming a pressed pellet. The use of potassium

bromide is supported by its significantly low infrared absorption coefficient, especially in the medium infrared spectral range from 4,000 to 400 cm^{-1}.

Photoluminescence spectroscopy

While conducting scientific research, great attention has been paid to measuring the luminescence properties of the $YXZO_4$ materials. Several measurements were carried out to thoroughly characterise the occurring processes and mechanisms through emission excitation spectra, luminescence emission, and detection of luminescence decay time profiles. In carried out measurements each setup was precisely adjusted to obtain the best signal-to-background noise ratio.

In emission spectra, the energy carried by the excitation beam is set, and the intensity of the emitted radiation is analysed by scanning the range of wavelengths using an emission monochromator. Emission spectra were collected upon excitation with a variety of wavelengths. Appropriate wavelengths were strictly correlated with the analysed material and optically active dopants. As an excitation source a pulse laser, a continuous-wave laser diode, and a xenon lamp were used. Depending on the UV-Vis-NIR light source used, the incident beam passed through a monochromator and then a set of optical lenses and filters. Thereafter, the beam interacted with analysed material and as a result, luminescence emission was scanned and further detected. If needed generated emission passed through a set of additional filters before being detected by a photomultiplier. In the end, the signal was transformed with a computer program correlated with the type of detector and (if needed) monochromator used. Each time the processed signal was obtained in the form of a spectrum with a predetermined spectral range. The emission spectra measurements were collected for different temperature conditions as well as the laser's pumping power.

The opposite mechanism occurs in emission excitation spectra. The emission monochromator is set on a specific emission wavelength. The excitation wavelength is scanned over a pre-set energy range. The spectral response of the material is measured, and a spectrum is obtained that reflects the energy levels of the system under study. Emission excitation spectra were collected for selected emission peak maxima dependent on optically active ions used in scientific papers. As an excitation source, the xenon lamp was used. Each presented spectrum was corrected for the lamp response.

An important characteristic of the luminophore is the luminescence lifetime. The luminescence lifetime corresponds to the average time the phosphor radiatively depopulates from the excited state to the ground state. A pulse laser was used to excite materials under study for the measurement of the luminescence lifetimes. The measurement setup was additionally equipped with a digital oscilloscope. Luminescence lifetime is measured as the slope of the emission intensity versus time. Experimental luminescence lifetimes measure the decay of the excited state by radiative relaxation including competing mechanisms that occur, such as energy transfers or nonradiative relaxation. Importantly, competing relaxation pathways can account for significant changes in the shape of the decay profile and reductions in luminescence lifetimes. Additionally, luminescence lifetimes can be influenced by internal chemical and structural factors.

Scientific papers included in the dissertation

Results

The dissertation includes four scientific articles included in the chapter Results. These articles were included in the dissertation submitted for review as finally published (with publisher's marks). Due to potential copyright infringement to the publisher, the submitted dissertation includes the publication "The study of the influence of pH on the structural and spectroscopic properties of nanocrystalline Eu^{3+} ion-doped yttrium orthovanadate" in the AAM (Author's Accepted Manuscript) version - i.e., the author's version accepted for publication. The published version can be found on the publisher's website: DOI: 10.1039/d0dt04052e. The other 3 publications were released under the open access model, so the dissertation includes their published versions.

P1: *The study of the influence of pH on the structural and spectroscopic properties of nanocrystalline Eu^{3+} ion-doped yttrium orthovanadate*

Marta Wujczyk, Adam Watras, Rafal J. Wiglusz

Dalton Transactions, 2021, 50, 3724
DOI: 10.1039/d0dt04052e
IF: 4.569

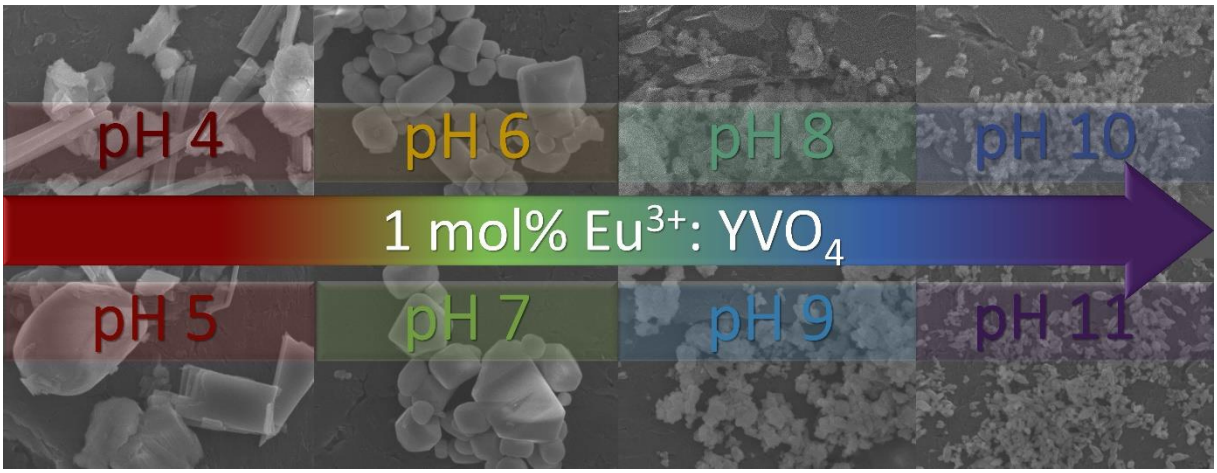

The motivation for the scientific publication entitled *"Investigating the effect of pH on the structural and spectroscopic properties of nanocrystalline yttrium orthovanadate doped with Eu^{3+} ions*" was related to optimizing the synthesis pathway and determining the connection between the colour of the resulting powder material and the synthesis conditions.

This study was aimed to investigate the physicochemical properties of the YVO_4 system in varying pH conditions. The materials were obtained via the co-precipitation method. Europium (Eu^{3+}) was chosen as a dopant, due to its properties as a luminescence probe. The use of Eu^{3+} ions would make it possible to determine changes occurring in the adjacent crystallographic structure of the optically active ion.

The co-precipitation synthesis method was applied to obtain the materials. A series of eight YVO_4: 1 mol% Eu^{3+} materials was synthesized in pH 4-11. As-prepared materials were heat-treated at 800 °C for 3 hours. A change in the colour of the powders was evident. The change in the material colour may be due to the formation of oxygen vacancies and the presence of V^{4+} ions. Therefore it was proposed that, the change in the sample's colour intensity can be correlated with the number of defects. The synthesis method used led to obtaining YVO_4 materials with a zircon-type crystallographic structure. No additional crystalline phases were observed. The SEM images were analysed for the entire series of materials. A strong correlation was observed, between the synthesis conditions and the size and shape of the particles. Based on the SEM images, an analysis of the size distribution of individual particles was performed. The materials showed a wide size distribution. The paper presents the evolution of the representative particle's shape over the broad range of pH conditions from 4 to 11. The original particle size was not preserved.

The spectroscopic properties of the materials were analysed through emission spectra collected were upon 397 nm and 266 nm excitation at room temperature. Observed was a strong dependence of the intensity in relation to the pH. A non-uniform dependence of intensities on excitation at 266 nm and 397 nm was shown. Upon the direct 4*f*-4*f* excitation, the highest emission intensity presented the sample obtained at pH 10. Contrary to excitation upon 266 nm, the highest intensity was detected for samples obtained at pH 6 and 9. For selected sample measured were the luminescence emission spectra at room and liquid nitrogen temperatures. A strong temperature dependence of the Eu^{3+} ions was showed in the compiled spectra. Emission excitation spectra revealed typical to Eu^{3+} inner 4*f*-4*f* transitions and two broad charge transfer bands, the O-Eu, and the O-V. Luminescence profiles highlighted the rise and decay of the luminescence. The rise and decay times were calculated based on the collected profiles.

With changing the pH from 4 to 11 the decay time was prolonged. No significant changes in luminescence rise time were observed.

In conclusion, materials obtained via the co-precipitation synthesis route at alkaline pH show improved spectroscopic properties. The co-precipitation synthesis method allowed the pH control during the reaction. Presented study showed the evolution of the size and shape of individual particles from rode-like to oval-like structures.

The dissertation author contributed to the process of creating the scientific article with:

- Synthesis of the YVO_4: 1 mol% Eu^{3+} materials;
- Analysis of the XRD patterns;
- Analysis of the SEM images;
- Measurement and analysis of emission (at room and low temperatures), emission excitation, and decay profiles;
- Preparation of the graphics and charts;
- Co-writing and co-editing the manuscript.

The study of pH influence on structural and spectroscopic properties of nanocrystalline Eu^{3+} ion doped yttrium orthovanadate

Marta Wujczyk, Adam Watras and Rafal J. Wiglusz*

Institute of Low Temperature and Structure Research, Polish Academy of Sciences, Okolna 2, 50-422 Wroclaw, Poland

Abstract

This paper presents an evolution of size and morphology of yttrium orthovanadate, influenced by pH conditions during the synthesis. A thorough research of the spectroscopic properties has been performed. Series of highly crystalline 1 mol% Eu^{3+}:YVO_4 has been synthesized using the co-precipitation method. Additionally, to improve the crystallinity materials have been heat-treated at 800 °C. The structural and morphological properties of the particles were studied using XRD (X-ray powder diffraction) and SEM (Scanning Electron Microscopy) techniques.

In order to investigate spectroscopic properties of 1 mol% Eu^{3+}: YVO_4, emission spectra and luminescence kinetics were measured. It has been found that alkaline pH manifests in smaller particles in comparison to acidic pH conditions. Additionally, superior spectroscopic properties present materials obtained also in alkaline pH.

Keywords: *Yttrium orthovanadate; Nanocrystallites; Evolution of pH dependence; Luminescence properties; Eu^{3+} ion doping*

*Corresponding author:

E-mail:r.wiglusz@intibs.pl;

Phone: +48(071)3954159

Fax: +48(071)3441029

1. Introduction

Research on advanced nanometric phosphor is of great importance. It is crucial to broaden knowledge on novel nano-sized luminescent materials in order to refine morphological, chemical and spectroscopic properties. Yttrium orthovanadate (YVO_4) has attracted an astonishing interest [1–5], which can be attributed to the physicochemical properties and potential applications as host materials for optically active ions [6,7]. Shape and size of yttrium orthovanadate is dependent of the synthesis route and can vary significantly [8–10]. Well-defined nano-sized particles of yttrium orthovanadates have been prepared by various synthesis routes: solid state reaction [11], solvo- and hydrothermal synthesis [12], precipitation and sol-gel methods [13], etc. The ease of modifications during the synthesis as well as its simplicity cause the co-precipitation method to be one of the most effective ones. Although, it has some disadvantages like a necessity for further heat treatment to better the crystal structure and spectroscopic properties.

It has been indicated that pure-phase YVO_4 can be precipitated only in pH conditions greater than 8, because in acidic pH YV_3O_9 and/or $Y_2V_{10}O_{28}$ are obtained [14]. Although, it has been reported that pure phase of YVO_4

nanocrystals can be obtained via hydrothermal and microemulsion synthesis in wide range of pH values during the synthesis [14–17]. Size and morphology of the YVO_4 particles can be achieved by alteration of pH conditions. Hence, in this study materials have been prepared using co-precipitation method. The main goal of this study is to investigate in detail morphological and spectroscopic properties of Eu^{3+} ion doped YVO_4 nanocrystals that vary in pH conditions (from 4 up to 11) during the synthesis. The pH value was adjusted using ammonia solution.

Amidst the lanthanide ions Eu^{3+} can act as a luminescent probe [18–20]. It has been proven that Eu^{3+} probe carries an information concerning the local chemical environment of the dopant as well as an information about the structure [21,22]. Therefore, in this study Eu^{3+} ion was chosen as a dopant. Materials have been prepared by co-precipitation synthesis and heat-treated at 800 °C for 3 hours. Structural, morphological, and spectroscopic measurements have been performed to characterize YVO_4 for the properties influenced by pH.

2. Experimental

2.1. Synthesis route

The nano-sized 1 mol% Eu^{3+} doped YVO_4 powders were obtained by co-precipitation method by mixing stoichiometric amounts of $Y(NO_3)_3$ (Alfa Aesar 99.99%), $Eu(NO_3)_3$ (Alfa Aesar 99.99%) and NH_4VO_3 (Sigma Aldrich, 99%) solutions on a hotplate stirrer. Lanthanide reactants were prepared by digesting oxides (Y_2O_3, Eu_2O_3) in an excess of the ultrapure HNO_3, thereafter re-crystalized thrice to get rid of an excess of HNO_3. Suspension's pH was each time adjusted and maintained by addition of ammonia solution. Steady value varied from pH 4 up to pH 11, with a step equal unity. The synthesis was carried out on a hotplate with a magnetic stirrer at 70 °C for 1.5 hour. Further the precipitate was centrifuged and washed with deionized water to obtain neutral pH. Final residue was dried for 24 hours at 70 °C and later heat-treated at 800 °C for 3 hours. Thereafter, nano-sized powder samples have been obtained.

2.2. XRD, SEM and TEM analysis

The X-ray diffraction patterns were obtained by the use of X'Pert Pro PANalytical diffractometer (Cu, $K_{\alpha 1}$: λ = 1.54060 Å) in a 2θ range of 5-75°, with a scan rate of 2.3 °/min for 30 minutes at a room temperature (300 K). The elemental composition analysis of the YVO_4 nanoparticles as well as morphology analysis, were performed on the scanning electron microscope (FEI Nova NanoSEM 230 equipped with an EDS spectrometer (EDAX PegasusXM4)).

2.3. Spectroscopic measurements

Emission spectra were recorded for three excitation wavelengths, the first λ_{exc} = 397 nm, the second λ_{exc} = 266 nm and the third λ_{exc} = 314 nm. As a source of the first excitation wavelenth a pulse Ti:Sapphire tunable laser pumped by 532 nm line of YAG:Nd^{3+} laser was used. The 266 nm wavelength was obtained by the use of 266 nm diode laser (50 mW). For the emission spectra measurements with the 314 nm

wavelength the McPherson spectrometer was used. This spectrometer is equipped with 0.3 m criss-cross Czerny-Turner monochromator, with a 150 W xenon lamp as an excitation source and with a Hamamatsu R928 photomultiplier as a detector. For measurements with the λ_{exc} = 397 nm excitation wavelength the 435 nm Schott filter was applied. As an optical detector the Hamamatsu PMA-12 photonic multichannel analyzer was used, when excited with λ_{exc} = 397 nm, 266 nm wavelengths. Decay curves were measured at 619 nm, under excitation from Ti:Sapphire LOTIS TII (λ_{exc} = 395) using a Jobin-Yvon THR 1000 spectrophotometer, a Hamamatsu R928 photomultiplier as a detector and a LeCroy WaveSurfer digital oscilloscope. Decay times were calculated with a weighted average equation as follows:

$$\tau_{av} = \frac{\int_{t_{min}}^{t_{max}} I(t)\, t\, dt}{\int_{t_{min}}^{t_{max}} I(t)\, dt}$$

Room temperature excitation spectra were measured by the use of the FLS980 Fluorescence Spectrometer from Edinburgh Instruments equipped with a 450 W Xenon lamp and a Hamamatsu R928P photomultiplier monitoring the $^5D_0 \rightarrow {}^7F_2$ transition at 618.8 nm Each of the obtained spectra was corrected for the instrument response. Temperature dependent emission spectra (100 K, 300 K, 700 K) were recorded on Linkam THMS600 stage for λ_{exc} = 398 nm of the diode laser.

3. Results and discussion

3.1. Structure and morphology

Yttrium orthovanadate crystalizes in zircon-$ZrSiO_4$ type tetragonal structure to $I4_1/amd$ space group (see **Figure 1**). Doping with lanthanide ions causes substitution of octahedral Y^{3+} by Eu^{3+} ions. Ionic radii of Y^{3+} (1.16 Å, CN = 8) is similar to Eu^{3+} (1.21 Å, CN = 8), therefore ion substitution should not cause local crystallographic defects [23]. YVO_4 unit cell parameters are listed in **Table 1**.

Table 1. *YVO_4 unit cell parameters* [24].

crystal structure	*zircon tetragonal*
space group	*$I4_1/amd$* (no. 141)
a (Å)	7.1183(1)
b (Å)	7.1183(1)
c (Å)	6.2893(1)
α (°)	90
β (°)	90
γ (°)	90
point-group symmetry	D_{4h}
coordination no.	Y(8), V(4), O(3)

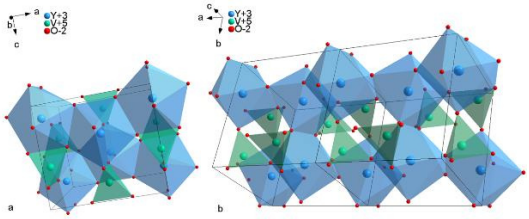

Figure 1. *Three-dimensional (3D) view of the YVO_4 super cell (a) and unit cell (b) indicating the Y^{3+} and V^{5+} coordination polyhedra.*

X-ray diffraction patterns presented in **Figure 2** are in accordance with a standard pattern of YVO_4 acquired from Inorganic Crystal Structure Database (ICSD) no. 78074. Diffraction patterns confirm crystal phase purity of obtained materials. Therefore, it can be stated, that independently on the pH conditions pure YVO_4 can be obtained. However, reaction

yield significantly differs, generally is lower in acidic pH than in alkaline pH. Powder diffractograms derivate from the standard pattern by a 2θ shift towards smaller angles, presumably caused by the expansion of the unit cell. Additionally, increased full width at half maximum (FWHM) of each peak is observed for the materials obtained at pH equal and higher than 8. Broadening of peaks indicates smaller size particles.

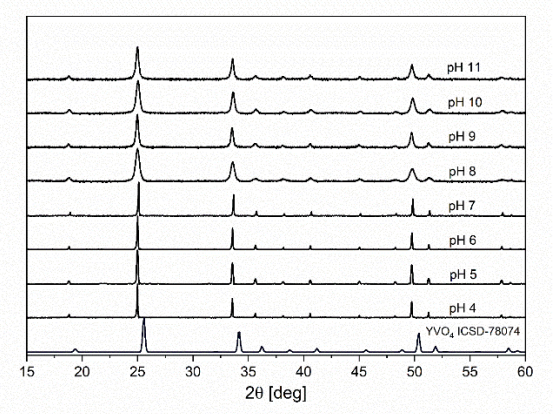

Figure 2. *XRD patterns of 1 mol% Eu^{3+}:YVO_4 annealed at 800 °C for 3 hours obtained at different pH values.*

As presented in **Figure 3** also color of the heat-treated material is dependent on the pH. It is supposed that in different pH conditions various polyvanadate ions take part in crystallization of YVO_4 [25]. It has been stated, that the impurity phases taking part in formation of YVO_4 are i. e. YV_3O_9, $Y_2V_{10}O_{28}$, $Y_8V_2O_7$ [26]. Presence of the vanadyl ions may negatively impact the formation of YVO_4 with oxygen vacancies and formation of V^{4+} defected ions [26]. Therefore, the color of the materials with changing pH may be affected. Intensity of the yellow color may indicate high concentration of defects in YVO_4 materials. Nobe et al. [27] and Garce et al.[28] indicated that the yellow color of YVO_4 is directly associated with oxygen vacancies and vanadium ions of lower oxidation states (V^{4+} ions adjacent to oxygen vacancies). Diffraction data show pure in phase YVO_4 with no unwanted phase **(Figure 2)**. Occurrence of the defects may greatly impact the luminescence properties of the materials. Therefore, when observing the lattice changes application of Eu^{3+} ion as a luminescent probe is crucial. Size of the particles has been determined by SEM images presented in **Figure 4**. As can be noted that particles have well-defined morphology. Change in size of the particles for material obtained in alkaline pH in comparison to those obtained in acidic or neutral pH is visible. Therefore, synthesis alterations are manifested in size reduction and changes in morphology of particles. Particles vary in average size, from 1.3 μm for pH 4, through 400 nm for pH 7, to 110 nm for pH 11. Particles shape distinctly changes from rod-like in acidic pH, oval in neutral, to spindle-like in alkaline pH. SEM images present information concerning the degree of aggregation. Based on **Figure 4**, it can be stated that obtained 1 mol% Eu^{3+}:YVO_4 material independently on the pH shows agglomerated particles. Size distribution of the representative materials is presented in **Figure 5** and **Figure S1-S4**. Strong linear correlation between the length and the width of the particles is observed for those obtained at rather neutral pH. Contrary to the particles obtained at strongly acidic and alkaline pH, where correlation between the length and the width is unnoticeable. The shape evolution is schematically presented in **Figure 6**, herein the actual size of the particles is not preserved. It is proposed that varying pH directly influences the

nucleation, growth and Ostwald ripening. It has been reported by F. Li et. al. that there is a direct correlation between the pH (of the reaction mixture) and the nucleation, growth and aggregation processes [29]. In the beginning stages of the synthesis – after mixing the reactants, initial monomers of YVO_4 are formed. Thereafter, created monomers, grow and in acidic pH create much bigger particles than in alkaline pH. On the basis of the Ostwald's ripening, bigger particles have been created via dissolution of the small particles and followed by redeposition onto the bigger ones. On the other hand, in alkaline pH mixture the Ostwald ripening is disallowed – influencing the growth and the coarsening, resulting in creation of the smaller particles. Therefore, it is proposed, that addition of the diluted ammonia solution might stabilize smaller molecule's surface. Such statement may be based on occurrence of the Ostwald's ripening. Smaller particles are not energetically preferable in comparison the larger ones. In presented case, diluted ammonia may attach NH_4^+ ion onto the surface of the particles and contribute to the nucleation rate as well as particles growth. Suggested explanation for occurring phenomenon is in accordance with obtained SEM images.

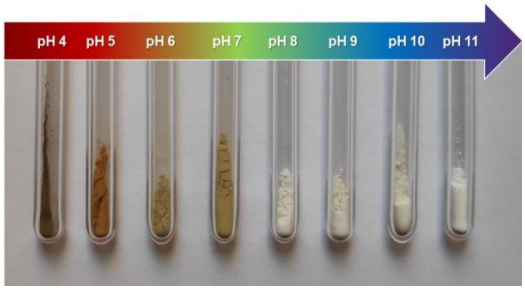

Figure 3. *Illustrative photo of obtained materials in fused quartz tubes.*

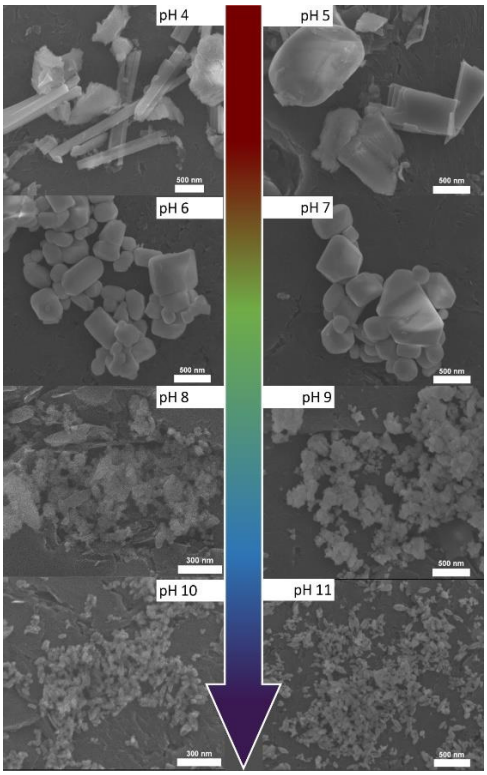

Figure 4. *SEM images of 1 mol% Eu^{3+}: YVO_4 samples synthesized at different pH values from 4 to 11.*

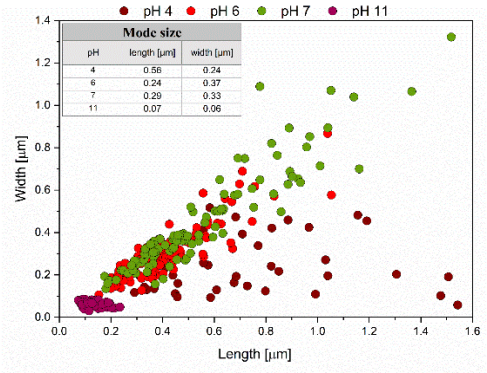

Figure 5*. Size distribution dependent on width and length of the 1 mol% Eu^{3+}:YVO_4 obtained at different pH.*

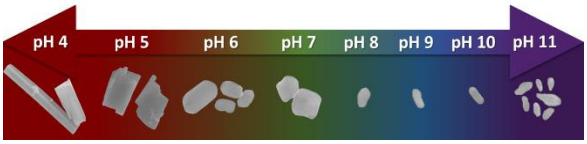

Figure 6*. Scheme of pH conditions during the synthesis correlated with representative particles.*

3.2. Spectroscopic data

The influence of pH conditions manifests not only in morphology and size, but also in

luminescent properties. Obtained emission spectra of the materials prepared in varying pH conditions are presented in **Figure 7**. An excitation wavelength of 398 nm has been chosen to excite the $^5L_6$ term via the $^7F_0 \rightarrow {}^5L_6$ transition. Sharp, narrow bands at 538 nm, 560 nm, 587 nm, 590 nm, 619 nm, 652 nm, 698 nm relate to europium(III) ions and can be assigned to the $^5D_1 \rightarrow {}^7F_{1,2}$, $^5D_0 \rightarrow {}^7F_{0,1,2,3,4}$ transitions, respectively [30,31].

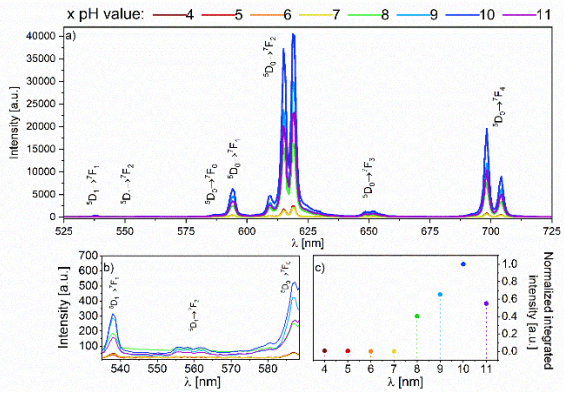

Figure 7. *Emission spectra of 1 mol% Eu^{3+}: YVO_4 annealed at 800 °C for 3 hours, excited with the 397 nm (a), the $^5D_0 \rightarrow {}^7F_0$ transition magnification (b) and integrated, normalized emission spectra in the 500 - 728 nm range (c).*

Materials obtained from alkaline solution present predominant emission intensities in comparison to materials obtained from acidic solution. Sample with the highest emission's intensity is the one obtained at the pH = 10. In case of nanometric particles presence of the surface defects is inevitable. Superior spectroscopic properties of the materials obtained in alkaline pH may depend on the better crystallinity of the material. Less oxygen vacancies are created as well as V^{4+} defect ions. Presence of oxygen vacancies and V^{4+} ions can lead to the non-radiative energy loss. Initial energy may be trapped in created defects and directly affect the emission intensity of materials obtained in acidic pH. Emission bands of the materials obtained in strongly alkaline pH are slightly broaden in comparison to those obtained in more neutral and acidic pH. Most likely it can be assigned to crystal structure distortions [32]. The $^5D_0 \rightarrow {}^7F_2$ transition is the electric dipole (ED) transition and the $^5D_0 \rightarrow {}^7F_1$ transition is the magnetic dipole (MD) transition. In each material ED transitions present predominant intensities when compared to MD transitions. Therefore, it can be deduced that crystallographic environment of Eu^{3+} is non-centrosymmetric. To confirm the non-centrosymmetric location of Eu^{3+} the asymmetry parameter R has to be calculated. Parameter R carries an information about a degree of asymmetry in near vicinity of Eu^{3+} in crystal structure, Eu-O covalence influenced by site symmetry, covalence of ligand atoms and electronegativity [8]. Asymmetry parameter can be calculated using following equation:

$$R = \frac{\int {}^5D_0 \rightarrow {}^7F_2}{\int {}^5D_0 \rightarrow {}^7F_1}$$

For calculations two data ranges were taken into consideration, 1st for the $^5D_0 \rightarrow {}^7F_2$ transition: 602 - 642 nm, and 2nd for the $^5D_0 \rightarrow {}^7F_1$ transition: 590 - 602 nm. **Table 2** presents calculated values of the asymmetry parameter. For each material parameter R is higher than 1, therefore a non-centrosymmetric environment of the optically active lanthanide ion is reaffirmed.

Table 2. Asymmetry parameter R calculated for each material.

Material	*pH*	*R*
1 mol% Eu^{3+}: YVO_4	4	8.2
	5	8.3
	6	8.1
	7	8.1
	8	10.6
	9	10.2
	10	10.9
	11	10.6

Based on the **Figure 7** it can be stated, that europium ions are localized specifically in one crystal site independent on the pH, given the fact that each material obeys the *2J+1* rule for the number of particular band's Stark splitting.

In **Figure 8** presented are low-, room- and high-temperature emission spectra of 1 mol% Eu^{3+}:YVO_4, pH 11. The $^5D_1 \rightarrow {}^7F_1$ (λ_{max} = 538 nm), the $^5D_1 \rightarrow {}^7F_2$ (λ_{max} = 561 nm), and the $^5D_0 \rightarrow {}^7F_0$ (λ_{max} = 587 nm) transitions have higher intensities when measured in high-temperature (700 K) than in low- (80 K) or room-temperature (300 K) (**Figure 8b**).

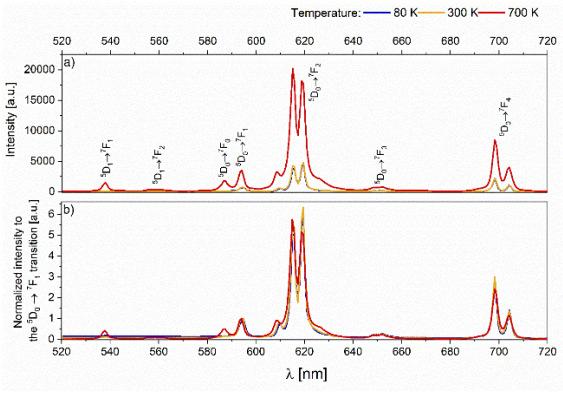

Figure 8. Emission spectra of 1 mol% Eu^{3+}: YVO_4, pH = 11, obtained at 80 K, 300 K, 700 K (a) and normalized to the $^5D_0 \rightarrow {}^7F_1$ transition emission spectra (b), excitation source - 398 nm diode laser, 70 mA.

Emission spectra obtained via excitation with the 314 nm and 266 nm wavelengths are presented in **Figure 9 and 10** respectively**Błąd! Nie można odnaleźć źródła odwołania.**. Excitation wavelengths were chosen to match the $O^{2-} \rightarrow V^{5+}$ and $O^{2-} \rightarrow Eu^{3+}$ charge transfer bands, observed in excitation spectra (**Figure 11**). Emission spectra present characteristic to europium ions sharp *f-f* transition bands. For 314 nm and 266 nm excitations the highest emission's intensity can be assigned to the material obtained at pH 9. When excited with λ_{exc} = 266 nm the $^5D_1 \rightarrow {}^7F_{1,2}$ and the $^5D_0 \rightarrow {}^7F_0$ transitions are observed. However, when excited with λ_{exc} = 314 nm transitions are not monitored. Herein, direct dependence of the emission intensity on the pH conditions is disturbed. It can be influenced by earlier sated crystal structure defects and distortions as well as location of more Eu^{3+} ions on the surface of the particle. The excitation of Eu^{3+} is indirect, meaning set to match the charge transfer bands. Therefore, energy transfer from $(VO_4)^{3-}$ may result in a low efficiency for the materials obtained in highly alkaline conditions. Although better efficiency of the energy transfer may be observed for the materials obtained in more acidic conditions, because there is a probability of more even distribution of Eu^{3+} ions in the bulk and the surface. Additionally, presence of oxygen vacancies up to a point can positively effect luminescence properties. Energy transfer to optically active rare earth ions can be sensitized via oxygen vacancies as a result of substantial mixing of charge transfer states [33].

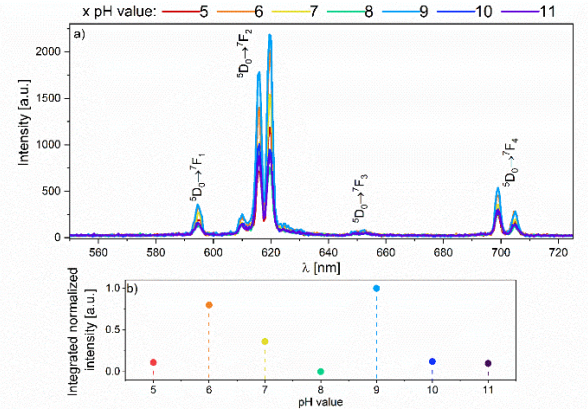

Figure 9. *Emission spectra obtained for λ_{exc} = 314 nm excitation at 300 K (a) and integrated and normalized emission spectra representation of the emission's intensity (b). Measurement was prepared for the 1 mol% Eu^{3+}: YVO_4 annealed at 800 °C for 3 hours.*

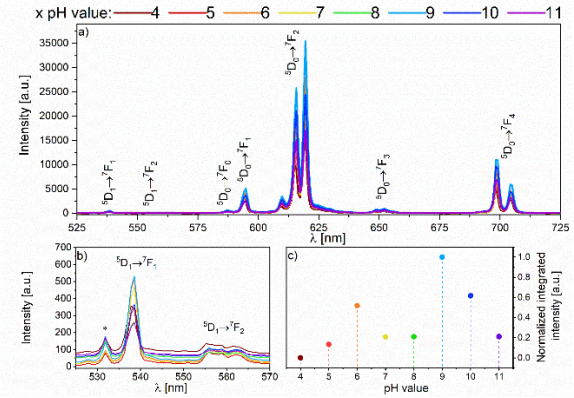

Figure 10. *Emission spectra obtained for λ_{exc} = 266 nm excitation at 300 K (a), the magnification of the $^5D_1 \rightarrow {}^7F_J$ transition bands (b), and integrated and normalized representation of the transitions intensity (c). Measurements were prepared for the 1 mol% Eu^{3+}:YVO_4 annealed at 800 °C for 3 hours.*

Excitation spectra were obtained via monitoring the $^5D_0 \rightarrow {}^7F_2$ transition at λ = 618.8 nm. In **Figure 11** two broad band transitions are observed. The first band can be assigned as the O^{2-}-Eu^{3+} charge transfer (CT) with maximum at around 266 nm, and the latter band as the O^{2-}-V^{5+} charge transfer (CT) with a maximum at around 310 nm [10]. In the Vis region of the spectra (above 350 nm) sharp *f-f* transition bands that correspond to Eu^{3+} ions are evident [4,34]. The *f-f* transitions occur in each material but have higher intensities for the materials obtained at the alkaline pH. For the materials obtained in acidic pH CT bands overpower f-f transitions, in case of the materials obtained in alkaline pH this dominance is weakened. Therefore, it may be an affirmation of more Eu^{3+} ions being localized on the surface of the particles obtained in alkaline pH in comparison to these obtained in acidic and neutral pH.

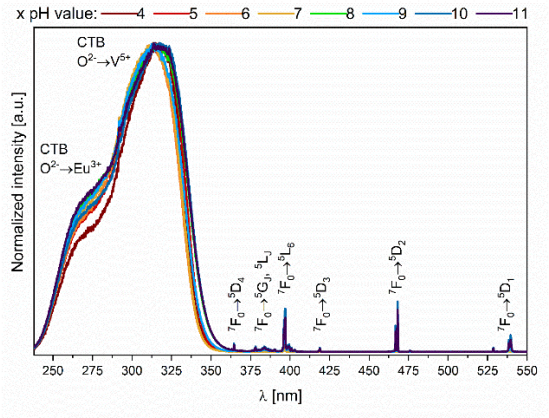

Figure 11. Excitation spectra measured at 300 K for 1 mol% Eu^{3+}: YVO_4 samples obtained at different pH values, monitored for the $^5D_0 \rightarrow {}^7F_2$ transition at 618.80 nm and excited with 397 nm xenon lamp.

Measurements of luminescence kinetics are presented in **Figure 12** and **Table 3**, as decay and growth curves, and correspondingly decay and growth times. Obtained decay curve shows double-exponential nature, as it is characteristic to Eu^{3+}: YVO_4 materials [4,35,36]. Based on the emission spectra of Eu^{3+}:YVO_4 **(Figure 7, 8, 9, 10)** europium ions locate only in one crystallographic position of Y^{3+}, D_{2d}. The double-exponential nature of the materials may be the result of the presence of vanadium ions of lower oxidation states [26]. Therefore, averaged decay times have been calculated. Change of pH from acidic to alkaline, results in generally longer decay times. When compared, decay time of material obtained at pH 4 is three times

longer than decay time of material obtained at pH 8. Calculated decay times present dependence on pH as well as correlation with emission spectra (**Figure 7**). There is a gradual change in intensity of the emission and decay time up to pH 7. For pH ≥ 8 higher emission intensities and sudden elongation of decay times are observed. Longer decay times may stem from a change in the average Eu^{3+}-Eu^{3+} distances, what is in accordance proposed location of the ions on the surface and structure distortions in form of oxygen vacancies, most likely occurring in materials with low pH. The oxygen vacancies and presence of V^{4+} may cause quenching of Eu^{3+} ions and shortening of decay times [26].

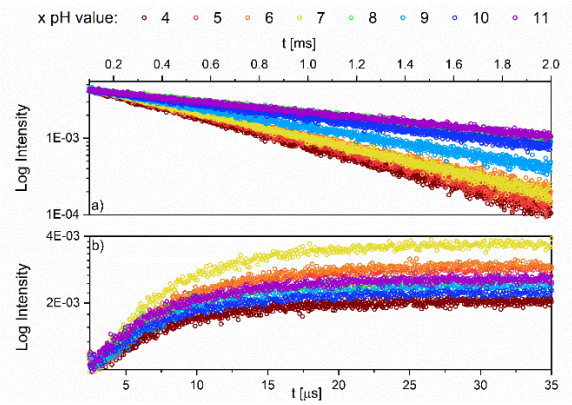

Figure 12. *Decay profiles (a) and growth profiles (b) for the 1 mol% Eu^{3+}: YVO_4 material obtained at different pH values, annealed at 800 °C for 3 hours, monitored for the $^5D_0 \rightarrow {}^7F_2$ transition at 619 nm at 300 K.*

Table 3. *Calculated averaged decay times and growth times for the $^5D_0 \rightarrow {}^7F_2$ transition at 619 nm of 1 mol% Eu^{3+}: YVO_4, heat treated at 800 °C for 3 hours, obtained at a wide range of pH values.*

	Growth time [µs]	*Averaged decay time [ms]*
pH = 4	6.90	0.55
pH = 5	6.82	0.57
pH = 6	6.83	0.62
pH = 7	7.20	0.61
pH = 8	6.71	1.18
pH = 9	6.51	0.83
pH = 10	6.52	1.10
pH = 11	6.69	1.50

4. Conclusions

In presented work the focus was put on the evolution of the size and morphology of 1 mol% Eu^{3+}: YVO_4 obtained in a variety of pH conditions. The co-precipitation synthesis has led to obtaining pure zircon type, tetragonal structure independently on the pH conditions. Additionally, heat-treated materials present different colors of the powders dependently on the pH conditions. Change in size and morphology of the particles is also evident. Material obtained in acidic pH up to neutral, present particles with bigger sizes and rode-like, cubic, and oval shapes. Spectroscopic properties of the materials obtained in alkaline pH show superior characteristics in comparison to materials obtained in acidic pH.

5. Acknowledgments

The authors would like to acknowledge the National Science Centre Poland (NCN) for the financial support within the Project ‘Preparation and modulation of spectroscopic properties of $YXZO_4$, where X and Z - P^{5+}, V^{5+}, As^{5+}, doped with "s^2-like" ions and co-doped with rare earth ions’ (No. UMO-2019/33/B/ST5/02247). We are grateful to M.Sc. E. Bukowska for performing XRPD measurements and to PhD. D. Szymanski for SEM-EDS measurements.

6. References

1 L. Xing, W. Yang, J. Lin, M. Huang and Y. Xue, *Sci. Rep.*, 2017, **7**, 1–7.

2 M. Yu, J. Lin, Z. Wang, J. Fu, S. Wang, H. J. Zhang and Y. C. Han, *Chem. Mater.*, 2002, **14**, 2224–2231.

3 I. Sokólska, E. Heumann, S. Kück and T. Lukasiewicz, *Appl. Phys. B*, 2000, **71**, 893–896.

4 N. S. Singh, R. S. Ningthoujam, M. N. Luwang, S. D. Singh and R. K. Vatsa, *Chem. Phys. Lett.*, 2009, **480**, 237–242.

5 C. C. Wu, K. B. Chen, C. Sen Lee, T. M. Chen and B. M. Cheng, *Chem. Mater.*, 2007, **19**, 3278–3285.

6 R. J. Wiglusz, A. Bednarkiewicz and W. Strek, *Inorg. Chem.*, 2012, **51**, 1180–1186.

7 T. Grzyb, R. J. Wiglusz, A. Gruszeczka and S. Lis, *Dalt. Trans.*, 2014, **43**, 17255–17264.

8 Q. F. Ren, B. Zhang, S. H. Chen, S. L. Wang, Q. Zheng, Y. Ding, H. S. Qian and Z. Jin, *Phys. B Condens. Matter*, 2019, **557**, 1–5.

9 Y. Zheng, X. Sun, H. Su, L. Sun and C. Qi, *Mater. Res. Bull.*, 2018, **105**, 149–153.

10 L. Yang, S. Peng, M. Zhao and L. Yu, *Appl. Surf. Sci.*, 2019, **473**, 885–892.

11 Y. Zuo, W. Ling and Y. Wang, *J. Lumin.*, 2012, **132**, 61–63.

12 Z. Xu, X. Kang, C. Li, Z. Hou, C. Zhang, D. Yang, G. Li and J. Lin, *Inorg. Chem.*, 2010, **49**, 6706–6715.

13 R. J. Wiglusz, L. Marciniak, R. Pazik and W. Strek, *Cryst. Growth Des.*, 2014, **14**, 5512–5520.

14 H. Wu, H. Xu, Q. Su, T. Chen and M. Wu, *J. Mater. Chem.*, 2003, **13**, 1223–1228.

15 R. Wangkhem, N. S. Singh, N. P. Singh, S. D. Singh and L. R. Singh, *J. Lumin.*, 2018, **203**, 341–348.

16 J. Wang, M. Hojamberdiev and Y. Xu, *Solid State Sci.*, 2012, **14**, 191–196.

17 J. Wang, M. Hojamberdiev, Y. Xu and J. Peng, *Mater. Chem. Phys.*, 2011, **125**, 82–86.

18 S. Basu, D. K. Patel, J. Nuwad, V. Sudarsan, S. N. Jha, D. Bhattacharyya, R. K. Vatsa and S. K. Kulshreshtha, *Chem. Phys. Lett.*, 2013, **561**–**562**, 82–86.

19 G. Jia, P. A. Tanner, C.-K. Duan and J. Dexpert-Ghys, *J. Phys. Chem. C*, 2010, **114**, 2769–2775.

20 N. Yaiphaba, R. S. Ningthoujam, N. Shanta Singh, R. K. Vatsa and N. Rajmuhon Singh, *J. Lumin.*, 2010, **130**, 174–180.

21 P. Hanninen and H. Harma, *Lanthanide Luminescence: Photophysical, Analytical and Biological Aspects*, 2011, vol. 7.

22 A. Watras, P. Boutinaud, R. Pazik and P. J. Dereń, *J. Lumin.*, 2016, **175**, 249–254.

23 R. D. Shannon and C. T. Prewitt, *Acta Cryst*, 1969, **B25**, 925.

24 B. C. Chakoumakos, M. M. Abraham and L. A. Boatner, *J. Solid State Chem.*, 1994, **109**, 197–202.

25 T. T. Huong, L. T. Vinh, H. T. Phuong, H. T. Khuyen, T. K. Anh, V. D. Tu and L. Q. Minh, *J. Lumin.*, 2016, **173**, 89–93.

26 L. Yang, G. Li, M. Zhao, J. Zheng, X. Guan and L. Li, *CrystEngComm*, 2012, **14**, 3227–3235.

27 Y. Nobe, H. Takashima and T. Katsumata, *Opt. Lett.*, 1994, **19**, 1216–1218.

28 N. Y. Garces, K. T. Stevens, G. K. Foundos and L. E. Halliburton, *J. Phys. Condens. Matter*, 2004, **16**, 7095–7106.

29 F. Li, C. Yang, Q. Li, W. Cao and T. Li, *Mater. Lett.*, 2015, **145**, 52–55.

30 B. Bondzior and P. J. Dereń, *J. Lumin.*, 2019, **213**, 151–157.

31 D. Wawrzynczyk, M. Nyk, A. Bednarkiewicz, W. Strek and M. Samoc, *J. Nanoparticle Res.*, , DOI:10.1007/s11051-014-2690-x.

32 L. Yanhong and H. Guangyan, *J. Solid State Chem.*, 2005, **178**, 645–649.

33 H. K. Yang, H. Choi, B. K. Moon, B. C. Choi, J. H. Jeong, J. H. Kim and K. H. Kim, *Solid State Sci.*, 2010, **12**, 1445–1448.

34 R. Pązik, K. Zawisza, A. Watras, K. Maleszka-Bagińska, P. Boutinaud, R. Mahiou and P. J. Dereń, *Mater. Res. Bull.*, 2013, **48**, 337–342.

35 F. He, P. Yang, N. Niu, W. Wang, S. Gai, D. Wang and J. Lin, *J. Colloid Interface Sci.*, 2010, **343**, 71–78.

36 G. Jia, Y. Song, M. Yang, Y. Huang, L. Zhang and H. You, *Opt. Mater. (Amst).*, 2009, **31**, 1032–1037.

Supplementary information

P1: *The study of the influence of pH on the structural and spectroscopic properties of nanocrystalline Eu^{3+} ion-doped yttrium orthovanadate*

Marta Wujczyk, Adam Watras, Rafal J. Wiglusz

Dalton Transactions, 2021, 50, 3724

DOI: 10.1039/d0dt04052e

IF: 4.569

The study of pH influence on structural and spectroscopic properties of nanocrystalline Eu^{3+} ion doped yttrium orthovanadate

Marta Wujczyk, Adam Watras and Rafal J. Wiglusz*

Institute of Low Temperature and Structure Research, Polish Academy of Sciences, Okolna 2, 50-422 Wroclaw, Poland

Abstract

This paper presents an evolution of size and morphology of yttrium orthovanadate, influenced by pH conditions during the synthesis. A thorough research of the spectroscopic properties has been performed. Series of highly crystalline 1 mol% Eu^{3+}:YVO_4 has been synthesized using the co-precipitation method. Additionally, to improve the crystallinity materials have been heat-treated at 800 °C. The structural and morphological properties of the particles were studied using XRD (X-ray powder diffraction) and SEM (Scanning Electron Microscopy) techniques.

In order to investigate spectroscopic properties of 1 mol% Eu^{3+}: YVO_4, emission spectra and luminescence kinetics were measured. It has been found that alkaline pH manifests in smaller particles in comparison to acidic pH conditions. Additionally, superior spectroscopic properties present materials obtained also in alkaline pH.

Keywords: *Yttrium orthovanadate; Nanocrystallites; Evolution of pH dependence; Luminescence properties; Eu^{3+} ion doping*

*Corresponding author:

E-mail:r.wiglusz@intibs.pl

Phone: +48(071)3954159

Fax: +48(071)3441029

In Figures S1-S4 are presented the size distribution analysis of the materials obtained at different pH. Synthesis in acidic and neutral pH results in bigger particles than in case of alkaline pH. Additionally, for the acidic and neutral pH more widespread distribution of sizes is observed, ranging from 100 nm to 2 μm. For the material obtained in alkaline pH (11) size distribution is narrower and ranges from 40 to 240 nm. Also, for alkaline and acidic pH thresholds particles present elongated shapes, and for neutral pH particles are more squared. There is also a linear dependence of width and length with changing size within one material.

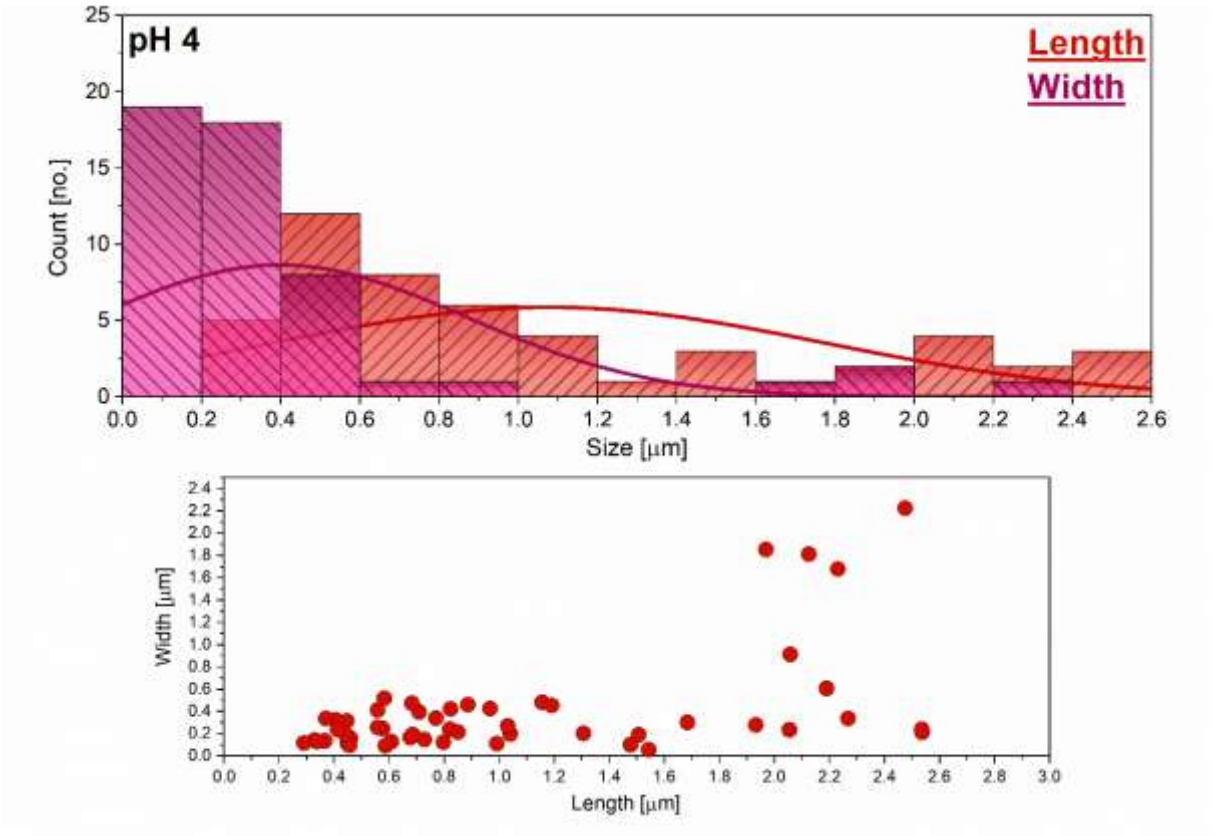

Figure S1. *Size distribution analysis based on SEM images of 1 mol% Eu^{3+}:YVO_4 obtained at pH 4.*

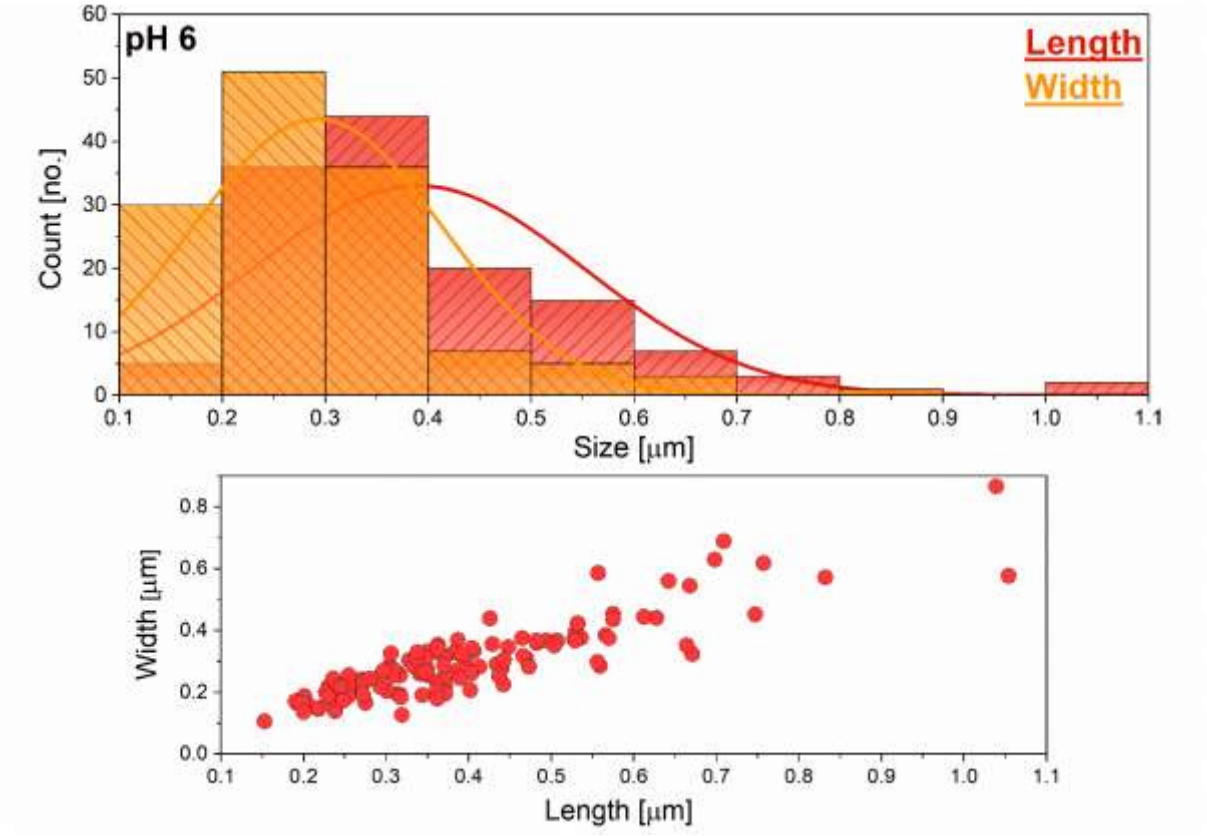

***Figure S2**. Size distribution analysis based on SEM images of 1 mol% Eu^{3+}:YVO_4 obtained at pH 6.*

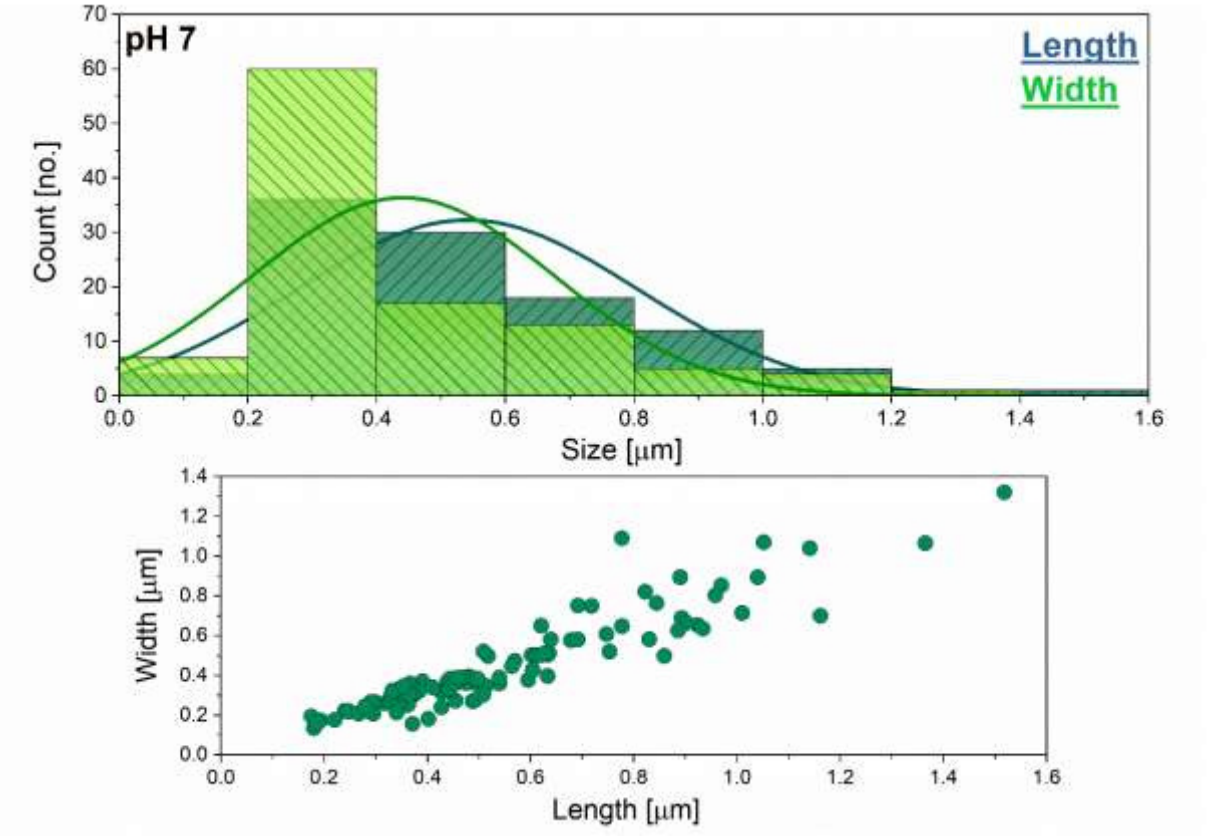

***Figure S3**. Size distribution analysis based on SEM images of 1 mol% Eu^{3+}:YVO_4 obtained at pH 7.*

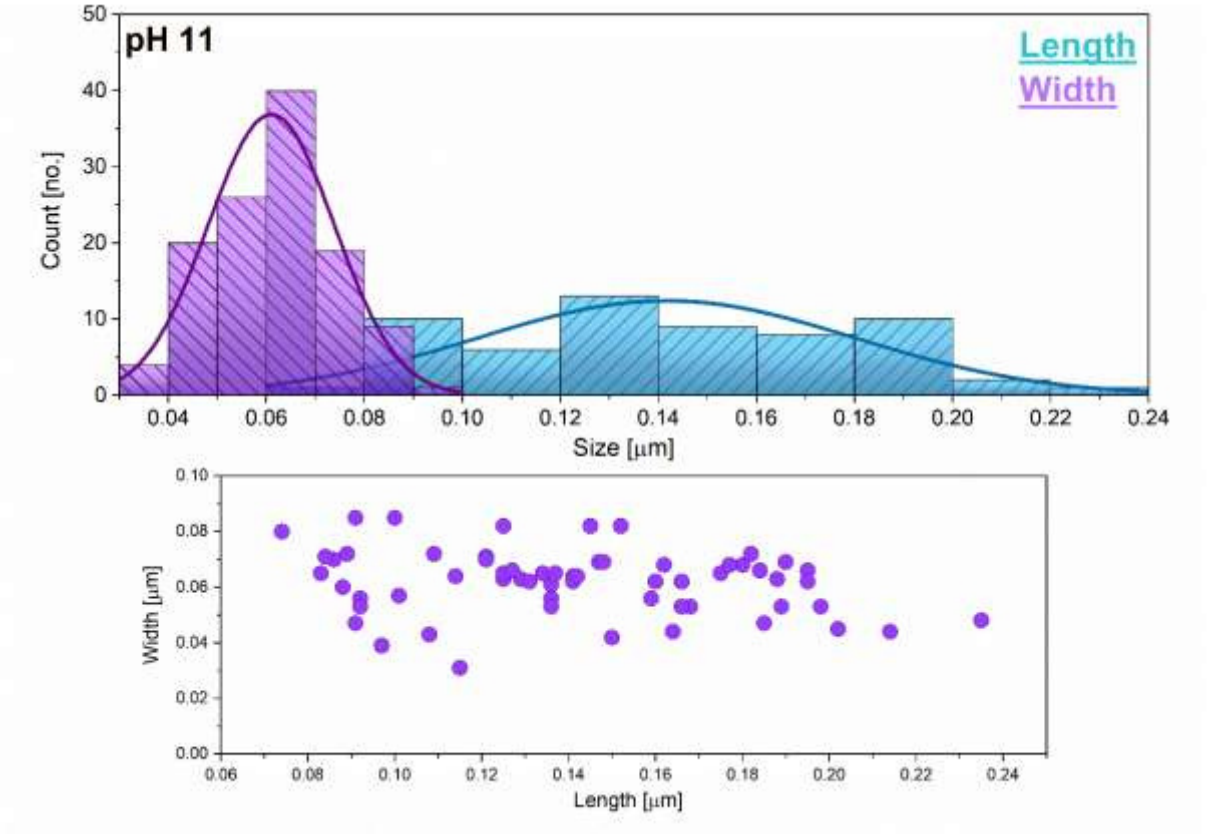

Figure S4. *Size distribution analysis based on SEM images of 1 mol% Eu^{3+}:YVO_4 obtained at pH 11.*

P2: *Emission Quenching and First Evidence of Tb^{3+}-to-As^{5+} Charge Transfer in Terbium(III) Ion-Doped $YV_xAs_{1-x}O_4$ Solid-State Solution*

Marta Wujczyk, Adam Watras, Philippe Boutinaud, Marco Bettinelli, Sara Targonska, Jorma Hölsä, Rafal J. Wiglusz

The Journal of Physical Chemistry C, 2020, 124, 31, 17364-17371
DOI: 10.1021/acs.jpcc.0c04668
IF: 4.177

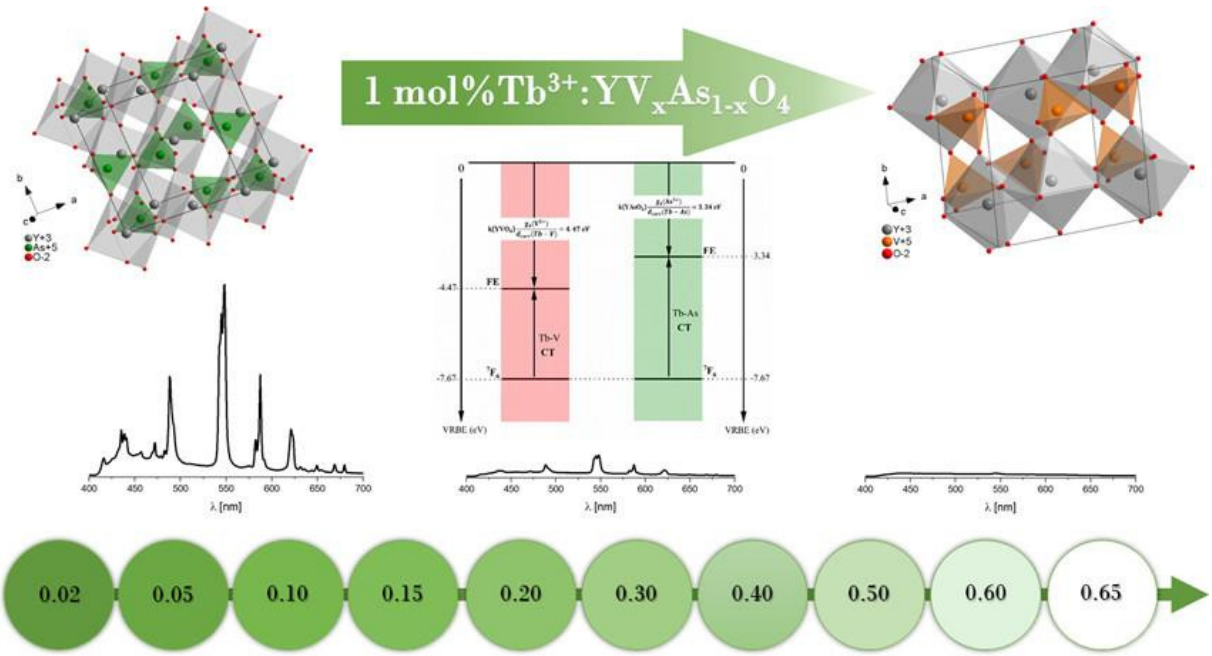

The motivation for the scientific article entitled "*Emission Quenching and First Evidence of Tb^{3+}-to-As^{5+} Charge Transfer in Terbium(III) Ion-Doped $YV_xAs_{1-x}O_4$ Solid-State Solution"* was related to the lack of Tb^{3+} luminescence in yttrium orthovanadate. It was shown, by G. Blasse and A. Bril, that upon host excitation Tb^{3+} ions do not emit. [101] Therefore, in this work $YV_xA_{1-x}O_4$ system was proposed to determine the quenching of Tb^{3+} ions luminescence in the presence of V^{5+}.

This study aimed to investigate the quenching process of Tb^{3+} ion's luminescence. Therefore, yttrium orthoarsenate matrix was diluted with vanadium ions gradually. The concentration of the dopant was set to 1 mol% Tb^{3+}. The only variable was V^{5+} to As^{5+} ions ratio.

The $YV_xAs_{1-x}O_4$: 1 mol% Tb^{3+}, where x equalled 0.02 to 0.65, materials were obtained utilizing the co-precipitation synthesis. Observed was a shift of the XRD planes. It indicated a change of unit cell size by the V^{5+}-As^{5+} substitution. Independent of the V^{5+}/As^{5+} ratio, the zircon-type continuous solid solution was obtained. SEM and TEM images revealed nanosized particles with an average size of 39×20 nm.

The focus was put on the analysis of the spectroscopic properties, concerning the quenching of Tb^{3+} ions luminescence. As expected, highest emission intensity was observed with materials containing low amounts of V^{5+}. As the concentration of V^{5+} ions increased, the probability of V^{5+} and Tb^{3+} ions being close to each other also increased. Noticed was the gradual decrease of Tb^{3+} ions emission. The concentration of 65 mol% V^{5+} was the limit at which complete quenching of Tb^{3+} ion luminescence was attained. Luminescence decay profiles were measured. For V^{5+} > 40 mol%, the behaviour of the profile changed from single exponential to double exponential. Based on decay times, the quenching rate was calculated. Excitation emission spectra were collected for the materials. The characteristic to Tb^{3+} ions' transitions, the $^5D_3 \rightarrow {}^7F_{2,3,4,5}$ and the $^5D_4 \rightarrow 7F_{1,2,3,4,5,6}$, were observed. In the UV spectral region three broad, overlapping bands were noted and assigned to the O-As, the Tb-As, and the O-V charge transfer transitions. The possibility of the Tb-As charge transfer band was noted for the first time and assured with performed calculations. The model based on Dorenbos methodology allowed for the determination of the Tb^{3+} ions quenching pathway. It was proposed that the quenching is directly correlated to adjacent Tb^{3+} and V^{5+} ions and is dependent on the low energy (≈ 3.2 eV) Tb-V charge transfer state.

In summary the study presented a thorough physicochemical investigation of $YV_xAs_{1-x}O_4$: 1 mol% Tb^{3+} materials, where x = 0.02 – 0.65. By TEM and SEM images, an analysis of the structure and morphology was presented, revealing the nanometric size of the particles. Variations in the composition of the solid solution of a small one are directly reflected in the spectroscopic properties of the materials. Changes in the composition of the solid solution were directly reflected by the spectroscopic properties of the materials. Applied techniques allowed for a determination of the Tb^{3+} ions luminescence quenching pathway. The formation of the new Tb-As MMCT state was noted.

The dissertation author contributed to the process of creating the scientific article with:

- Co-synthesis of the $YV_xAs_{1-x}O_4$: 1 mol% Tb^{3+} materials;
- Analysis of the XRD patterns;
- Analysis of the SEM and TEM images;
- Measurement and analysis of emission, emission excitation, and decay profiles;
- Preparation of the graphics and charts, excluding Figure 8;
- Co-writing and co-editing the manuscript.

THE JOURNAL OF PHYSICAL CHEMISTRY C

pubs.acs.org/JPCC

Article

Emission Quenching and First Evidence of Tb^{3+}-to-As^{5+} Charge Transfer in Terbium(III) Ion-Doped $YV_xAs_{1-x}O_4$ Solid-State Solution

Marta Wujczyk, Adam Watras, Philippe Boutinaud, Marco Bettinelli, Sara Targonska, Jorma Hölsä, and Rafal J. Wiglusz*

Cite This: J. Phys. Chem. C 2020, 124, 17364−17371

Read Online

ACCESS | Metrics & More | Article Recommendations | Supporting Information

ABSTRACT: The paper discusses the origin of emission quenching and the formation of metal-to-metal charge-transfer states in yttrium orthovanadate-arsenates doped with Tb^{3+} ions. For that purpose, a series of highly crystalline yttrium orthovanadate-arsenate nanoparticles (type $YV_xAs_{1-x}O_4$, where x = 2−65 mol %) doped with Tb^{3+} ions were prepared using the co-precipitation method. The structural and morphological properties of the particles were studied by means of X-ray powder diffraction (XRD), transmission electron microscopy (TEM), and scanning electron microscopy (SEM) techniques. The photoluminescence spectral and dynamical properties of $YV_xAs_{1-x}O_4$ doped with 1 mol % Tb^{3+} ions were investigated in detail. It was found that the emission quenching is related to changes in the band gap and Tb^{3+}-to-V^{5+} metal-to-metal charge transfer. Further, the Tb^{3+}-to-As^{5+} metal-to-metal charge transfer was identified and rationalized based on different models.

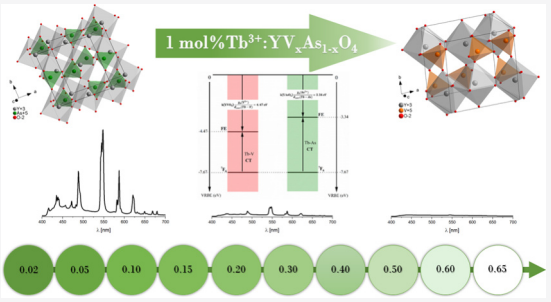

1. INTRODUCTION

A large number of research groups are looking for novel, nanosized, stable chemically and mechanically stable materials with attractive and distinct spectroscopic properties.[1−4] One of the materials that have brought an immense interest is YVO_4. The interest is rightful due to the fact that doping with rare-earth ions like Eu^{3+} or Nd^{3+}, and/or additionally codoped with s^2-type cations like Bi^{3+}, has a number of potential applications, such as sensors,[5] fluorescent labels,[6] display devices,[7] laser materials,[8−11] and bioprobes.[12,13] However, it is known for long that doping with Tb^{3+} does not generate any luminescence in YVO_4.[14,15] This phenomenon is ascribed to the formation of a low-lying Tb^{3+}-to-V^{5+} metal-to-metal charge transfer (MMCT) state that efficiently quenches the otherwise brightly emitting $^5D_4$ level. Some 15 years ago, the Tb^{3+}:$Y(P,V)O_4$ solid solution was investigated to determine the reason for the total inactivity of Tb^{3+} ions in YVO_4. It was concluded that the intensity of Tb^{3+} ion emission is proportional to the probability that none of the four metal ion sites of Tb^{3+} ion is occupied by V^{5+} ion.[16] Similar work has been carried out more recently in sol−gel nanosized Tb^{3+}:$Y(P,V)O_4$ solid solution and also concluded on the Tb^{3+} ion emission quenching mediated by a low-lying Tb-V CT state.[17] As discussed in earlier studies, the MMCT process is ascribed as an excitation from the ground state of Tb^{3+} ion to the bottom of the conduction band of the host, which allows locating the $^7F_0$ ($4f^8$) ground state of Tb^{3+} ion relative to the host fundamental states.[18,19] In YVO_4, the bottom of the conduction band consists majorly of V(3d) orbitals[20−22] and features a relatively narrow band gap of 3.8 eV,[23] whereas in YPO_4, the band gap is much larger, up to 9.2 eV,[24] and the P orbitals contribute very little to the bottom of the conduction band that has a strong Y(4d) character.[20,22] It comes that the Tb^{3+}-to-P^{5+} or Tb^{3+}-to-Y^{3+} CT, if occurring, has high energy relative to Tb → V CT.

In the present work, we investigate the emission behavior of Tb^{3+} ion in the nanosized solid solution $Y(As,V)O_4$, where As^{5+} ion plays a role similar to that of P^{5+} ion in terms of dilution of the V^{5+} ion within the crystal lattice. The essential difference with the previous report of DeLosh et al.[16] is the $3d^{10}$ electron configuration of As^{5+} ion that allows 4s orbitals to participate in the bottom of the lattice conduction band in the mixture with the Y(4d) orbitals[25] with a corresponding band gap of 4.5 eV.[26] This potentially permits $Tb^{3+}(4f^8)$-to-$As^{5+}(4s^0)$ CT to occur in the near-UV spectral region, although somehow higher relative to YVO_4, and related vanadium-rich compounds to avoid quenching of Tb^{3+} ion emission. In this regard, the maximum concentration of V^{5+} ions that quenches the luminescence of Tb^{3+} ions in $YV_xAs_{1-x}O_4$ solid solution is determined to be 65 mol % and the occurrence of Tb-As MMCT is evaluated by adapting a model previously established for the Pr^{3+}-to-d^0 transition-metal CT.[18]

Received: May 24, 2020
Revised: July 2, 2020
Published: July 10, 2020

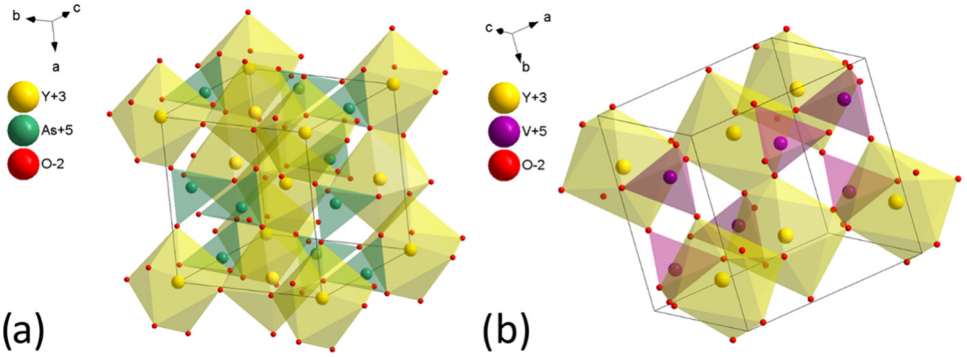

Figure 1. Three-dimensional (3D) view of the unit cell representation of (a) $YAsO_4$ and (b) YVO_4.

2. MATERIALS AND METHODS

2.1. Synthesis Route. Nanosized yttrium orthovanadate-arsenate doped with terbium ions were prepared by wet chemical synthesis via co-precipitation method. The concentration of the optically active ions was set to be 1 mol % Tb^{3+} for each material, with respect to the appropriate Y^{3+} molar content. The V^{5+} ions concentration was changed from 2 to 65 mol % with respect to the appropriate As^{5+} molar content. Analytical grade Y_2O_3 (99.99% Alfa Aesar), Tb_7O_{11} (99.99% Alfa Aesar), As_2O_3 (99.5% Sigma-Aldrich), and NH_4VO_3 (99.5% Sigma-Aldrich) were used as the starting materials.

In this method, stoichiometric amounts of the Y_2O_3 and Tb_7O_{11} were digested in excess of dilute HNO_3 to transform them into nitrate salts. The obtained lanthanide nitrates were recrystallized three times to get rid of the excess HNO_3. Ammonium metavanadate was dissolved in deionized water. The arsenic oxide was transformed to arsenic acid with an excess amount of ultrapure HNO_3. Next, H_3AsO_4 and NH_4VO_3 solutions were mixed and the mixture was added to nitrate salts solution ($Y(NO_3)_3$ and $Tb(NO_3)_3$). The reaction was maintained at a stirring plate for 1.5 h at approximately 100 °C. The pH of the suspension was adjusted to 8 with aqueous ammonia. The obtained precipitate was washed and centrifuged at least thrice to reach the pH value. The as-prepared materials were dried for 24 h at 70 °C and heated at 800 °C for 3 h to form crystallized nanoparticles.

2.2. XRD, SEM, and TEM Analyses. The development of the crystal phase was checked by X-ray diffraction (XRD). The patterns were collected in the 2θ range of 5−120° with an X'Pert PRO X-ray diffractometer (Cu Kα1, 1.54060 Å) (PANalytical). The XRD patterns were assigned using the Joint Committee on Powder Diffraction Standards Database (JCPDS) and Inorganic Crystal Structure Database (ICSD) and then analyzed. Analysis of the morphology, dispersibility, and size of the materials was performed using the scanning electron microscope (SEM) FEI Nova NanoSEM 230 equipped with an energy-dispersive system (EDS) spectrometer (EDAX PegasusXM4) as well as the high-resolution transmission electron microscopy (HR-TEM) on a Philips CM-20 Super Twin microscope.

2.3. Spectroscopic Analysis. Infrared spectra were measured by a Thermo Scientific Nicolet iS50 FT-IR spectrometer equipped with an Automated Beam splitter exchange system (iS50 ABX containing DLaTGSKBr detector), built-in all-reflective diamond ATR module (iS50 ATR), Thermo Scientific Polaris and HeNe laser was used as an IR radiation source. The infrared spectra were recorded in KBr pellets at a 4000−400 cm^{-1} range with a spectral resolution of 2 cm^{-1} at room temperature. The obtained infrared spectra (Figure S1) are featured in the Supporting Information. Emission spectra were recorded upon excitation at 380 nm using a tunable Ti/sapphire laser pumped with the second harmonic of the YAG:Nd^{3+} pulse laser (f = 10 Hz, t < 10 ns). A long pass Schott filter (420 nm) was used. The Hamamatsu PMA-12 photonic multichannel analyzer was used as an optical detector. All measurements were performed with the fixed parameters such as the exposure time (200 ms) and the cumulative amount of measurements (20), finally resulting in an averaged emission spectrum. The excitation spectra were collected at room temperature using an FLS980 Fluorescence Spectrometer from Edinburgh Instruments equipped with a 450 W xenon lamp and a Hamamatsu R928P photomultiplier. The emission decay profiles corresponding to the $^5D_4 \rightarrow {}^7F_5$ transition of Tb^{3+} at 548 nm were recorded at room temperature upon 380 nm excitation using a Tektronix MDO3052 digital oscilloscope.

3. RESULTS AND DISCUSSION

3.1. Structure and Morphology. The crystal structure of YXO_4 (where X = As, V) is tetragonal, ascribed to space group $I4_1/amd$ (no. 141), and offers only one yttrium cationic site for the possible substitution with rare-earth ions (see Figure 1). The parameters that characterize unit cells of the compounds are as follows (see Table 1).

Table 1. Crystallographic Data for Yttrium Orthovanadate and Yttrium Orthoarsenate[27,28]

	YVO_4	$YAsO_4$
cryst. syst.	zircon tetragonal	zircon tetragonal
space group	$I41/amd$ (no. 141)	$I41/amd$ (no. 141)
a (Å)	7.1183(1)	6.9040(1)
b (Å)	7.1183(1)	6.9040(1)
c (Å)	6.2893(1)	6.2820(1)
α (deg)	90	90
β (deg)	90	90
γ (deg)	90	90
point-group symmetry	D_{4h}	D_{4h}
coordination no.	Y(8); V(4); O(3)	Y(8); As(4); O(3)

Moreover, the mixed $YV_xAs_{1-x}O_4$ system doped with Tb^{3+} ions should be in accordance with Vegard's law as a solid solution. A similar situation was observed in the case of $YV_xP_{1-x}O_4$ and Eu^{3+}:$YV_xP_{1-x}O_4$ that was obtained via the co-precipitation method.[29,30]

The formation of crystalline undoped and 1 mol % Tb^{3+}-doped $YV_xAs_{1-x}O_4$ nanomaterials was followed by XRD

https://dx.doi.org/10.1021/acs.jpcc.0c04668
J. Phys. Chem. C 2020, 124, 17364−17371

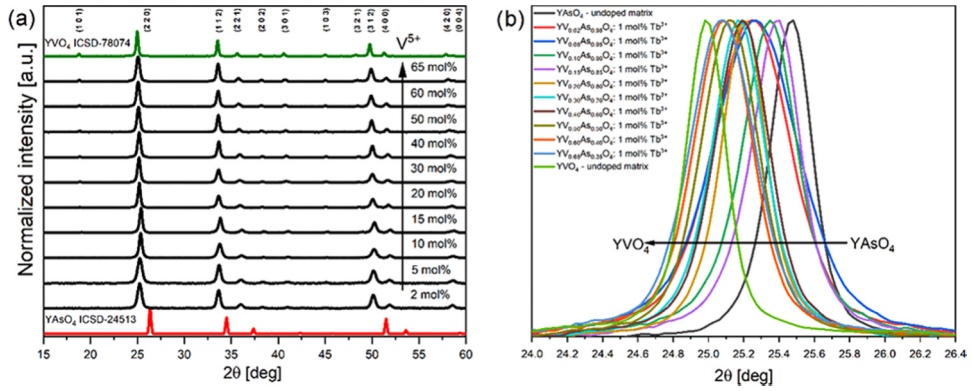

Figure 2. XRDP patterns of $YV_xAs_{1-x}O_4$ doped with 1 mol % Tb^{3+} ions and heat-treated at 800 °C for 3 h in air (a). Dependence of the lattice plane (220) shift upon V^{5+}/As^{5+} ratio in $YV_xAs_{1-x}O_4$ doped with terbium ions (b).

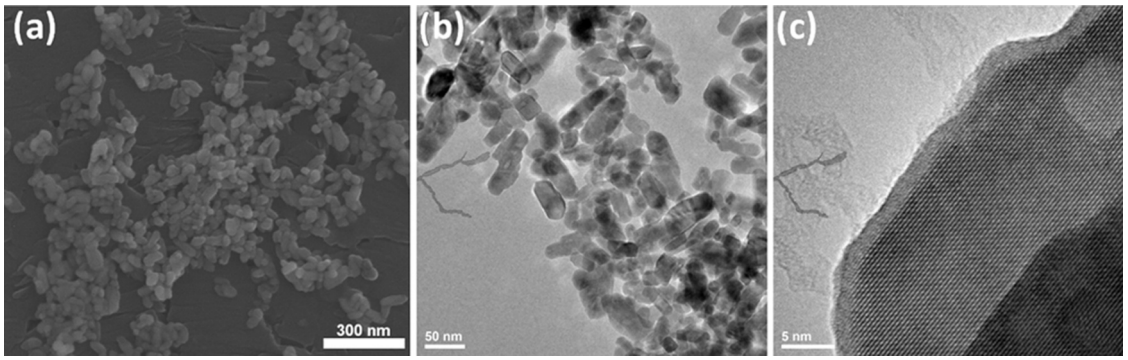

Figure 3. Size and morphology representation by SEM image (a) and TEM images (b, c) of 1 mol % Tb^{3+}:$YV_{0.5}As_{0.5}O_4$ sample thermally treated at 800 °C.

measurements (see Figures S2 and 2, respectively). All samples prepared by utilizing wet chemistry techniques showed detectable crystallinity and purity at all ranges and proposed sintering temperature at 800 °C. Moreover, a continuous shift of the (220) plane toward lower 2θ angles was observed as an effect of the cell parameters change induced by the substitution of the bigger V^{5+} (0.355 Å at CN 4) cation by smaller one As^{5+} (0.335 Å) (see Figure 2b), respectively.

TEM images of the representative 1 mol % Tb^{3+}:$YV_{0.5}As_{0.5}O_4$ sample are shown in Figure 3. After 3 h at 800 °C, we observe that elongated particles form flat plates with an average size in the range of 20−40 nm (Figure 4). These observations are in line with earlier data reported for the nanosized YVO_4 or $YAsO_4$ systems.[31,32]

3.2. Spectroscopic Properties. The emission spectra of the 1 mol % Tb^{3+}:$YV_xAs_{1-x}O_4$ (x = 0.02−0.65) are shown in Figure 5. The visible lines are ascribed to the characteristic 4f−4f transitions of Tb^{3+} ions.[33−35] The intensity of these lines

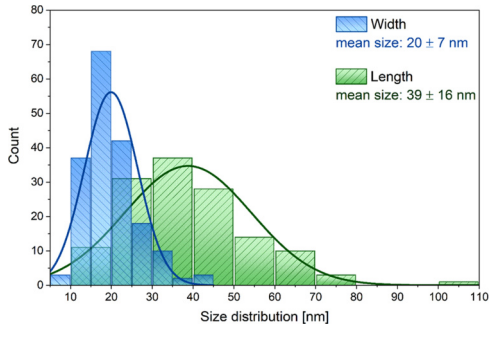

Figure 4. Particle size distribution designated by TEM images.

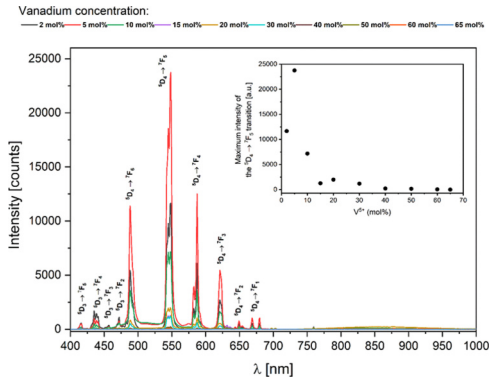

Figure 5. Emission spectra (λ_{exc} = 380 nm) obtained for 1 mol % Tb^{3+}:$YV_xAs_{1-x}O_4$ thermally treated at 800 °C.

increases sharply up to x = 0.05 and then gradually decreases for larger values of x, i.e., with an increase of the probability that Tb^{3+} ion finds V^{5+} ion in its immediate neighborhood to form the Tb-V MMCT state. Total quenching is observed for x = 0.65 at room temperature. This, in fact, motivated us to interrupt the solid solution at this content.

This compositional dependence of the emission intensity is well confirmed by the analysis of the temporal decay of the $^5D_4$-$^7F_5$ emission of Tb^{3+} in the solid solution. The compounds were excited at 380 nm in correspondence with the $^7F_0$−$^5L_6$ intraionic transition of Tb^{3+} ions (Figure 6). The decays present

https://dx.doi.org/10.1021/acs.jpcc.0c04668
J. Phys. Chem. C 2020, 124, 17364−17371

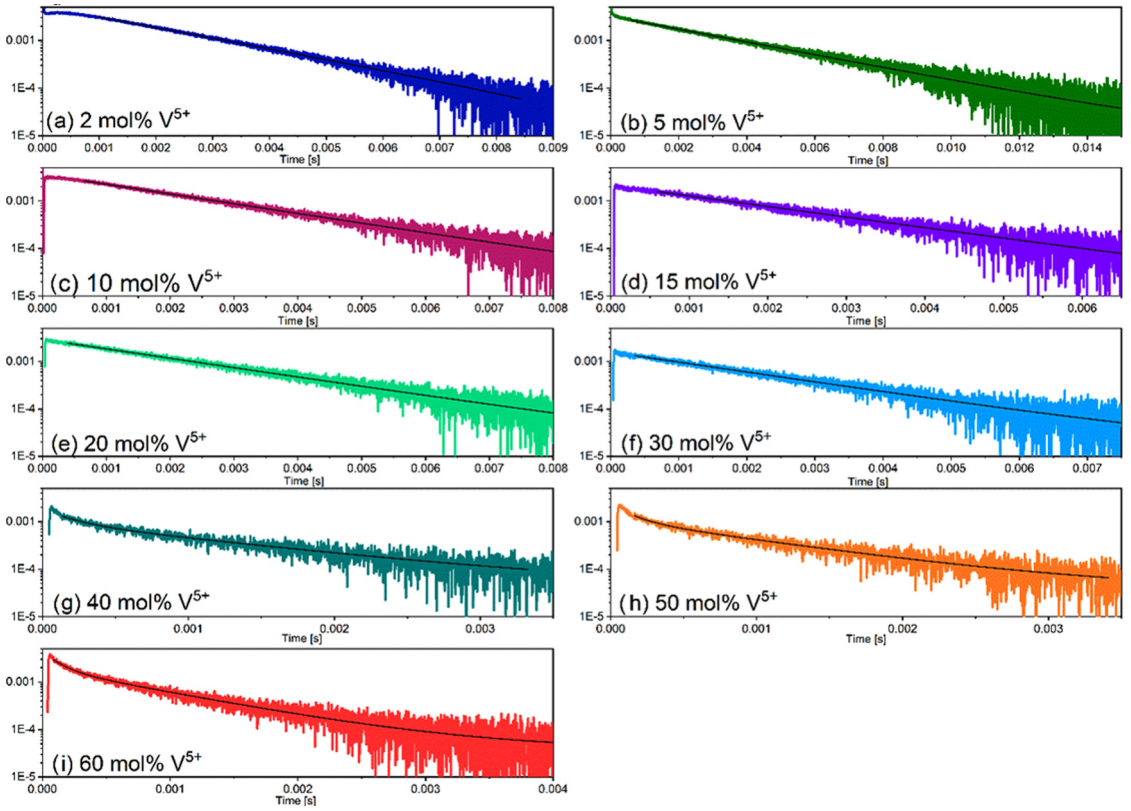

Figure 6. Decay time profiles of 1 mol % Tb^{3+}:$YV_xAs_{1-x}O_4$ measured for the $^5D_4 \rightarrow {}^7F_5$ transition monitored at 548 nm and pumped with 380 nm wavelength of the pulse laser.

a single-exponential nature for materials with a concentration of V^{5+} up to 40 mol % and a double-exponential nature above 40 mol % V^{5+} ions. The emergence of the double-exponential decay profile is directly correlated with a high content of V^{5+} ions in the matrices. It could be explained through the crystal structure non-uniformity related to two separate phases of the YVO_4 and $YAsO_4$ in the crystal structure. Minakova et al. have shown that the peak related to the (220) plane was split. In this case, there could be indicated the existence of another crystal phase in the $YV_xAs_{1-x}O_4$ matrix.[36] Therefore, an emergence of the double-exponential decay profile could be seen, when such a phenomenon occurs. The short time component can be associated with the Tb^{3+}:$YV_xAs_{1-x}O_4$ phase in which Tb^{3+} ions are nearby V^{5+} ions as well as As^{5+} ions. On the other hand, the longtime component may come from the Tb^{3+}:$YAsO_4$ phase in which Tb^{3+} ions are directly coordinated by As^{5+} ions. All values get the millisecond components of the time interval reproduced in Figure 5. The values were obtained by fitting the decay profiles with exponential functions in Origin software (Table 2). Decay profiles of the materials containing up to 30 mol % V^{5+} were fitted with the single-exponential function

$$y = y_0 + A_1 e^{-(x-x_0)/t_1} \quad (1)$$

And decay profiles of the materials containing above 40 mol % V^{5+} were fitted with the double-exponential function

$$y = y_0 + A_1 e^{-(x-x_0)/t_1} + A_2 e^{-(x-x_0)/t_2} \quad (2)$$

where y_0 is the offset; x_0 is the center; A_1, A_2 are the amplitudes; and t_1, t_2 are time constant and coefficient of determination (R^2) at 0.94−0.99. Hence, with an increment of V^{5+} ion concentration, a shortening of the decay time is observed.

Table 2. Decay Time Dependent on Vanadium Ion Concentration in the 1 mol % Tb^{3+}:$YV_xAs_{1-x}O_4$ System

V^{5+} (mol %)	t_1 (ms)	t_2 (ms)
2	1.96 ± 0.01	
5	3.21 ± 0.01	
10	2.11 ± 0.01	
15	1.94 ± 0.02	
20	2.18 ± 0.01	
30	2.05 ± 0.02	
40	1.23 ± 0.09	0.19 ± 0.02
50	0.97 ± 0.04	0.14 ± 0.01
60	0.84 ± 0.01	0.12 ± 0.003

Decay times characterize themselves with rises prominent for each sample except that containing 5 mol % V^{5+} ions (Figure S3). The longest rise is observed for the sample containing 2 mol % V^{5+} ions. The presence of the rises may be explained on the basis of the $^5D_4$ term population by the nonradiative transition's occurring from the $^5D_3$ term, which is directly populated by the absorption of the excitation energy (λ_{exc} = 380 nm) (Figure S3). Additionally, based on the lifetime profiles, a quenching rate of the Tb^{3+} emission by V^{5+} was calculated. The quenching rate k_q can be calculated using the following formula

$$k_q = \frac{1}{\tau_q} - \frac{1}{\tau_0} \quad (3)$$

where τ_q is the decay time with quenching and τ_0 is the decay time without quenching. Using values for 5 and 60% samples (τ_0 = 3.21 ms and τ_q = 0.84 ms, respectively), quenching rate stands at k_q = 879.

https://dx.doi.org/10.1021/acs.jpcc.0c04668
J. Phys. Chem. C 2020, 124, 17364−17371

Room-temperature excitation spectra collected in correspondence with the green $^5D_4-^7F_5$ emission of Tb^{3+} ions are presented in Figure 7 for all members of the Tb^{3+}:$YV_xAs_{1-x}O_4$

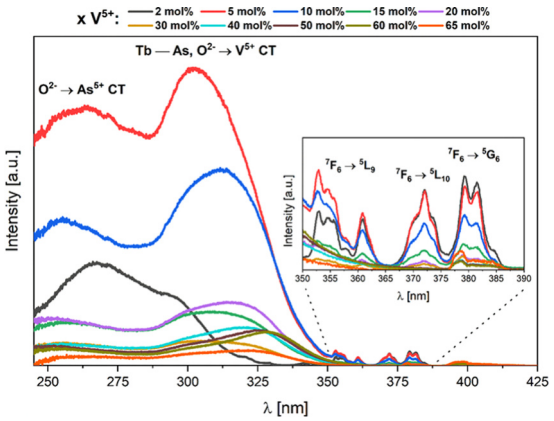

Figure 7. Excitation emission spectra of the $YV_xAs_{1-x}O_4$ doped with 1 mol % Tb^{3+} ions annealed at 800 °C.

solid solution. They show the weak 4f−4f transitions of Tb^{3+} ions in the near-UV spectral region and intense transitions with f−d and/or charge transfer character below 350 nm.

The origin of these excitation signals depends on the considered member of the solid solution. As we know since the work of DeLosh et al., the first critical issue is the probability for the Tb^{3+} ions to find the V^{5+} acceptors in its immediate neighborhood in the $YV_xAs_{1-x}O_4$ solid solution. In the zircon crystal structure, this probability is $P(x) = 1-(1-x)^2$. Values are given in Table 3 together with the energy position of the lowest

Table 3. Probability for the Tb^{3+} Ions to Find V^{5+} Acceptor in Its Immediate Neighborhood and the Energy of the Lowest Excitation Band in the Solid Solution $YV_xAs_{1-x}O_4$

x	$P(x)$ (%)	energy of the lowest excitation band (eV)
0.02	4	4.14
0.05	10	4.05
0.10	19	3.95
0.15	28	3.93
0.20	36	3.89
0.30	51	3.87
0.40	64	3.84
0.50	75	3.79
0.60	84	3.77
0.65	88	3.83

excitation band in the compounds. The energy of the lowest excitation band was obtained by fitting the excitation-emission curves with the Gauss function in Origin software

$$y = y_0 + \frac{A}{w\sqrt{\frac{\pi}{2}}} e^{-2(x-x_c)^2/w^2} \quad (4)$$

where y_0 is the offset, x_c is the center of the peak, w is the width, and A is the area. The coefficient of determination (R^2) stands at >0.99.

Let us start with the compound Tb^{3+}:$YV_{0.02}As_{0.98}O_4$, i.e., the codoped arsenate $YAsO_4$: 2 mol % V^{5+},1 mol % Tb^{3+} with negligible interaction between Tb^{3+} and V^{5+} ions. In the previous work,[31] the fundamental excitation (FE) of the $YAsO_4$ host was located roughly at ≈255 nm (39 200 cm^{-1}, 4.86 eV) from a low spectrally defined shoulder. Here, the spectral definition of this band is much better with a maximum observed clearly at 267 nm (4.64 eV, see the black curve in Figure 7). This value matches fairly the 4.5 eV reported in another study.[26] Therefore, we assign this excitation band to host FE, i.e., the $O^{2-} \rightarrow As^{5+}$ CT occurring within the tetrahedrally coordinated arsenate groups. The presence of this band demonstrates that the Tb^{3+} emission is host sensitized. The second, lower-lying excitation band at 4.14 eV is assignable to $4f^8 \rightarrow 4f^7 5d^1$ transitions of Tb^{3+} or/and to $Tb^{3+}(4f^8)$, $As^{5+}(3d^{10}4s^0) \rightarrow Tb^{4+}(4f^7)$, $As^{4+}(3d^{10}4s^1)$ CT transition. At present, nothing is known on the occurrence of $Tb^{3+} \rightarrow As^{5+}$ MMCT in solids and similarly, no direct information exists on the energy of the $Tb^{3+}(4f^8)$, $V^{5+}(3d^0) \rightarrow Tb^{4+}(4f^7)$, $V^{4+}(3d^1)$ CT in YVO_4, since the Tb^{3+} ions emission is quenched in this compound. We tentatively introduce here a method allowing an estimation of these CT energies by transposing the Pr^{3+}-to-metal CT model published in another study[37] to the case of Tb^{3+} ions. This model uses the methodology developed by Dorenbos through which the energy levels of divalent and trivalent lanthanides can be positioned respective to fundamental bands (top of valence band/bottom of conduction band) of a given crystal lattice (A).[38,39] Following the Dorenbos' model, we calculate the vacuum-referred binding energy of an electron located in the $4f^8$ ($^7F_0$) ground state of Tb^{3+} ion in the lattice (A) in eV using

$$\mathrm{VRBE}(Tb^{3+}, 4f^8, \mathrm{A}) = -24.92 + \frac{18.05 - U(\mathrm{A})}{0.777 - 0.0353U(\mathrm{A})} - U(\mathrm{A}) + \Delta E(4f^8, 4f^6) \quad (5)$$

where 24.92 eV is the third ionization energy of europium as a free atom, $\frac{18.05 - U(\mathrm{A})}{0.777 - 0.0353U(\mathrm{A})}$ is the chemical shift,[40] $U(\mathrm{A})$ is the Coulomb repulsion energy associated with lattice (A) determined within an accuracy of ≈±0.1 eV as the binding energy difference between the Eu^{2+} ($4f^7$) and Eu^{3+} ($4f^6$) ions ground states[41−43] and $\Delta E(4f^8, 4f^6)$ is the energy separating $4f^8$ and $4f^6$ ground states of Tb^{3+} and Eu^{3+} ions. This value was estimated at 3.58 eV in[19,44] but recently revised in[39,45] to a value amounting 3.4 eV, which we will retain here. Following the methodology described in another study and adapting it to Tb^{3+}[37] the absolute value of VRBE(Tb^{3+}, $4f^8$, A) is connected with the $Tb^{3+} \rightarrow M^{n+}$ CT energy according to

$$\mathrm{MMCT}(Tb^{3+} - M^{n+}, \mathrm{A}) = \mathrm{VRBE}(Tb^{3+}, 4f^8, \mathrm{A}) - k(\mathrm{A})\frac{\chi_{\mathrm{CN}'}(M^{n+})}{d(Tb^{3+} - M^{n+})} \quad (6)$$

where $\chi_{\mathrm{CN}'}(M^{n+})$ is the electronegativity of the metal cation M^{n+} with coordination number CN′ in the crystal lattice as calculated in a previous study,[46] $k(\mathrm{A})$ is a lattice-related parameter, and $d(Tb^{3+}\text{-}M^{n+})$ is the shortest distance between the cations, corrected from ionic radii mismatches between Tb^{3+} and its doping site in the crystal lattice. Taking A = YVO_4, we have $\chi_4(V^{5+})$ = 2.46, the electronegativity of tetrahedrally coordinated V^{5+} as picked up in the previous study,[46] $d(Tb^{3+}\text{-}V^{5+})$ = 3.155 Å and $k(YVO_4)$ = 5.73 eV.[37] Using $U(YVO_4)$ = 7.0 eV,[37] we calculate VRBE(Tb^{3+},$4f^8$, YVO_4) = −7.67 eV from eq 5 and MMCT (Tb^{3+}-V^{5+}, YVO_4) = 3.2 eV from eq 6. This value matches well the energy level scheme published in a previous study.[47] This very low position of the Tb-V CT state accounts

https://dx.doi.org/10.1021/acs.jpcc.0c04668
J. Phys. Chem. C 2020, 124, 17364−17371

for the quenching of the Tb^{3+} ion emission in YVO_4. The situation is more complex for $YAsO_4$, essentially because the spectroscopy of trivalent lanthanides is very poorly documented in this compound, except for Eu^{3+}.[24,48,49] In particular, the absence of information pertaining to f−d transitions of Ce^{3+} ions prevents calculating the energy of the lowest spin-allowed $4f^8 \rightarrow 4f^7 5d^1$ transition of Tb^{3+} ions in this lattice via the redshift model of Dorenbos.[41,42] This issue remains therefore open. In this context, we will concentrate on the possibility of a Tb^{3+}-to-As^{5+} CT in this compound. The use of eqs 5 and 6 requires the determination of $U(YAsO_4)$ and $k(YAsO_4)$; $d(Tb^{3+}\text{-}V^{5+})$ = 3.155 Å is obtained from ICSD 24513 standard card of $YAsO_4$ and $\chi_4(As^{5+})$ = 2.5 is picked up from the previous study.[46] $U(YAsO_4)$ can be estimated following a concept introduced by Dorenbos in the previous study[50] and reused latter in,[37,38] which establishes a connection between $U(A)$ and the average electronegativity $\chi_{av}(A)$ of the lattice (A) defined as

$$\chi_{av}(A) = \frac{\sum_i n_i Z_i \chi_i}{\sum_i n_i Z_i} \tag{7}$$

where n_i is the number of cations of type i with charge Z_i and electronegativity χ_i. Using the electronegativity scale of Li and Xue,[46] we calculate $\chi_{av}(YVO_4)$ = 2.03 and $\chi_{av}(YAsO_4)$ = 2.04. The similarity of the values prompts us to consider in the first intention that $U(YAsO_4) = U(YVO_4)$ = 7.0 eV. It should be noted that the value $\chi_{av}(YVO_4)$ differs a bit from that published by Dorenbos et al.,[38] which used Pauling electronegativities. The value of $k(YAsO_4)$ is yet impossible to determine by means of empirical approaches as it was done in the previous study[37] due to the lack of experimental optical data pertaining to Pr^{3+} or Tb^{3+} in arsenates. However, we can try a direct estimation of this value considering that $k(A)$ in eq 6 is analogous to a Coulomb constant and therefore writable in units of eV Å as $k(A) = \frac{14.4}{\varepsilon_r(A)}$, where $\varepsilon_r(A)$ is the real part of the dielectric constant of compound (A) in a spectral region corresponding to the UV excitation band that is suspected of CT origin, i.e., ≈+4 eV. We found $\varepsilon_r(YAsO_4) \approx 3.4$[51] (JVASP-10202), which gives $k(YAsO_4) \approx 4.2$ eV Å. Introducing all of the required data in eq 6 gives a Tb^{3+}−As^{5+} energy of 4.33 eV in Tb^{3+}:$YAsO_4$. Considering the values given in Table 3, this result looks relevant. We therefore conclude that the lower-lying excitation band in the As-rich part of the Tb^{3+}:$YV_xAs_{1-x}O_4$ solid solution contains a $Tb^{3+} \rightarrow As^{5+}$ CT contribution, possibly mixed with Tb f−d transitions, although this could not be assessed in the present work. As evidenced in Table S1, the increase in V^{5+} content does not modify the Tb-As/V distances significantly. This means that the $Tb^{3+} \rightarrow As^{5+}$ CT almost keeps its energy; only the probability of forming that CT state diminishes. In parallel, a second excitation band grows up to the low-energy side. The energy position of this band (≈3.8 eV) matches $O^{2-} \rightarrow V^{5+}$ LMCT within the isolated $(VO_4)^{3-}$ groups[22] and is ascribed accordingly. This band attests to the occurrence of $(VO_4)^{3-}$-to-Tb^{3+} energy transfer. Concomitantly, the progressive increase of the probability of having a V atom in the immediate vicinity of Tb atoms results in the formation of the Tb^{3+}-to-V^{5+} CT state at ≈3.2 eV, which quenches the Tb^{3+} ion emission. The corresponding situation is sketched in Figure 8 for the end members of the Tb^{3+}:$YV_xAs_{1-x}O_4$ solid solution.

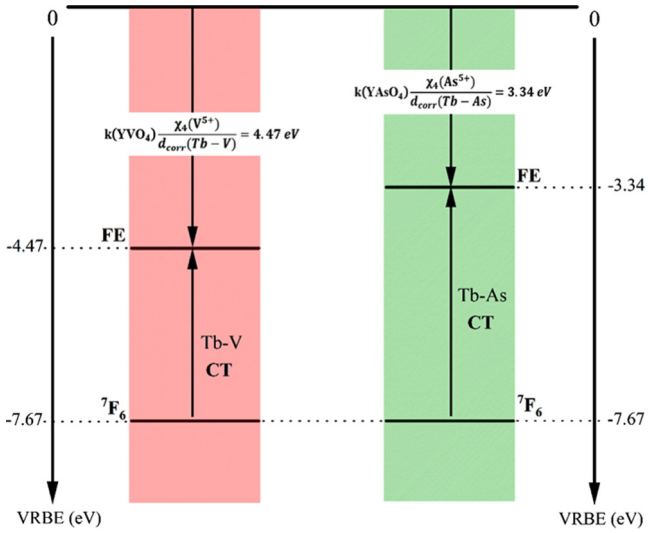

Figure 8. Scheme of energy levels in the $YV_xAs_{1-x}O_4$ system.

4. CONCLUSIONS

The terbium-doped $YV_xAs_{1-x}O_4$ system ($0 \le x \le 0.65$) has been synthesized as pure tetragonal nanocrystals using a co-precipitation synthesis route. The detailed study of yttrium orthovanadate-arsenate structures presented complete crystallization and was confirmed by X-ray diffraction and Rietveld analysis. It has been found and described in detail the regularity with observed structural and spectroscopic measurements.

Moreover, the designed physicochemical experiments have allowed unambiguous determination of the spectroscopic properties, such as emission, excitation, and luminescence kinetics. The presented measurements and calculations allowed a clear inference and thus proposing the basic information concerning Tb^{3+}−V^{5-} quenching and formation of Tb^{3+}-to-As^{5+} metal-to-metal charge transfer (CT) state. Furthermore, the main reasons for the quenching occurrence are both very low position of the Tb-V CT state and directly influenced by the variation of the band gap.

■ ASSOCIATED CONTENT

Supporting Information

The Supporting Information is available free of charge at https://pubs.acs.org/doi/10.1021/acs.jpcc.0c04668.

Fourier transform infrared (FT-IR) spectrum of yttrium orthovanadate-arsenate powders (Figure S1); diffraction data for undoped matrices of YVO_4, $YV_xAs_{1-x}O_4$, and $YAsO_4$ in comparison to standard ICSD patterns (a) and the dependence of the lattice plane (220) on shift (b) (Figure S2); unit cell parameters (a, c), cell volume (V), crystallite size as well as refine factor (R_w) for $Tb_{0.01}Y_{0.99}V_xAs_{1-x}O_4$ prepared at 800 °C as a function of V^{5+} ion concentration (Table S4); rise time dependent on the vanadium concentration (Figure S3) (PDF)

■ AUTHOR INFORMATION

Corresponding Author

Rafal J. Wiglusz − *Institute of Low Temperature and Structure Research, Polish Academy of Sciences, 50-422 Wroclaw, Poland;* orcid.org/0000-0001-8458-1532; Phone: +48 (071) 3954159; Email: r.wiglusz@intibs.pl; Fax: +48 (071) 3441029

https://dx.doi.org/10.1021/acs.jpcc.0c04668
J. Phys. Chem. C 2020, 124, 17364−17371

Authors

Marta Wujczyk − *Institute of Low Temperature and Structure Research, Polish Academy of Sciences, 50-422 Wroclaw, Poland*

Adam Watras − *Institute of Low Temperature and Structure Research, Polish Academy of Sciences, 50-422 Wroclaw, Poland;* orcid.org/0000-0003-4736-0356

Philippe Boutinaud − *Université Clermont Auvergne, SIGMA Clermont, Institut de Chimie de Clermont-Ferrand, F-63000 Clermont-Ferrand, France*

Marco Bettinelli − *Luminescent Materials Laboratory, Department of Biotechnology, University of Verona, 37134 Verona, Italy;* orcid.org/0000-0002-1271-4241

Sara Targonska − *Institute of Low Temperature and Structure Research, Polish Academy of Sciences, 50-422 Wroclaw, Poland*

Jorma Hölsä − *Department of Physics, University of the Free State, ZA-9300 Bloemfontein, South Africa*

Complete contact information is available at: https://pubs.acs.org/10.1021/acs.jpcc.0c04668

Notes

The authors declare no competing financial interest.

■ ACKNOWLEDGMENTS

The authors would like to acknowledge the National Science Centre in Poland (NCN − Narodowe Centrum Nauki) for the financial support within the Project "Preparation and modulation of spectroscopic properties of $YXZO_4$, where X and Z-P^{5+}, V^{5+}, As^{5+}, doped with 's^2-like' ions and codoped with rare earth ions" (No. UMO-2019/33/B/ST5/02247). We are grateful to M.Sc. E. Bukowska for performing XRPD measurements and to Ph.D. D. Szymanski for SEM-EDS measurements.

■ REFERENCES

(1) Carlos, L. D.; Ferreira, R. A. S.; de Zea Bermudez, V.; Julián-López, B.; Escribano, P. Progress on Lanthanide-Based Organic-Inorganic Hybrid Phosphors. *Chem. Soc. Rev.* **2011**, *40*, 536−549.

(2) Luitel, H. N.; Chand, R.; Torikai, T.; Yada, M.; Watari, T. Highly Efficient NIR-NIR Upconversion in Potassium Substituted Ca-MoO4:Tm3+, Yb3+phosphor for Potential Biomedical Applications. *RSC Adv.* **2015**, *5*, 17034−17040.

(3) Nampi, P. P.; Varma, H.; Biju, P. R.; Kakkar, T.; Jose, G.; Saha, S.; Millner, P. Sodium Yttrium Fluoride Based Upconversion Nano Phosphors for Biosensing. *J. Phys. Conf. Ser.* **2015**, *619*, No. 012043.

(4) Bednarkiewicz, A.; Wawrzynczyk, D.; Nyk, M.; Samoć, M. Tuning Red-Green-White up-Conversion Color in Nano NaYF4:Er/Yb Phosphor. *J. Rare Earths* **2011**, *29*, 1152−1156.

(5) Wangkhem, R.; Singh, N. S.; Singh, N. P.; Singh, S. D.; Singh, L. R. Facile Synthesis of Re-Dispersible YVO4:Ln3+(Ln3+= Dy3+, Eu3+, Sm3+) Nanocrystals: Luminescence Studies and Sensing of Cu2+ions. *J. Lumin.* **2018**, *203*, 341−348.

(6) Shao, J.; Yan, J.; Li, X.; Li, S.; Hu, T. Novel Fluorescent Label Based on YVO4: Bi3+, Eu3+ for Latent Fingerprint Detection. *Dyes Pigm.* **2019**, *160*, 555−562.

(7) Wu, C.-C.; Chen, K. B.; Lee, C.; Sen; Chen, T. M.; Cheng, B. M. Synthesis and VUV Photoluminescence Characterization of (Y,Gd)-(V,P)O4:Eu3+ as a Potential Red-Emitting PDP Phosphor. *Chem. Mater.* **2007**, *19*, 3278−3285.

(8) Fields, R. A.; Birnbaum, M.; Fincher, C. L. Highly Efficient Nd:YVO4 diode - Laser End-Pumped Laser. *Appl. Phys. Lett.* **1987**, *51*, 1885−1886.

(9) Kränkel, C.; Fagundes-Peters, D.; Fredrich, S. T.; Johannsen, J.; Mond, M.; Huber, G.; Bernhagen, M.; Uecker, R. Continuous Wave Laser Operation of Yb3+:YVO4. *Appl. Phys. B* **2004**, *79*, 543−546.

(10) Fields, R. A.; Birnbaum, M.; Fincher, C. L. Highly Efficient Nd:YVO4 Diode-Laser End- Pumped Laser. *Appl. Phys. Lett.* **1987**, *51*, 1885.

(11) O'Connor, J. R. Unusual Crystal-Field Energy Levels and Efficient Laser Properties of YVO4:Nd. *Appl. Phys. Lett.* **1966**, *9*, 407.

(12) Shen, J.; Sun, L. D.; Zhu, J. D.; Wei, L. H.; Sun, H. F.; Yan, C. H. Biocompatible Bright YVO4:Eu Nanoparticles as Versatile Optical Bioprobes. *Adv. Funct. Mater.* 2010, *20* (21), 3708−3714. DOI: 10.1002/adfm.201001264.

(13) Luo, M.; Sun, T. Y.; Wang, J. H.; Yang, P.; Gan, L.; Liang, L. L.; Yu, X. F.; Gong, X. H. Synthesis of Carboxyl-Capped and Bright YVO4:Eu,Bi Nanoparticles and Their Applications in Immunochromatographic Test Strip Assay. *Mater. Res. Bull.* **2013**, *48*, 4454−4459.

(14) Blasse, G.; Bril, A. Investigation of Some Ce3+ - Activated Phosphors. *J. Chem. Phys.* **1967**, *47*, 5139.

(15) Blasse, G.; Bril, A. Photoluminescent Efficiency of Phosphors with Electronic Transitions in Localized Centers. *J. Electrochem. Soc.* **1968**, *115*, 1067−1075.

(16) Delosh, R. G.; Tien, T. Y.; Gibbons, E. F.; Zacmanidis, P. J.; Stadler, H. L. Strong Quenching of Tb3+ Emission by Tb−V Interaction in YPO4−YVO4. *J. Chem. Phys.* **1970**, *53*, 681.

(17) Mraouefel, A.; Guerbous, L.; Boukerika, A.; Diaf, M.; Mendoud, A.; Seraiche, M. Effect of the Vanadium Concentration on Structural and Photoluminescence of YP1-XVxO4: 1 at.% Tb3+ Nanophosphors. *Opt. Mater.* **2017**, *65*, 129−136.

(18) Krumpel, A. H.; Boutinaud, P.; Van Der Kolk, E.; Dorenbos, P.; et al. Charge Transfer Transitions in the Transition Metal Oxides ABO4:Ln3+ and APO4:Ln3+ (A=La, Gd, Y, Lu, Sc; B=V, Nb, Ta; Ln=lanthanide). *J. Lumin.* **2010**, *130*, 1357−1365.

(19) Dorenbos, P.; Krumpel, A. H.; Kolk, E. Van Der.; Boutinaud, P.; Bettinelli, M.; Cavalli, E. Lanthanide Level Location in Transition Metal Complex Compounds. *Opt. Mater.* **2010**, *32*, 1681−1685.

(20) Sohn, K.; Zeon, I. W.; Chang, H.; Lee, S. K.; Park, H. D. Combinatorial Search for New Red Phosphors of High Efficiency at VUV Excitation Based on the YRO4 (R = As, Nb, P, V) System. *Chem. Mater.* **2002**, *14*, 2140−2148.

(21) Huang, Z.; Feng, J.; Pan, W. Theoretical Investigations of the Physical Properties of Zircon-Type YVO4. *J. Solid State Chem.* **2012**, *185*, 42−48.

(22) Cavalli, E.; Angiuli, F.; Mezzadri, F.; Trevisani, M.; Bettinelli, M.; Boutinaud, P.; Brik, M. G. Tunable Luminescence of Bi3+ -Doped YPxV1-XO4 (0=<x=<1). *J. Phys. Condens. Matter* **2014**, *26*, No. 385503.

(23) Dolgos, M. R.; Paraskos, A. M.; Stoltzfus, M. W.; Yarnell, S. C.; Ã, P. M. W. The Electronic Structures of Vanadate Salts: Cation Substitution as a Tool for Band Gap Manipulation. *J. Solid State Chem.* **2009**, *182*, 1964−1971.

(24) Poolton, N. R. J.; Bos, A. J. J.; Jones, G. O.; Dorenbos, P. Probing Electron Transfer Processes in YPO4: Ce, Sm by Combined Synchrotron − Laser Excitation Spectroscopy. *J. Phys. Condens. Matter* **2010**, *22*, No. 185403.

(25) Inoue, Y. Photocatalytic Water Splitting by RuO2-Loaded Metal Oxides and Nitrides with D0- and D10- Related Electronic Configurations. *Energy Environ. Sci.* **2009**, *2*, 364−386.

(26) Errandonea, D.; Kumar, R.; López-Solano, J.; Rodríguez-Hernández, P.; Muñoz, A.; Rabie, M. G.; Sáez Puche, R. Experimental and Theoretical Study of Structural Properties and Phase Transitions in YAsO4 and YCrO4. *Phys. Rev. B.* **2011**, *83*, 1−12.

(27) Ledderboge, F.; Nowak, J.; Massonne, H.; Förg, K.; Höppe, H. A.; Schleid, T. High-Pressure Investigations of Yttrium (III) Oxoarsenate (V): Crystal Structure and Luminescence Properties of Eu3+ - Doped Scheelite-Type Y[AsO4] from Xenotime-Type Precursors. *J. Solid State Chem.* **2018**, *263*, 65−71.

(28) Chakoumakos, B. C.; Abraham, M. M.; Boatner, L. A. Crystal Structure Refinements of Zircon-Type MVO4 (M = Sc, Y, Ce, Pr, Nd, Tb, Ho, Er, Tm, Yb, Lu). *J. Solid State Chem.* **1994**, *109*, 197−202.

(29) Ropp, R. C.; Carroll, B. Yttrium Phosphate-Yttrium Vanadate Solid Solutions and Vegard's Law. *Inorg. Chem.* **1975**, *14*, 2199−2202.

(30) Pan, G.; Song, H.; Dai, Q.; Qin, R.; Bai, X.; Dong, B.; Fan, L.; Wang, F. Microstructure and Optical Properties of Eu3+ Activated YV 1-XPxO4 Phosphors. *J. Appl. Phys.* **2008**, *104* (). DOI: 10.1063/1.3003130.
(31) Strzep, A.; Watras, A.; Zawisza, K.; Boutinaud, P.; Wiglusz, R. J. Forgotten and Resurrected Chernovite-(Y): YAsO4 Doped with Eu3+ Ions as a Potential Nanosized Luminophore. *Inorg. Chem.* **2017**, *56*, 10914−10925.
(32) Wiglusz, R. J.; Bednarkiewicz, A.; Strek, W. Role of the Sintering Temperature and Doping Level in the Structural and Spectral Properties of Eu-Doped Nanocrystalline YVO4. *Inorg. Chem.* **2012**, *51*, 1180−1186.
(33) Kumar, V.; Som, S.; Kumar, V.; Kumar, V.; Ntwaeaborwa, O. M.; Coetsee, E.; Swart, H. C. Tunable and White Emission from ZnO:Tb3+ Nanophosphors for Solid State Lighting Applications. *Chem. Eng. J.* **2014**, *255*, 541−552.
(34) Zhou, X.; Jiang, S.; Xiang, G.; Tang, X.; Luo, X.; Li, L.; Zhou, X. Tunable Emission Color of Li2SrSiO4:Tb3+ Due to Cross-Relaxation Process and Optical Thermometry Investigation. *J. Am. Ceram. Soc.* **2018**, *101*, 3076−3085.
(35) Sobierajska, P.; Wiglusz, R. J. Influence of the Grain Sizes on Stokes and Anti-Stokes Fluorescence in the Yb3+ and Tb3+ Ions Co-Doped Nanocrystalline Fluorapatite. *J. Alloys Compd.* **2019**, *785*, 808−818.
(36) Minakova, T.; Mjakin, S.; Bakhmetyev, V.; Sychov, M.; Zyatikov, I.; Ekimova, I.; Kozik, V.; Chen, Y.; Kurzina, I. Highly Efficient YVPO4 Luminescent Materials Activated by Europium. *Crystals* **2019**, *9*, No. 658.
(37) Boutinaud, P. Rationalization of the Pr3+-to-Transition Metal Charge Transfer Model: Application to the Luminescence of Pr3+ in Titano-Niobates. *J. Lumin.* **2019**, *214*, No. 116557.
(38) Dorenbos, P.; Rogers, E. G. Vacuum Referred Binding Energies of the Lanthanides in Transition Metal Oxide Compounds. *ECS J. Solid State Sci. Technol.* **2014**, *3*, R150−R158.
(39) Dorenbos, P. The Pr3+ and Tb3+ Ground State Locations in Compounds Obtained from Thermoluminescence and Intervalence Charge Transfer Studies. *Opt. Mater.* **2019**, *91*, 333−337.
(40) Dorenbos, P. Modeling the Chemical Shift of Lanthanide 4f Electron Binding Energies. *Phys. Rev. B* **2012**, *85*, No. 165107.
(41) Dorenbos, P. The 4fn-4fn-15d Transitions of the Trivalent Lanthanides in Halogenides and Chalcogenides. *J. Lumin.* **2000**, *91*, 91−106.
(42) Dorenbos, P. f-d Transition Energies of Divalent Lanthanides in Inorganic Compounds. *J. Phys. Condens. Matter* **2003**, *15*, 575−594.
(43) Dorenbos, P. Lanthanide Charge Transfer Energies and Related Luminescence, Charge Carrier Trapping, and Redox Phenomena. *J. Alloys Compd.* **2009**, *488*, 568−573.
(44) Dorenbos, P. Charge Transfer Bands in Optical Materials and Related Defect Level Location. *Opt. Mater.* **2017**, *69*, 8−22.
(45) Dorenbos, P. [INVITED] Improved Parameters for the Lanthanide 4f And 4f−1 5d Curves in HRBE and VRBE Schemes That Takes the Nephelauxetic Effect into Account. *J. Lumin.* **2020**, *222*, No. 117164.
(46) Li, K.; Xue, D. Estimation of Electronegativity Values of Elements in Different Valence States. *J. Phys. Chem. A* **2006**, *110*, 11332−11337.
(47) Dorenbos, P.; Krumpel, A. H.; Van Der Kolk, E.; Boutinaud, P.; Bettinelli, M.; Cavalli, E. Lanthanide Level Location in Transition Metal Complex Compounds. *Opt. Mater.* **2010**, *32*, 1681−1685.
(48) Linares, C.; Louat, A.; Blanchard, M. Rare-Earth - Oxygen Bonding in the LnMO4 Xenotime Structure: Spectroscopic Investigation and Comparative Study of Ligand Field Modesl. In *New Concepts*; Springer: Berlin, Heidelberg, 1977; pp 179−207.
(49) McCarthy, G. J.; Rhyne, J. J.; Silber, H. B. *The Rare Earths in Modern Science and Technology*, 2nd ed.; Plenum Press: New York, 1980.
(50) Dorenbos, P. Relating the Energy of the [Xe]5d1 Configuration of Ce3+ in Inorganic Compounds with Anion Polarizability and Cation Electronegativity. *Phys. Rev. B* **2002**, *65*, No. 235110.
(51) Choudhary, K.; Zhang, Q.; Reid, A. C. E.; Chowdhury, S.; Van Nguyen, N.; Trautt, Z.; Newrock, M. W.; Congo, F. Y.; Tavazza, F. Computational Screening of High-Performance Optoelectronic Materials Using OptB 88 VdW and TB-MBJ Formalisms. *Sci. Data* **2018**, *5*, No. 180082.

https://dx.doi.org/10.1021/acs.jpcc.0c04668
J. Phys. Chem. C 2020, 124, 17364−17371

Supplementary information

P2: *Emission Quenching and First Evidence of Tb^{3+}-to-As^{5+} Charge Transfer in Terbium(III) Ion-Doped $YV_xAs_{1-x}O_4$ Solid-State Solution*

Marta Wujczyk, Adam Watras, Philippe Boutinaud, Marco Bettinelli, Sara Targonska, Jorma Hölsä, Rafal J. Wiglusz

The Journal of Physical Chemistry C, 2020, 124, 31, 17364-17371
DOI: 10.1021/acs.jpcc.0c04668
IF: 4.177

Emission Quenching and First Evidence of Tb^{3+}-to-As^{5+} Charge Transfer in Terbium(III) Ion Doped $YV_xAs_{1-x}O_4$ Solid State Solution

Marta Wujczyk[1], Adam Watras[1], Philippe Boutinaud[2], Marco Bettinelli[3], Sara Targonska[1], Jorma Hölsä[4] and Rafal J. Wiglusz[1*]

[1] *Institute of Low Temperature and Structure Research, PAS, Okolna 2, 50-422 Wroclaw, Poland*

[2] *Université Clermont Auvergne, SIGMA Clermont, Institut de Chimie de Clermont-Ferrand, BP 10448, F-63000 Clermont-Ferrand, France*

[3] *Luminescent Materials Laboratory, Dept. of Biotechnology, University of Verona, Strada Le Grazie 15, 37134 Verona, Italy*

[4] *Department of Physics, University of the Free State, ZA-9300 Bloemfontein, South Africa*

***Keywords*:** yttrium orthovanadate-arsenate, solid state solution, emission quenching , MMCT, terbium, luminescence

*Corresponding author:

E-mail: r.wiglusz@intibs.pl

Phone: +48 (071) 3954159

Fax: +48 (071) 3441029

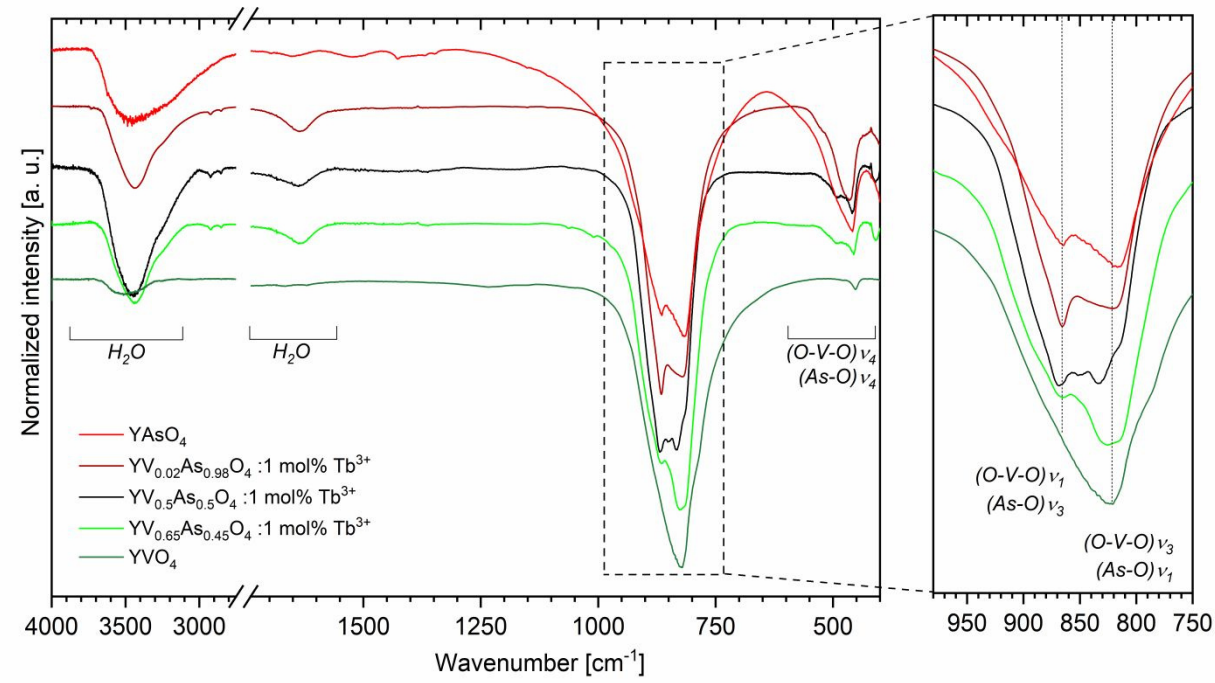

Figure S1. Fourier transform infrared (FT-IR) spectrum of yttrium orthovanadate-arsenate powders.

The infrared spectra of the obtained samples (300 K) are presented in **Figure S1**. The broad bands at 3500 cm^{-1} and 1643 cm^{-1} are attributed to the stretching and bending vibrations of O–H group of H_2O molecule, respectively [1,2]. The FT-IR spectra of yttrium orthovanadate-arsenate structure are characterized by two spectral regions, from 950 cm^{-1} to 750 cm^{-1} and from 550 cm^{-1} to 400 cm^{-1}, respectively. The interpretation of bands related to vanadate and arsenate groups is difficult due to their similarity. Consequently, the bands in the region from 866 to 870 cm^{-1} could be assigned to symmetric-stretching modes of O-V-O and asymmetric-stretching modes of As-O groups. This phenomenon occurs also at 835 cm^{-1} where are located lines corresponded to symmetric-stretching modes of As-O band and asymmetric-stretching modes of O-V-O mode [3–5]. In the lower frequency region the bands at 496 cm^{-1}, 456 cm^{-1} and 410 cm^{-1} are assigned to antisymmetric bending of O-V-O groups [6] as well as of As-O band [7]. The infrared spectra clearly confirm presence of vanadate and arsenate group in assumed yttrium orthovanadate-arsenate structure. Lines corresponded to both groups are observed. The intensity ratio between maximum at 835 cm^{-1} and at 866 cm^{-1} is changed by modification of vanadate group amount. This regularity is also observed in the lower frequency region. Decreasing of the intensity of band at 456 cm^{-1} is caused by increasing of vanadium concentration.

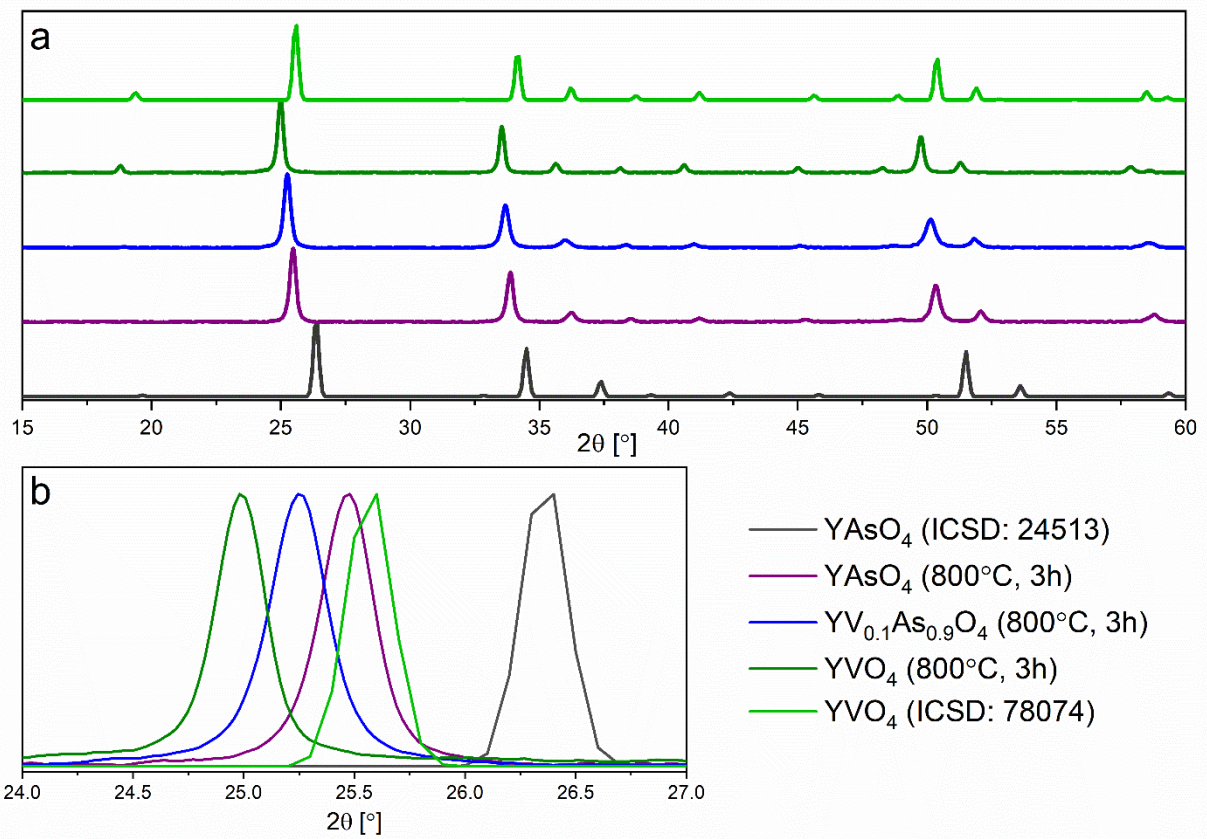

Figure S2. Diffraction data for un-doped matrices of YVO_4, $YV_xAs_{1-x}O_4$ and $YAsO_4$ in comparison to standard ICSD patterns (a) and the dependence of the lattice plane (2 2 0) on shift (b).

Table S1. Unit cell parameters (a,c), cell volume (V), crystallite size as well as refine factor (R_w) for $Tb_{0.01}Y_{0.99}V_xAs_{1-x}O_4$ prepared at 800 °C as a function of V^{5+} ion concentration.

$Tb_{0.01}Y_{0.99}V_xAs_{1-x}O_4$	a (Å)	c (Å)	V (Å3)	Grain size (nm)	R_w (%)	Y-As/V D_{min} (Å)
x = 0.02	7.0329	6.2847	310.85	14.99±0.01	1.38	3.1398
x = 0.05	7.0507	6.2910	312.74	15.51±0.01	1.34	3.1424
x = 0.10	7.0544	6.2927	313.15	15.57±0.01	1.20	3.1432
x = 0.15	7.0619	6.2917	313.77	19.67±0.01	1.14	3.1433
x = 0.20	7.0676	6.2938	314.38	21.56±0.01	1.30	3.1438
x = 0.30	7.0737	6.2930	314.88	19.90±0.01	1.50	3.1434
x = 0.40	7.0775	6.2941	315.28	24.66±0.01	1.26	3.1439
x = 0.50	7.0869	6.2958	316.20	24.31±0.01	1.76	3.1422
x = 0.60	7.0926	6.2937	316.60	22.74±0.01	1.12	3.1412
x = 0.65	7.0963	6.2955	317.03	22.97±0.01	1.49	3.1415

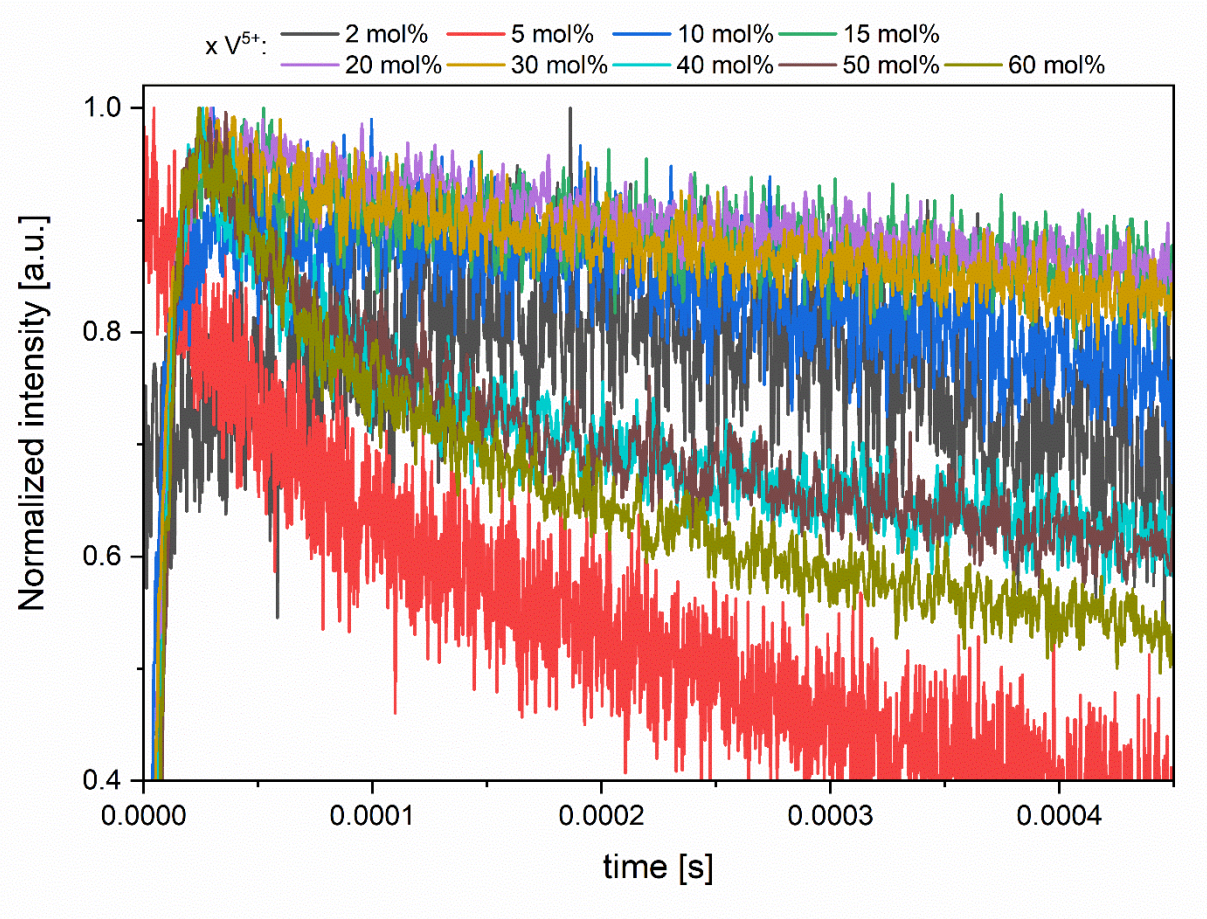

Figure S3. Rise time dependent on the vanadium concentration.

References:

(1) Devi, H. F.; Singh, T. D. Optical Properties of Porous Sm3+ -Doped Yttrium Orthophosphate Nanoparticles Tailored by Co-Precipitation Route. *Opt. Commun.* **2019**, *439* (October 2018), 34–37. https://doi.org/10.1016/j.optcom.2019.01.045.

(2) Niraj Luwang, M.; Ningthoujam, R. S.; Srivastava, S. K.; Vatsa, R. K. Disappearance and Recovery of Luminescence in Bi 3+ , Eu 3+ Codoped YPO 4 Nanoparticles Due to the Presence of Water Molecules Up to 800 °C. *J. Am. Chem. Soc.* **2011**, *133* (9), 2998–3004. https://doi.org/10.1021/ja1092437.

(3) Goldberg, S.; Johnston, C. T. Mechanisms of Arsenic Adsorption on Amorphous Oxides Evaluated Using Macroscopic Measurements, Vibrational Spectroscopy, and

Surface Complexation Modeling. *J. Colloid Interface Sci.* **2001**, *234* (1), 204–216. https://doi.org/10.1006/jcis.2000.7295.

(4) Jia, Y.; Xu, L.; Wang, X.; Demopoulos, G. P. Infrared Spectroscopic and X-Ray Diffraction Characterization of the Nature of Adsorbed Arsenate on Ferrihydrite. *Geochim. Cosmochim. Acta* **2007**, *71* (7), 1643–1654. https://doi.org/10.1016/j.gca.2006.12.021.

(5) Verma, S.; Gupta, R.; Bamzai, K. K. Effect of Mixing Ce 3+ and Nd 3+ Ions in Equimolar Ratio on Structural, Optical and Dielectric Properties on Pure Cerium Orthovanadate and Neodymium Orthovanadate. *Mater. Res. Bull.* **2016**, *81*, 71–84. https://doi.org/10.1016/j.materresbull.2016.05.003.

(6) Nabar, M. .; Mhatre, B. . Studies on Triple Orthovanadates. *J. Alloys Compd.* **2001**, *323–324*, 83–85. https://doi.org/10.1016/s0925-8388(01)00991-4.

(7) Frost, R. L.; López, A.; Scholz, R.; Lana, C.; Xi, Y. A Raman Spectroscopic Study of the Arsenate Mineral Chenevixite Cu 2Fe23+(AsO4)2(OH) 4·H2O. *Spectrochim. Acta - Part A Mol. Biomol. Spectrosc.* **2015**, *135*, 192–197. https://doi.org/10.1016/j.saa.2014.06.091.

P3: *Influence of vanadium concentration on up-conversion luminescence in Er^{3+}–Yb^{3+} and Tm^{3+}–Yb^{3+} ions pair co-doped $YV_xP_{1-x}O_4$ solid state solution*

Marta Wujczyk, Adam Watras, Katarzyna Szyszka, Rafal J. Wiglusz

Journal of Alloys and Compounds, 2021, 884, 161022
DOI: 10.1016/j.jallcom.2021.161022
IF: 6.371

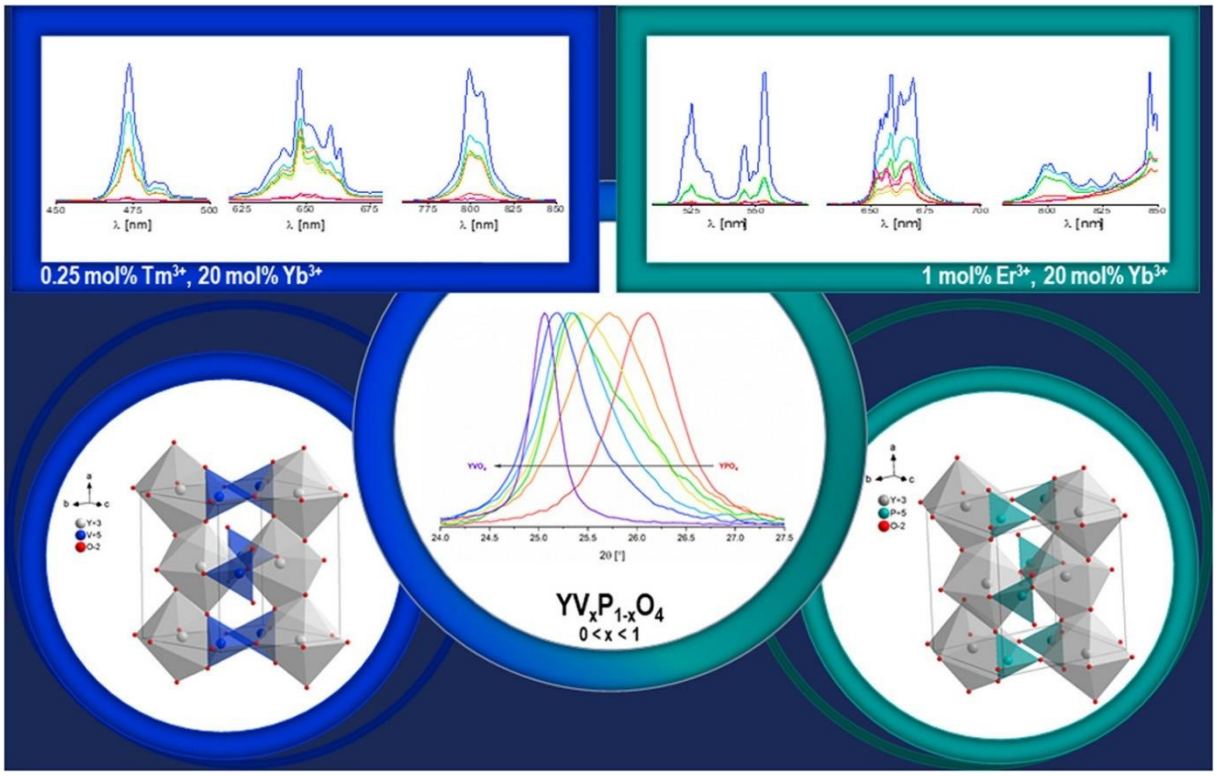

The motivation for the scientific paper entitled "*Influence of vanadium concentration on up-conversion luminescence in Er^{3+}-Yb^{3+} and Tm^{3+}-Yb^{3+} ions pair co-doped $YV_xP_{1-x}O_4$ solid state solution*" was related to the desire to analyse the effect of continuous solid solution structure on up-conversion mechanisms.

The study was aimed to investigate an influence of $YV_xP_{1-x}O_4$ (x = 0.3, 0.4, 0.5, 0.6, 0.7) solid state solution on up-conversion processes in two different type of up-converting ion pairs, Er^{3+}-Yb^{3+} and Tm^{3+}-Yb^{3+}. Concentration of co-dopants was set to 1 mol% Er^{3+}, 20 mol% Yb^{3+} and 0.25 mol% Tm^{3+}, 20 mol% Yb^{3+}.

For that purpose, a series of yttrium orthovanadate-phosphate continuous solid solutions was obtained via co-precipitation synthesis route. By changing the V^{5+}-P^{5+} ratio a shift of XRD planes towards smaller angles was observed. Additionally, broadening of XRD peaks with increasing P^{5+} amount was noted. The broadening of the XRD peaks is related to the ionic size mismatch between the V^{5+} and P^{5+} ions, resulting in defects in the crystallographic structure. The SEM images showed that V^{5+} rich materials are bigger with better defined particle shape, while being less agglomerated in comparison to P^{5+} rich materials.

Spectroscopic properties of $YV_xP_{1-x}O_4$: Er^{3+}-Yb^{3+} and Tm^{3+}-Yb^{3+} were investigated through measurements of emission and dependence of the emission intensity on laser pump power. In emission spectra for $YV_xP_{1-x}O_4$: Er^{3+}-Yb^{3+} observed are characteristic to Er^{3+} ions emission lines. The transitions with the highest intensity are the $^2H_{11/2} \rightarrow {}^4I_{15/2}$ and the $^4S_{3/2} \rightarrow {}^4I_{15/2}$. In these materials, a Tm^{3+} ion contamination was noted. In emission spectra for $YV_xP_{1-x}O_4$: Tm^{3+}-Yb^{3+} noted are characteristic Tm^{3+} ions emission lines. The highest intensity transition is the $^3H_4 \rightarrow {}^3H_6$. For all the solid solutions the power dependence of emission intensity on the laser pump power was measured and calculated. The measurements were carried out for a wide range of the laser power, allowing for the number of photons required for the process to be estimated. Measurements allowed for the processes in the materials to be proposed. The up-conversion processes are indicated in the energy diagram.

In summary the co-precipitation synthesis route led to obtaining $YV_xP_{1-x}O_4$ solid solutions. Based on the conducted spectroscopic measurements the up-conversion processes involved in the emission of Er^{3+} and Tm^{3+} ions were proposed. The ETU, ESA, cooperative sensitization and cross-relaxation mechanisms are described in detail in the paper. The dependence of Er^{3+} ion emission on matrix composition was noted. For materials rich in P^{5+} ions, a change in the intensity of individual 4*f*-4*f* transitions was observed.

The dissertation author contributed to the process of creating the scientific article with:

- Synthesis of the $YV_xP_{1-x}O_4$: Er^{3+}, Yb^{3+} and Tm^{3+}, Yb^{3+} materials;
- Analysis of the XRD patterns;
- Analysis of the SEM images and EDS maps;
- Measurement and analysis of emission and power dependence of the emission intensity;
- Preparation of the graphics, schemes, and charts;
- Co-writing and co-editing the manuscript.

Journal of Alloys and Compounds 884 (2021) 161022

Contents lists available at ScienceDirect

Journal of Alloys and Compounds

journal homepage: www.elsevier.com/locate/jalcom

Influence of vanadium concentration on up-conversion luminescence in Er^{3+}–Yb^{3+} and Tm^{3+}–Yb^{3+} ions pair co-doped $YV_xP_{1-x}O_4$ solid state solution

Marta Wujczyk, Adam Watras, Katarzyna Szyszka, Rafal J. Wiglusz*

Institute of Low Temperature and Structure Research, PAS, Okolna 2, 50-422 Wroclaw, Poland

ARTICLE INFO

Article history:
Received 25 February 2021
Received in revised form 28 June 2021
Accepted 29 June 2021
Available online 2 July 2021

Keywords:
Solid state solution
Yttrium orthovanadate
Yttrium orthophosphate
Lanthanide ions
Up-conversion

ABSTRACT

The paper is focused on an influence of vanadium ions on the up-conversion processes in nanosized $YV_xP_{1-x}O_4$ solid state solution. As a consequence, two series of $YV_xP_{1-x}O_4$ (where x = 0–1) materials has been obtained via co-precipitation method. Yttrium orthovanadate-phosphate has been co-doped with the up-converting Er^{3+}-Yb^{3+} and Tm^{3+}-Yb^{3+} lanthanide ion pairs. Obtained series of nanosized materials has been investigated for phase purity, chemical composition, morphology by the means of X-Ray Powder Diffraction (XRD) and Scanning Electron Microscope (SEM). Photoluminescence properties of 0.25 mol% Tm^{3+}, 20 mol% Yb^{3+}:$YV_xP_{1-x}O_4$ (x = 0, 0.3, 0.4, 0.5, 0.6, 0.7, 1), and 1 mol% Er^{3+}, 20 mol% Yb^{3+}:$YV_xP_{1-x}O_4$ (x = 0, 0.3, 0.4, 0.5, 0.6, 0.7, 1) were investigated in detail. It has been found that increase of the vanadium content leading to better up-conversion luminescence.

1. Introduction

Recently, rare earth doped and co-doped yttrium orthooxides have attracted an astonishing interest and have been investigated as phosphors for UV, Vis, and NIR excitations. The interest of YXO_4 (where X = As, Cr, P, V) is related to physicochemical properties such as high-temperature stability, resistivity to photo degradation, insolubility in water [1]. Among the extensive studies of the YXO_4 matrices it was also investigated for occurrence of up- and down-conversion processes [2–10]. Although, to the best of our knowledge up-conversion processes in the mixed $YV_xP_{1-x}O_4$ solid solutions have not been investigated.

Yttrium orthovanadate as well as yttrium orthophosphate crystallize in the tetragonal system and are ascribed by $I4_1/amd$ space group [11,12]. Moreover, yttrium orthovanadate is isostructural to yttrium orthophosphate. Therefore, a solid-state solution with general formula YVxP1-xO4 may be obtained. The unit cell is built out of the yttrium octahedral and vanadium tetrahedral, which is statistically substituted by phosphorus tetrahedral groups. Yttrium ions are also substituted in a statistical manner, when doped or co-doped with lanthanide ions (i.e., Tm^{3+}, Er^{3+} and Yb^{3+} ions).

Up-conversion (UC) processes are based on the energy conversion from low energy (IR, NIR) to the higher energy (UV, Vis). F. Auzel [13] has compartmentalized UC processes into six different processes: ESA (Excited State Absorption), APTE/ETU (Addition de Photon par Transfers d'Energie/Energy Transfer Up-conversion), cooperative sensitization, cooperative luminescence, second harmonic generation (SHG) and 2-photon absorption excitation. Although, the quantum efficiency (QE) of the up-conversion processes is relatively low, ETU and ESA processes present highest quantum efficiency out of the mentioned processes [13].

This paper is focused on an investigation of the up-conversion processes that are influenced by concentration of vanadium ions in $YV_xP_{1-x}O_4$ matrix. The concentration of the vanadium ions is in the range of $0 \le x \le 1$ in respect to the appropriate phosphorus molar content. Moreover, two pairs of co-dopants related to Tm^{3+}-Yb^{3+} and Er^{3+}-Yb^{3+} ions were used. In both cases, 20 mol% Yb^{3+} ion was chosen as a sensitizer and 0.25 mol% Tm^{3+} as well as 1 mol% Er^{3+} ions were chosen as activators. The series of 0.25 mol% Tm^{3+}, 20 mol% Yb^{3+}:$YV_xP_{1-x}O_4$ (where x = 0, 0.3, 0.4, 0.5, 0.6, 0.7, 1) and 1 mol% Er^{3+}, 20 mol% Yb^{3+}:$YV_xP_{1-x}O_4$ (where x = 0, 0.3, 0.4, 0.5, 0.6, 0.7, 1) samples were obtained via co-precipitation synthesis method and thereafter heat-treated at 800 °C for 3 h.

* Corresponding author.
E-mail address: r.wiglusz@intibs.pl (R.J. Wiglusz).

https://doi.org/10.1016/j.jallcom.2021.161022
0925-8388/

Table 1
Crystallographic data for yttrium orthovanadate and yttrium orthophosphate [14,15].

	YVO_4	YPO_4
cryst. syst.	zircon tetragonal	zircon tetragonal
space group	$I4_1/amd$ (no.141)	$I4_1/amd$ (no.141)
a **(Å)**	7.1183(1)	6.8947(6)
b **(Å)**	7.1183(1)	6.8947(6)
c **(Å)**	6.2893(1)	6.0276(6)
α (°)	90	90
β (°)	90	90
γ (°)	90	90
point-group symmetry	D_{4h}	D_{4h}
coordination no.	Y(8); V(4); O(3)	Y(8); P(4); O(3)

2. Experimental

2.1. Synthesis

Nano-sized yttrium orthovanadate-phosphate doped with ytterbium-thulium and ytterbium-erbium ions were prepared by wet chemical synthesis via co-precipitation method. Concentration of the optically active ions was set to 0.25 mol% Tm^{3+}, 20 mol% Yb^{3+} and 1 mol% Er^{3+}, 20 mol% Yb^{3+} for each material, in respect to the appropriate Y^{3+} molar content. The V^{5+} ions concentration was changed from 30 to 70 mol%, respective to the appropriate P^{5+} molar content. Analytical grade Y_2O_3 (99.99% Alfa Aesar), Tm_2O_3 (99.99% Alfa Aesar), Yb_2O_3 (99.99% Alfa Aesar), Er_2O_3 (99.99% Alfa Aesar), $(NH_4)_2HPO_4$ (> 98% ACROS Organics) and NH_4VO_3 (99.5% Sigma-Aldrich) were used as the starting materials.

In this method, stoichiometric amounts of the lanthanide oxides were digested in an excess of 65% HNO_3 (about 2 ml; Suprapur® Merck) to transform them into nitrate salts. The obtained lanthanide nitrates were re-crystallized three times to get rid of the HNO_3 excess. Ammonium metavanadate and diammonium phosphate were dissolved in deionized water separately. Next, $(NH_4)_2HPO_4$ and NH_4VO_3 solutions were mixed and thereafter nitrate salts solution was added ($Y(NO_3)_3$, $Tm(NO_3)_3$, $Yb(NO_3)_3$ and $Y(NO_3)_3$, $Er(NO_3)_3$, $Yb(NO_3)_3$). Reaction (about 150 ml) was maintained at a stirring plate for 1.5 h at approximately 70 °C. The pH of the suspension was adjusted to 9 with aqueous ammonia (25% Avantor Poland). The obtained precipitate was washed and centrifuged at least thrice to reach neutral pH value. The as-prepared materials were dried for 24 h at 70 °C and heat-treated at 800 °C for 3 h to form crystallized nanoparticles.

2.2. XRD and SEM analysis

The development of the crystal phase was analysed via X-ray diffraction (XRD). The diffractograms were collected with an X'Pert PRO X-ray diffractometer (Cu Kα1, 1.54060 Å) (PANalytical). The XRD patterns were assigned to standard patterns from Inorganic Crystal Structure Database (ICSD) and thereafter analysed. Analysis of the size and morphology, as well as dispersibility of the $YV_xP_{1-x}O_4$ was performed on the SEM (Scanning Electron Microscope) FEI Nova NanoSEM 230 equipped with an EDS spectrometer (EDAX Genesis XM4).

2.3. Spectroscopic analysis

Emission spectra were recorded upon 980 nm excitation with diode laser (CW) at 300 K. A Schott KG5 and THORLABS FESH0850 were used as filters. For the measurements of up-conversion emission of 1 mol% Er^{3+}, 20 mol% Yb^{3+}: $YV_xP_{1-x}O_4$ only THORLABS FESH0850 filter was used. Two filters were used for up-conversion emission of 0.25 mol% Tm^{3+}, 20 mol% Yb^{3+}: $YV_xP_{1-x}O_4$. THORLABS FESH0850 filter does not fully transmit in 450 – 500 nm spectral region. Schott KG5 filter transmits in 450 – 500 nm but not in 600 – 800 spectral regions. Therefore, the presented emission spectra of 0.25 mol% Tm^{3+}, 20 mol% Yb^{3+}: $YV_xP_{1-x}O_4$ are compiled from two measurements preformed on the same setup, varying only on applied filter. The Hamamatsu PMA-12 photonic multichannel analyser was used as an optical detector. Power dependence of the up-conversion emission intensity was performed for a wide range of laser pump power 0.05–1.4 W, while excited upon 980 nm at 300 K. Data was fitted in respect to the following formula:

$$N_i \sim P^n, \quad (1)$$

where P – absorbed pump power, n – number of sequentially absorbed photons, N – population density of i state.

3. Results and discussion

3.1. Structure and morphology

The crystal structure of YXO_4 (where X = P, V) group of compounds is tetragonal with space group $I4_1/amd$ (No. 141), with only one cationic site for yttrium, which is substituted by rare earth ions

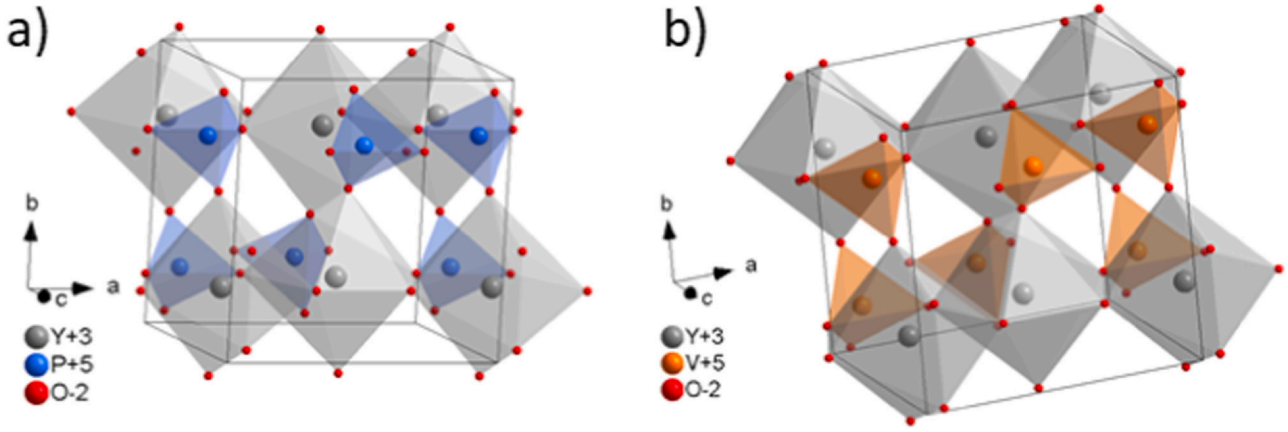

Fig. 1. 3D view of the YPO_4 (a) and YVO_4 (b) unit cells.

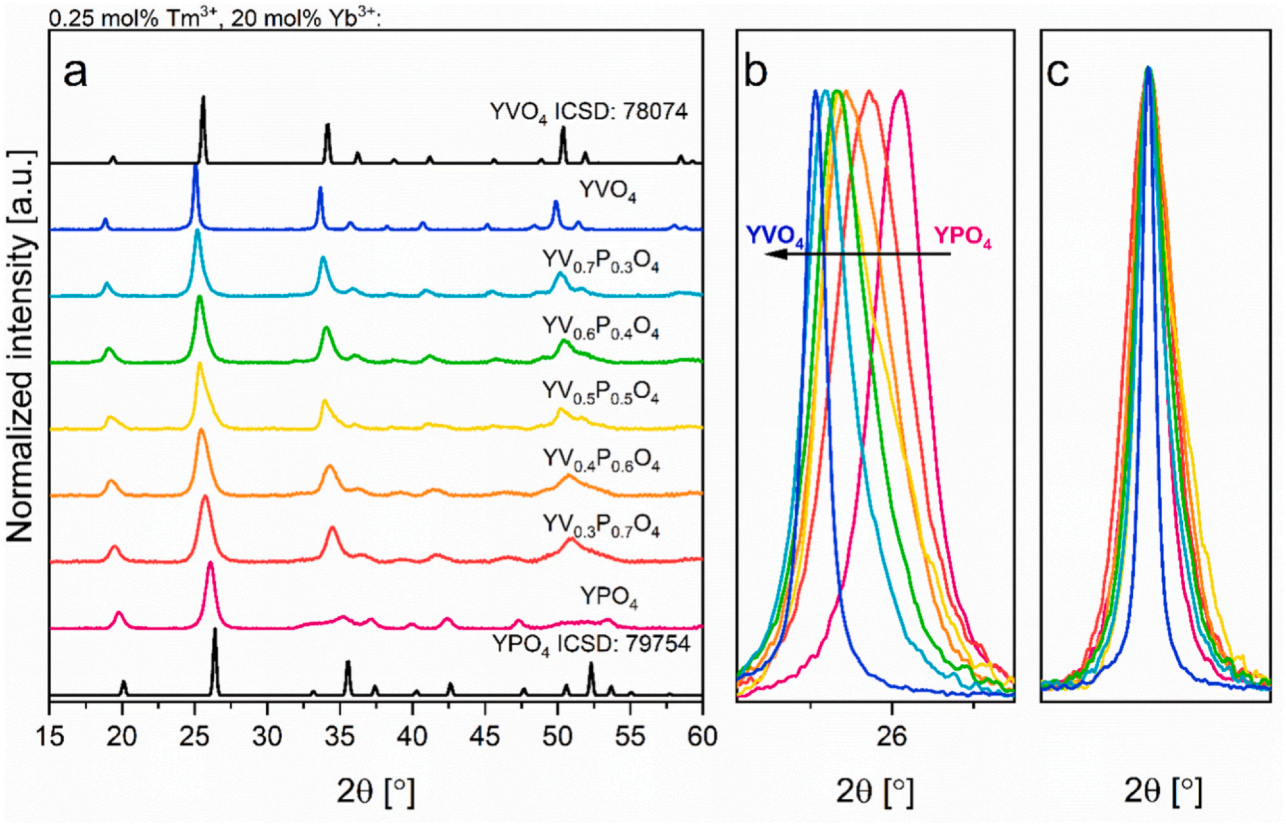

Fig. 2. X-ray diffraction patterns (a), 2theta shift (b) and (c) centered peak for bandwidth analysis, obtained for 0.25 mol% Tm^{3+}, 20 mol% Yb^{3+}:$YV_xP_{1-x}O_4$ thermally treated at 800 °C for 3 h.

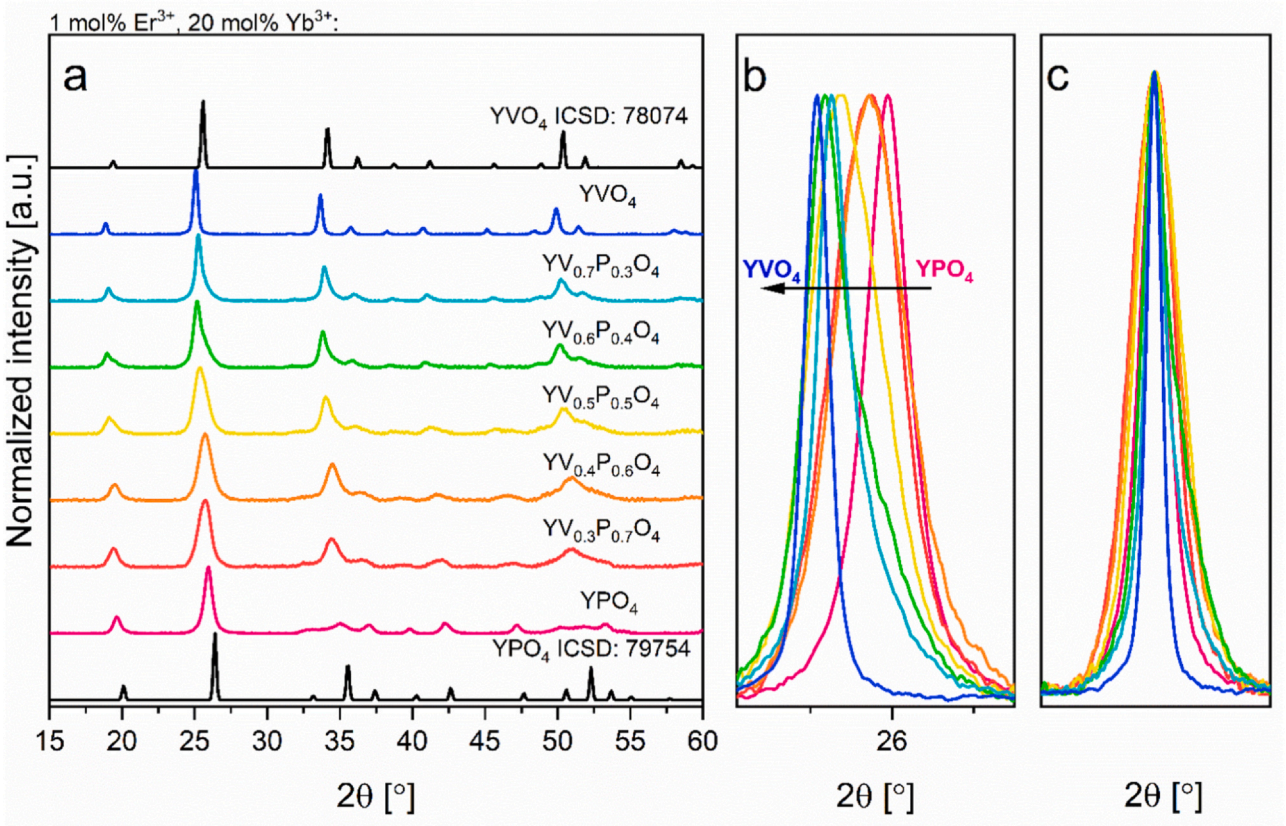

Fig. 3. X-ray diffraction patterns (a), 2θ shifts (b) and (c) centered peak for bandwidth analysis, obtained for 1 mol% Er^{3+}, 20 mol% Yb^{3+}:$YV_xP_{1-x}O_4$ thermally treated at 800 °C for 3 h.

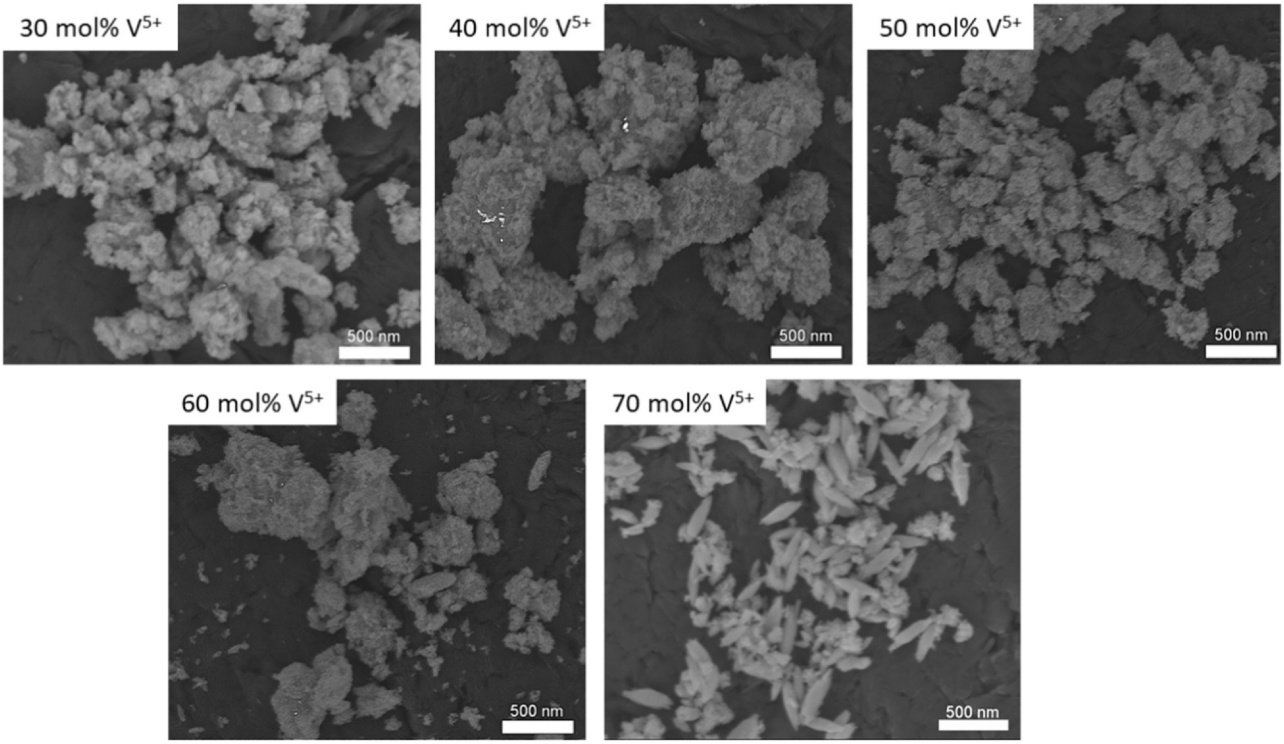

Fig. 4. SEM images obtained for 1 mol% Er^{3+}, 20 mol% Yb^{3+}:$YV_xP_{1-x}O_4$ thermally treated at 800 °C for 3 h.

(Tm^{3+}, Er^{3+}, Yb^{3+}). Unit cell parameters of the YVO_4 and YPO_4 are listed in Table 1.

As it was already presented in the case of $YV_xP_{1-x}O_4$ and Eu^{3+}:$YV_xP_{1-x}O_4$ obtaining the solid solution via co-precipitation method is possible [16,17]. Therefore, the $YV_xP_{1-x}O_4$ system co-doped with up-converting ions (Tm^{3+}, Er^{3+}, Yb^{3+}) should also be in accordance with the Vegard's law for solid solutions.(Fig. 1).

The formation of pure crystal phase of $YV_xP_{1-x}O_4$ solid solution was affirmed by the means of X-ray powder diffraction measurements (see Fig. 2 and 3). Crystal phase purity was obtained for the heat-treated materials differing in vanadium to phosphor ratio and in co-dopants (0.25 mol% Tm^{3+}, 20 mol% Yb^{3+} and 1 mol% Er^{3+}, 20 mol% Yb^{3+}). A continuous shift of the planes towards lower 2θ angles was observed and this is a confirmation of the unit cell parameters change. The change is forced by the substitution of the bigger V^{5+} (0.36 Å at C.N. 4) cation by smaller one P^{5+} (0.17 Å at C.N. 4) (**see** Fig. 2**b** and **3b**). Diffraction line broadening is observed for the solid solutions, when compared to the YPO_4 and YVO_4 matrices obtained at the equivalent synthesis conditions (**see** Fig. 2**c** and 3**c**). Broadening of the diffraction lines can possibly be a consequence of the lattice strain in the crystal lattice [18] and P^{5+} ions are substituted by V^{5+} ions. The strain may originate from the ionic size incompatibility between V^{5+} and P^{5+} ions. The lattice strain can be associated with the grain-interior dislocations [19], grain-boundary dislocations [20] and excess volume of grain boundaries (vacancies, vacancy clusters) [21]. Similar broadening of the XRD lines for $YV_xP_{1-x}O_4$ solid solution was observed by Nguyen H.D. et al. [22], were investigated materials were doped with bismuth and europium ions. Therefore it may be concluded that, the change of the

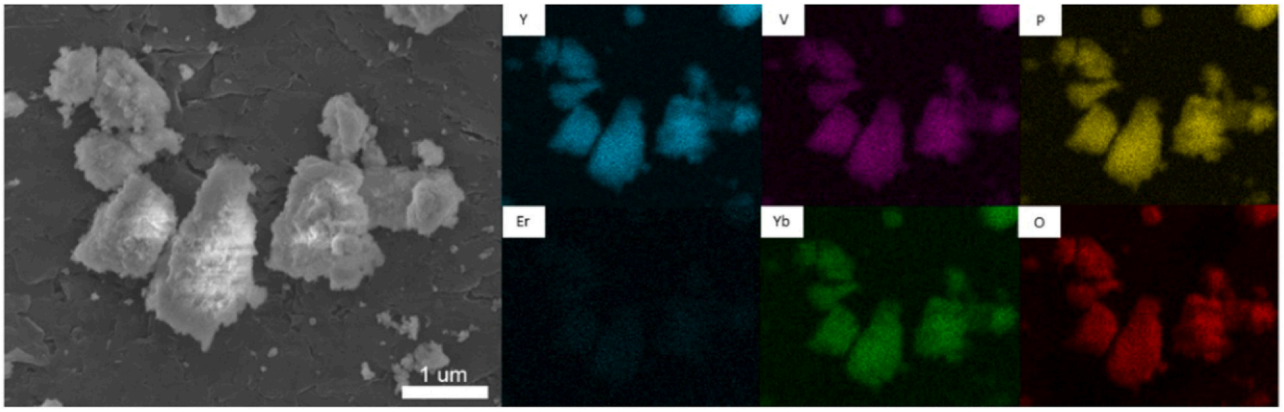

Fig. 5. EDS maps obtained for 1 mol% Er^{3+}, 20 mol% Yb^{3+}:$YV_{0.5}P_{0.5}O_4$ thermally treated at 800 °C for 3 h.

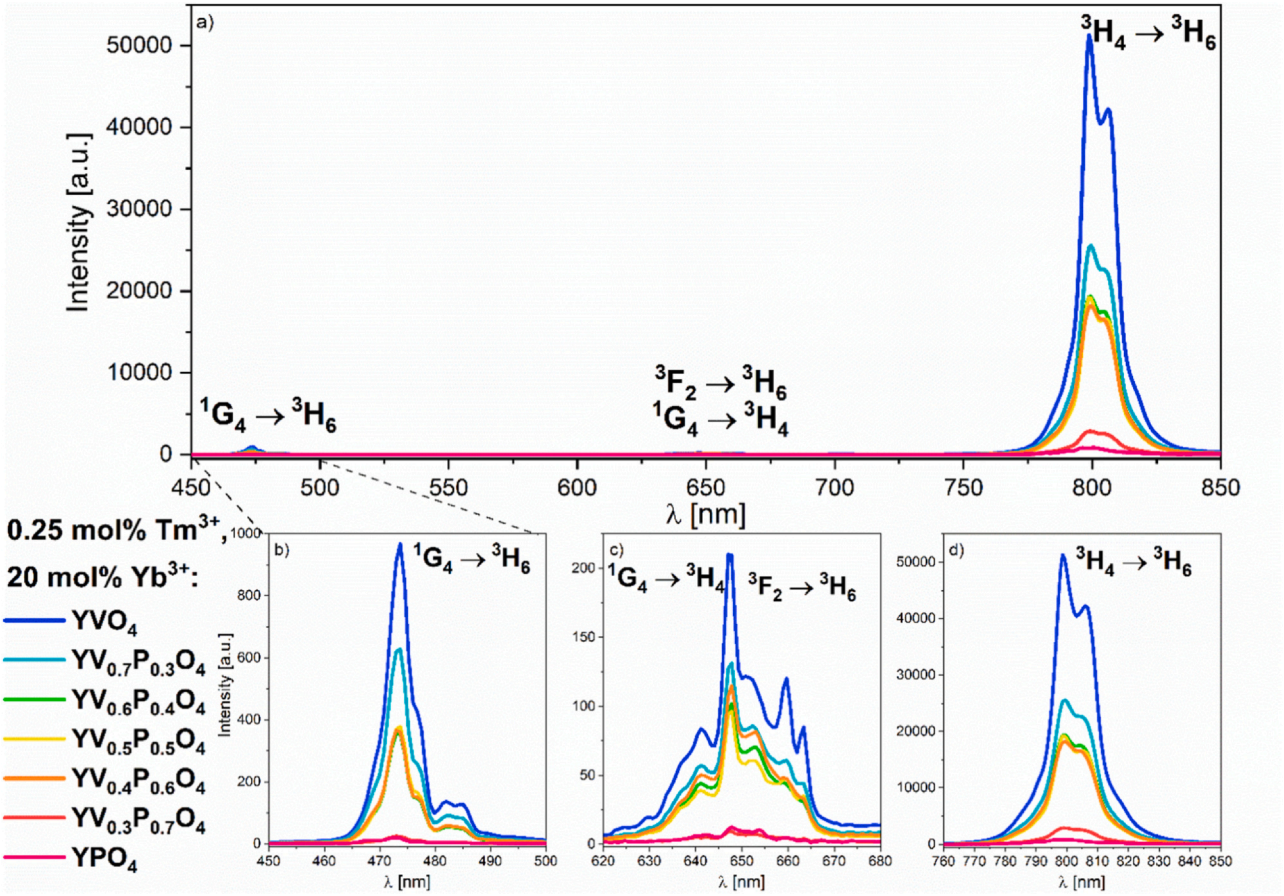

Fig. 6. Emission spectra of 0.25 mol% Tm^{3+}, 20 mol% Yb^{3+}:$YV_xP_{1-x}O_4$ under 980 nm excitation in room temperature.

diffraction lines width is not dependent on co-doping ions, but rather on the ionic radii mismatch between P^{5+} and V^{5+}.

SEM images are presented for the representative 0.25 mol% Tm^{3+}, 20 mol% Yb^{3+}:$YV_xP_{1-x}O_4$ material series, each thermally treated at 800 °C for 3 h (Fig. 4). Materials with low vanadium concentration have smaller and more agglomerated particles. On the contrary, the material with highest vanadium concentration presents less agglomerated and bigger particles with pellet or spindle like morphology. EDS maps (Fig. 5) present distribution of the ions in the representative 0.25 mol% Tm^{3+}, 20 mol% Yb^{3+}:$YV_{0.5}P_{0.5}O_4$ material's particles. Constituents are distributed evenly in the matrix structure and no conspicuous aggregation of the dopants is observed.

3.2. Spectroscopic properties

Up-conversion emission spectra of the 0.25 mol% Tm^{3+}, 20 mol% Yb^{3+}:$YV_xP_{1-x}O_4$ and 1 mol% Er^{3+}, 20 mol% Yb^{3+}:$YV_xP_{1-x}O_4$ are shown in Fig. 6 and Fig. 7, respectively. Emission spectra obtained for the materials containing Tm^{3+} and Yb^{3+} ions present visible transitions at around 473 nm, 645 nm, 660 nm and 800 nm, ascribed as the $^1G_4 \rightarrow {}^3H_6$, $^1G_4 \rightarrow {}^3H_4$, $^3F_2 \rightarrow {}^3H_6$, $^3H_4 \rightarrow {}^3H_6$ Tm^{3+} *f-f* transitions, respectively. The material with the highest emission intensity is 0.25 mol% Tm^{3+}, 20 mol% Yb^{3+}:YVO_4 and the material with the weakest is 0.25 mol% Tm^{3+}, 20 mol% Yb^{3+}:YPO_4. Intensity of the emission steadily increases with the increase of vanadium ions concentration in materials. No change in the shape of the transition bands was observed. No additional emission was recorded. No other evident influence of vanadium was observed than the emission intensity enhancement when introduced to the YPO_4 matrix.

Up-conversion emission spectra obtained for the 1 mol% Er^{3+}, 20 mol% Yb^{3+} material series, while excited under 980 nm at 300 K, present characteristic emission lines of erbium ions. The emission lines observed at 525 and 547 nm are attributed to the $^2H_{11/2} \rightarrow {}^4I_{15/2}$ and $^4S_{3/2} \rightarrow {}^4I_{15/2}$ transitions of Er^{3+} ions (sensitizer), respectively. Emission at around 650 nm is assigned to the $^4F_{9/2} \rightarrow {}^4I_{15/2}$ transition. Emission observed at 820 nm, 830 nm and 849 nm is associated with the $^4F_{7/2} \rightarrow {}^4I_{11/2}$, $^2H_{9/2} \rightarrow {}^4I_{11/2}$ and $^2H_{11/2} \rightarrow {}^4I_{13/2}$ transitions within erbium ions. Intensity of the emission simultaneously increases with the increase of vanadium ions concentration in materials. Additionally, the share of the respective transition bands changes in reference to the total emission, this relation is presented in Fig. 8.

With an increase of vanadium concentration in solid solution, a contribution of the $^4F_{9/2} \rightarrow {}^4I_{15/2}$ transition band decreases in favor of both the $^2H_{11/2} \rightarrow {}^4I_{15/2}$ and $^4S_{3/2} \rightarrow {}^4I_{15/2}$ transition bands (see Fig. 8). Additionally, solid solutions differ in emission band shapes. The difference is prominent in materials with marginal values of the

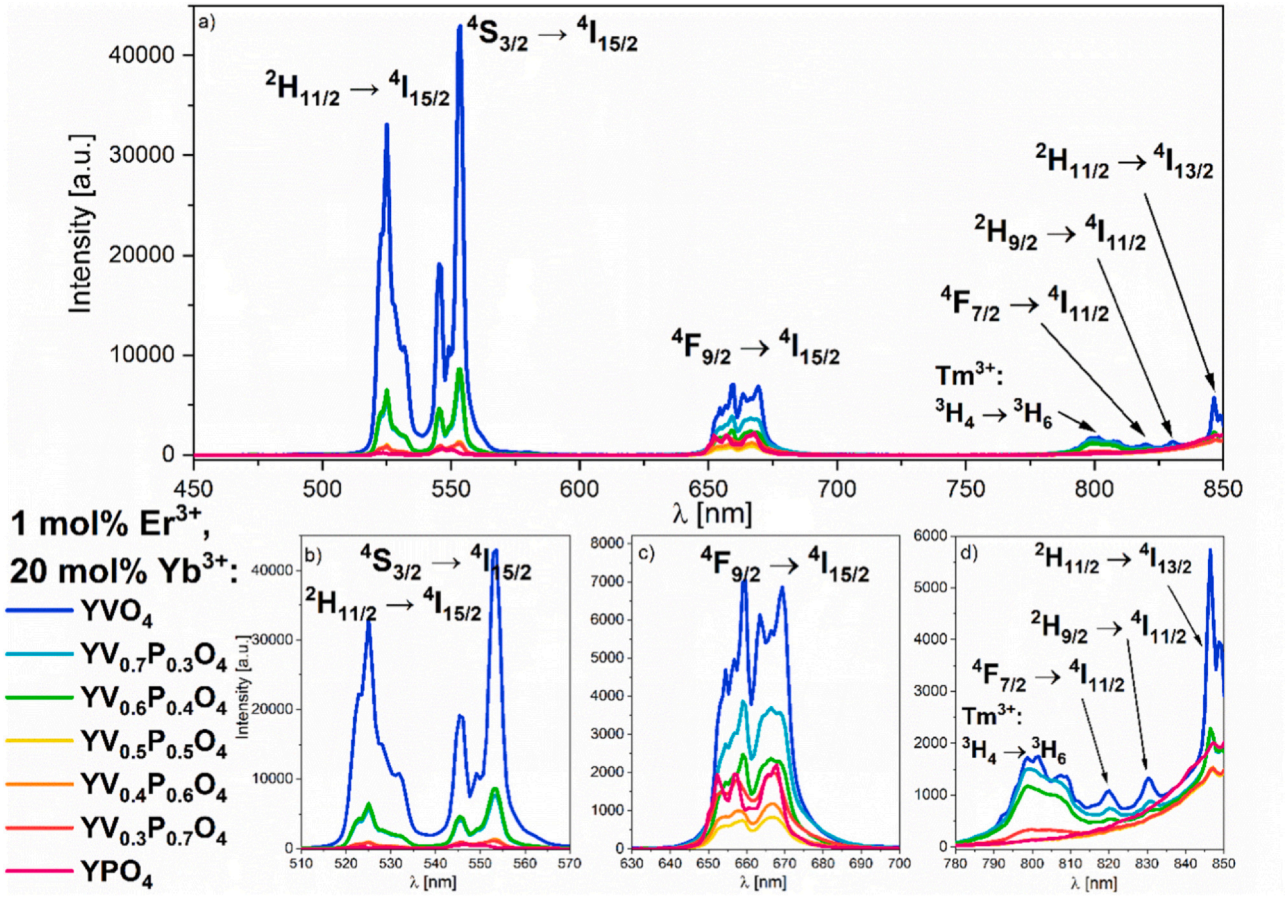

Fig. 7. Emission spectra of 1 mol% Er^{3+}, 20 mol% Yb^{3+}:$YV_xP_{1-x}O_4$ under 980 nm excitation at room temperature.

vanadium concentration (30 mol% V^{5+} and 70 mol% V^{5+}). The $^4F_{9/2} \rightarrow {}^4I_{15/2}$ transition contribution changing with increasing P^{5+} concentration may be caused by the occurring cross-relaxation (CR) processes. Population of the $^4F_{9/2}$ level is directly corelated with CR processes and its happening is dependent on the distance between two adjacent Er^{3+} ions in crystal lattice. In case of $YV_xP_{1-x}O_4$ the unit cell size visibly changes, where YPO_4 unit cell size being much smaller than YVO_4 due to different ionic radii of P^{5+} and V^{5+}. Therefore, the distance between two Er^{3+} ions in material containing low concentration of vanadium is shorter, hence it may be direct cause behind the increase in the intensity of the $^4F_{9/2} \rightarrow {}^4I_{15/2}$ transition.

The intensity of the up-conversion process increases with the increase of vanadium ions concentration in both Er/Yb and Tm/Yb co-doped materials. This means that vanadium ions have positive impact on emission intensity, independently on the used pairs of upconverting ions in this material. Moreover, the shape of particular transitions as well as the ratio of particular transition is influenced by vanadium ions concentration and is much more visible in case of Er/Yb ions pair.

A double logarithmic dependence of the integrated intensity versus laser pump power was investigated for each up-converting ions pair (Figs. 9, 10). Measurements were performed in a wide range of the laser pump power 0.05 – 1.43 W. Power dependence (PD) functions were determined for the $^2H_{11/2}$, $^4S_{3/2}$, $^4F_{9/2} \rightarrow {}^4I_{15/2}$ transitions and for the $^1G_4$, $^3H_4 \rightarrow {}^3H_6$ transitions for each material. According to the equations described by M. Pollnau (Eq. 1), the amount of photons needed for the up-conversion process can be estimated from the slope of the PD function [23]. Estimated number of photons is marked with the symbol *n* and is listed in inserted table in Figs. 9 and 10 for every material. Linear nature of the power dependence's function slope is reaffirming domination of the up-conversion processes over the linear decay from the indirect excited states. The 1 mol% Er^{3+}, 20 mol% Yb^{3+}:$YV_xP_{1-x}O_4$ (Fig. 9) independently on the vanadium concentration yielded *n* value equal to 2. Therefore, the two-photon nature behind population of the $^4F_{9/2}$, $^2H_{11/2}$ and $^4S_{3/2}$ states is confirmed. The 0.25 mol% Tm^{3+}, 20 mol% Yb^{3+}:$YV_xP_{1-x}O_4$ (Fig. 10) independently on the vanadium concentration yielded *n* value equal to 2 for the $^1G_4 \rightarrow {}^3H_6$ and $^3H_4 \rightarrow {}^3H_6$ transitions. Based on power dependence functions presented in Fig. 10b, it can be

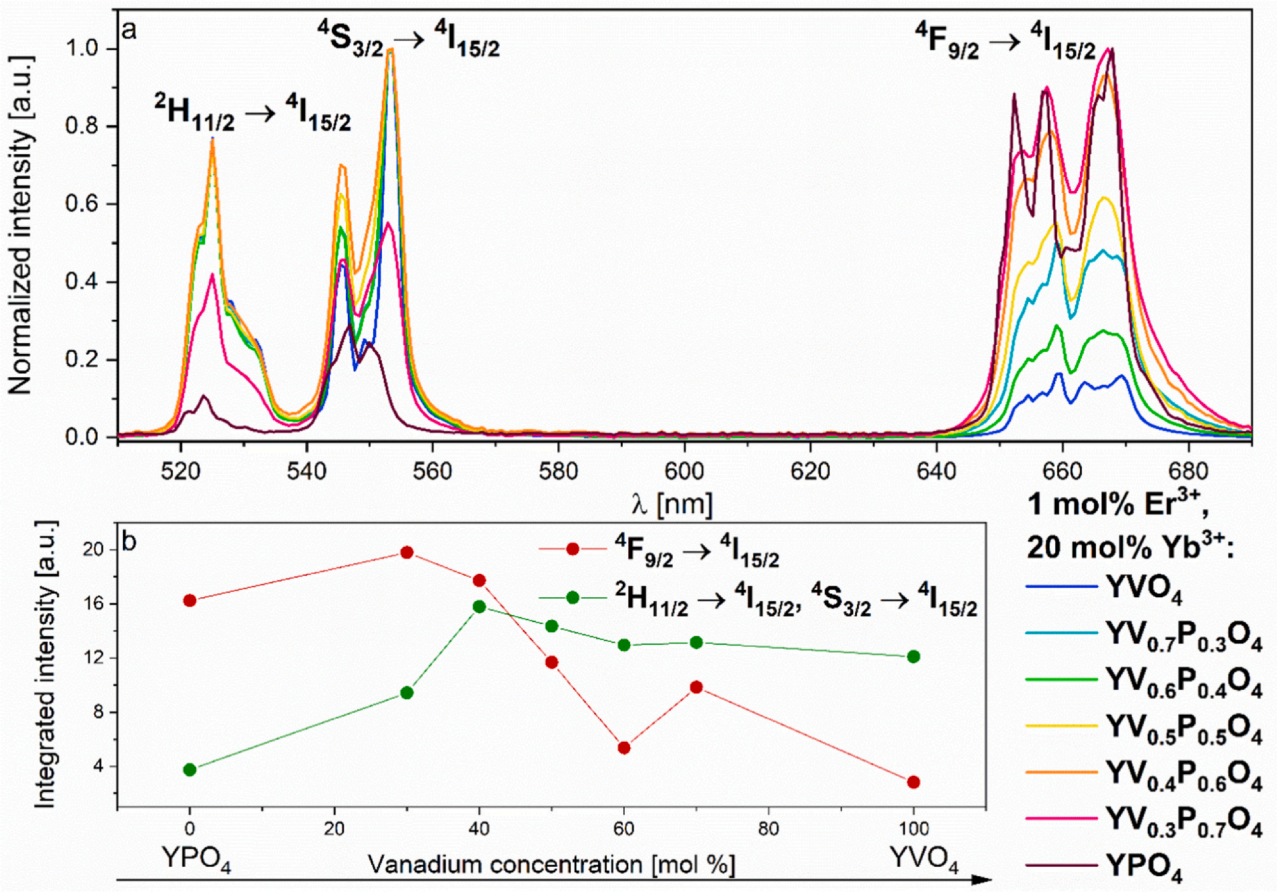

Fig. 8. Emission spectra of 1 mol% Er^{3+}, 20 mol% Yb^{3+}:$YV_xP_{1-x}O_4$ with normalized emission intensity (a) and of the integrated emission intensity dependence on vanadium concentration (b).

suggested that population of the $^1G_4$ state involves absorption of the two subsequent photons. Although, in order to populate the $^1G_4$ state, three photons need to be subsequently absorbed, when excited under 980 nm [24]. Decrease of the *n* value to 2 can be explained by the increase of the energy transfer rate from the sensitizer Yb^{3+} to the activator Tm^{3+} and additional contribution of the cooperative sensitization process to populate $^1G_4$, via Yb^{3+}-Yb^{3+} to Tm^{3+} energy transfer [25,26]. Possible pathways for the population of the $^1G_4$ state are given in Fig. 10.

The energy levels schemes in Fig. 11 and Fig. 12 shows the proposed model pathway for up-conversion processes occurring between Tm^{3+}-Yb^{3+} and Er^{3+}-Yb^{3+} ions in $YV_xP_{1-x}O_4$ solid state solution. Proposed pathways concern a series of $YV_xP_{1-x}O_4$ materials due to the fact related to emission spectra (Figs. 6 and 7) only vary in respective intensities and no additional *f-f* transition bands are found. Excitation wavelength is directly resonant with the sensitizer's (Yb^{3+}) large absorption cross section, its energy can be transferred to the activators (Tm^{3+}, Er^{3+}) with ease [27–29].

Within materials co-doped with 0.25 mol% Tm^{3+} and 20 mol% Yb^{3+} the process proceeding the ETU is Ground State Absorption (GSA), marked with black, solid arrow in the Fig. 11**.** Energy Transfer Up-conversion (ETU) process between the sensitizer (Yb^{3+}) and the acceptors (Er^{3+} and Tm^{3+}) is marked with black, bended arrows insinuating energy transfer from the sensitizer to the acceptors. Population of the Tm^{3+} upper levels is preceded by energy transfer from Yb^{3+} ions in the thulium-ytterbium co-doped materials. Although, the population of the $^3F_4$ level is more complex. The $^3F_4$ level can be populated via two possible pathways by the non-resonant ground state absorption of initial light (black, solid arrow), followed by non-radiative relaxation to the $^3H_5$, further depopulated to the $^3F_4$. Additionally, the $^3F_4$ is populated by the non-resonant energy transfer (black, bended arrow) from the pumped $^2F_{5/2}$ level in Yb^{3+} ion to the $^3H_5$ state in Tm^{3+} ion and later, depopulated to the $^3F_4$. Further, the $^3F_2$ state is populated by the non-resonant energy transfer from the $^2F_{5/2}$ level (Yb^{3+}), then followed by emission to the ground state ($^3F_2 \rightarrow {}^3H_6$ at 660 nm) or by non-radiative relaxation to the $^3H_4$. After that emission may be observed at 798 nm ($^3H_4 \rightarrow {}^3H_6$). Subsequently, the $^1G_4$ level may also be populated by the non-resonant energy transfer from the $^2F_{5/2}$ level (Yb^{3+}). Two emission bands are observed from the $^1G_4$ level, first associated with the $^1G_4 \rightarrow {}^3H_6$ transition at 473 nm and second associated with the $^1G_4 \rightarrow {}^3F_4$ transition at 647 nm. Cooperative sensitization up-conversion is

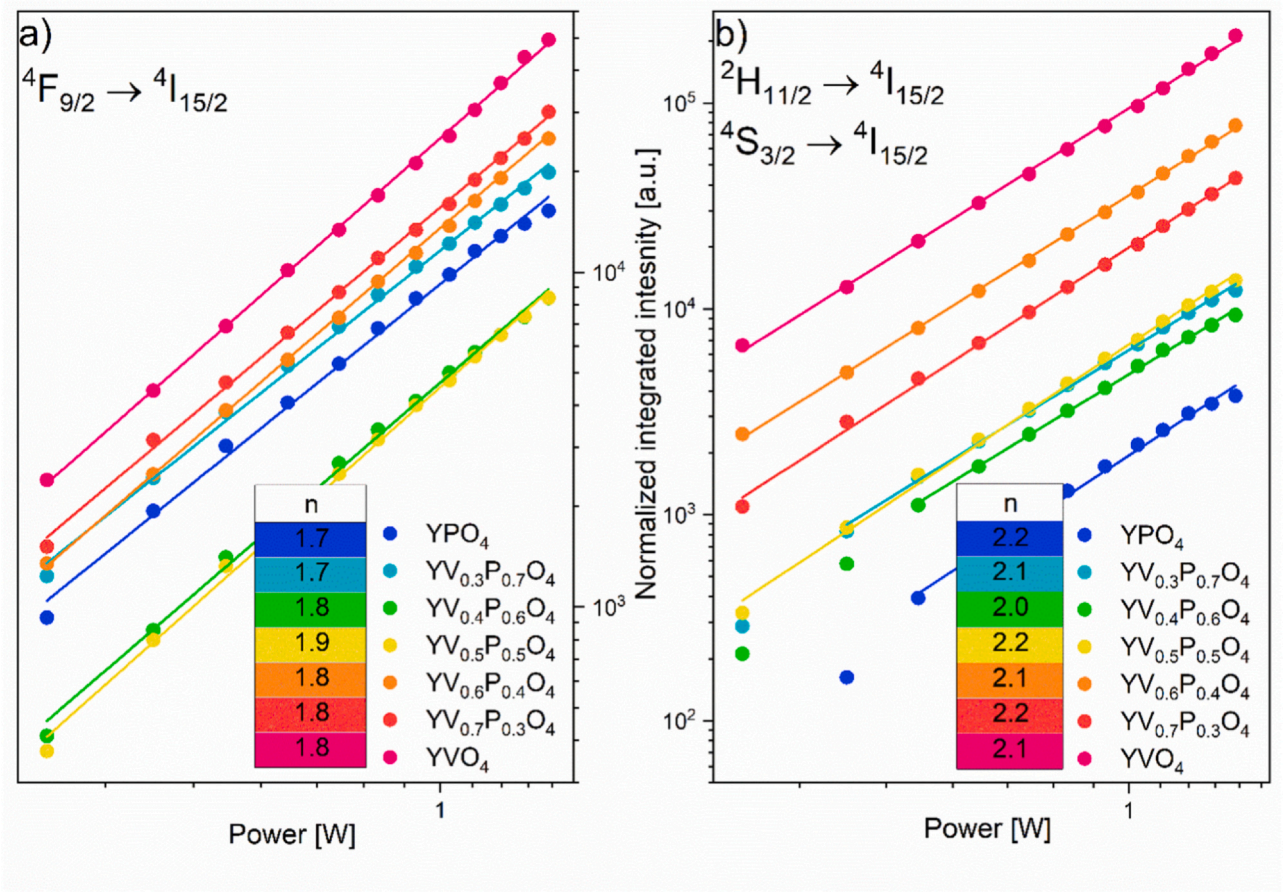

Fig. 9. Double logarithmic dependence of the emission intensity on the laser pump power of the $^4F_{9/2} \rightarrow {}^4I_{15/2}$ transition (a) and the $^2H_{11/2} \rightarrow {}^4I_{15/2}$, $^4S_{3/2} \rightarrow {}^4I_{15/2}$ transitions (b) in 1 mol% Er^{3+}, 20 mol% Yb^{3+}:$YV_xP_{1-x}O_4$ measured with FESH0850 filter at 300 K.

marked with pink, dashed, bended arrows, showing energy transfer from two separate Yb^{3+} sensitizer centers. Possible pathway for the $^1G_4$ level population is via cooperative sensitization process, which relies on direct and simultaneous energy transfer from two Yb^{3+} ions excited to the $^2F_{5/2}$ level. Therefore, population of the $^1G_4$ level can originate from subsequent absorption of two photons. Cooperative sensitization between Yb^{3+}-Yb^{3+} → Tm^{3+} has been proposed to be responsible for the population of the $^1G_4$ level [25,26,30].

Within materials co-doped with 1 mol% Er^{3+} and 20 mol% Yb^{3+} the process proceeding the ETU and ESA is Ground State Absorption (GSA), marked with black, solid arrow in the Fig. 12**.** Excited State Absorption (ESA) is marked with orange, dashed arrow and occurs within erbium ions causing excitation of the higher states (i.e., $^4F_{7/2}$) from the first excited state ($^4I_{11/2}$). In erbium-ytterbium co-doped materials, population of the Er^{3+} upper levels is more complex, than in case of Tm^{3+}, and involves: energy transfer up-conversion (black, dashed, bended arrows), excited state absorption (orange, dashed arrow) and cross-relaxation (yellow, dotted arrows). The preceding process for excited state absorption is ground state absorption (black, solid arrow), which leads to populating the $^4I_{15/2}$ level. Excitation to the upper $^4F_{7/2}$ level within Er^{3+} ion is caused by the absorption of subsequent photon. Further, the $^4F_{7/2}$ level is depopulated via non-radiative relaxation to the $^2H_{11/2}$ level, emission to the ground state may be observed at 523 nm or non-radiative relaxation of the $^2H_{11/2}$ level may lead to populating next lower lying the $^4S_{3/2}$ level. The $^4S_{3/2} \rightarrow {}^4I_{15/2}$ transition is associated with emission at 547 nm. The $^4F_{9/2}$ level is populated by the cross-relaxation processes (yellow, dashed arrows) between two erbium ions [31]. Cross-relaxation is a process of non-radiative energy transfer between two adjacent ions of the same element (herein Er^{3+}). One ion lowers its excitation energy by depopulating to a lower excited state, this energy is transferred to other ion leading to population of its higher states. In the scheme marked with yellow, dotted arrows. The cross-relaxation process causes quenching the luminescence of one kind of ions [32]. Energy transfer related to up-conversion in Er^{3+}-Yb^{3+} (black, dashed, bended arrows) pairs is involving a non-resonant energy transfer from excited sensitizer center (the $^2F_{5/2}$ level of Yb^{3+}) to the $^4I_{11/2}$ level in Er^{3+}. Second non-resonant energy transfer from the $^2F_{5/2}$ level (Yb^{3+}) is leading to population of the $^4F_{7/2}$ level in Er^{3+} and non-radiative relaxation to the $^2H_{11/2}$ level. Emission to the ground state ($^2H_{11/2} \rightarrow {}^4I_{15/2}$, 523 nm) or non-radiative relaxation may occur and lead to populating the lower lying $^4S_{3/2}$ level and further, radiatively relax to the ground state ($^4S_{3/2} \rightarrow {}^4I_{15/2}$, 547 nm).

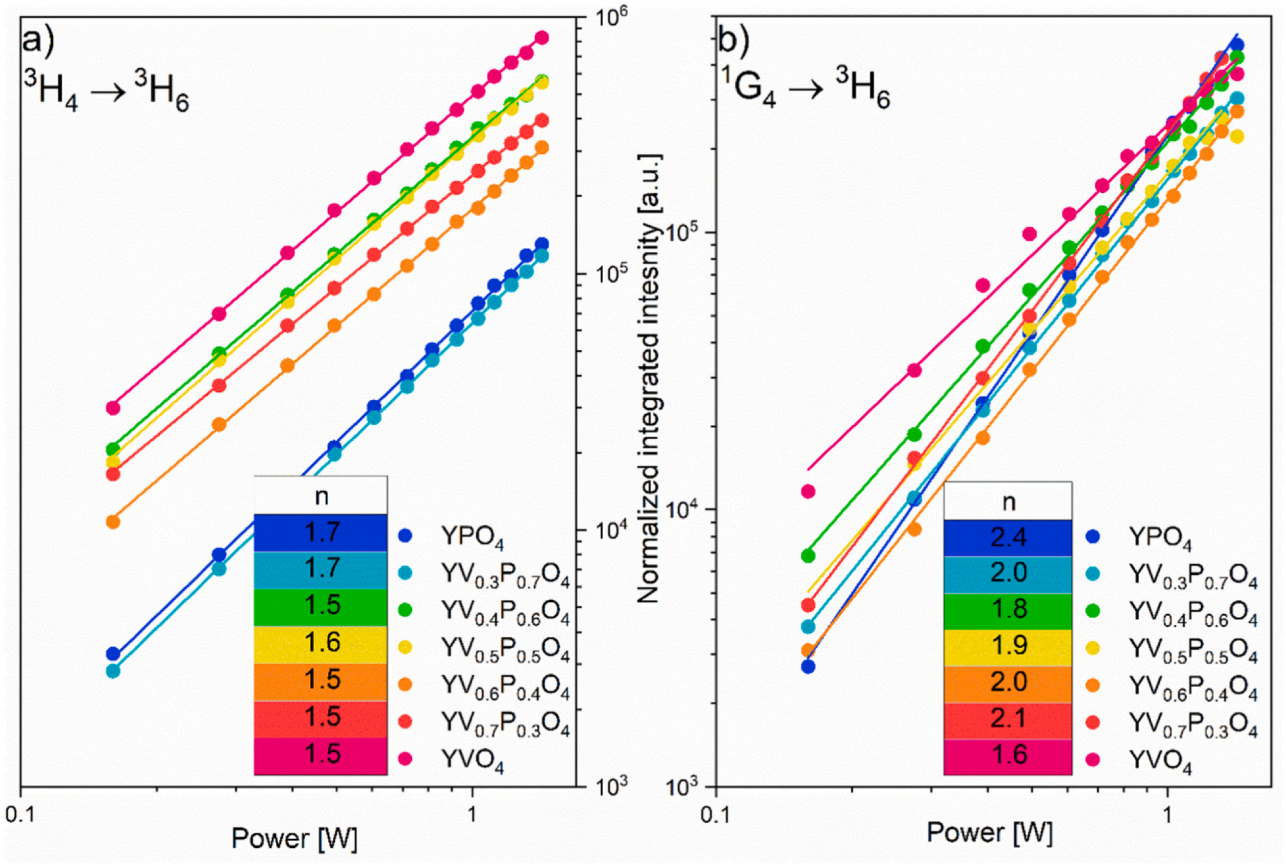

Fig. 10. Double logarithmic dependence of the emission intensity on the laser pump power of the $^3H_4 \rightarrow {}^3H_6$ transition (a) measured with Schott KG5 filter and of the $^1G_4 \rightarrow {}^3H_6$ transition (b) measured with filter FESH0850 in 0.25 mol% Tm^{3+}, 20 mol% Yb^{3+}:$YV_xP_{1-x}O_4$ (300 K).

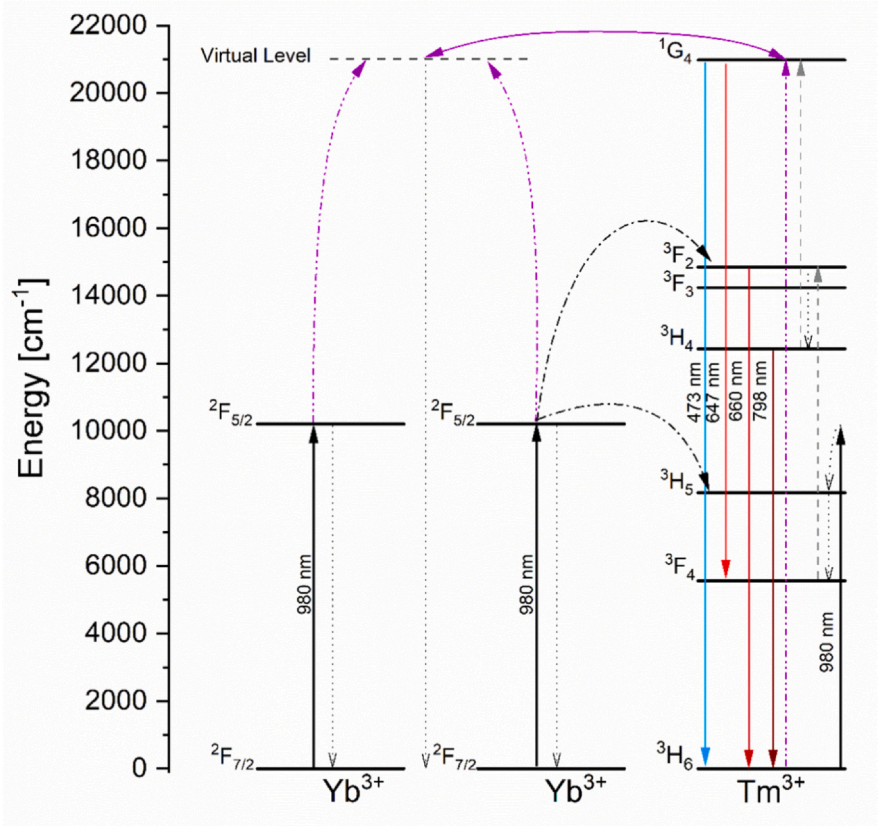

Fig. 11. Energy level scheme with proposed up-conversion processes occurring in 0.25 mol% Tm^{3+}, 20 mol% Yb^{3+}:$YV_xP_{1-x}O_4$.

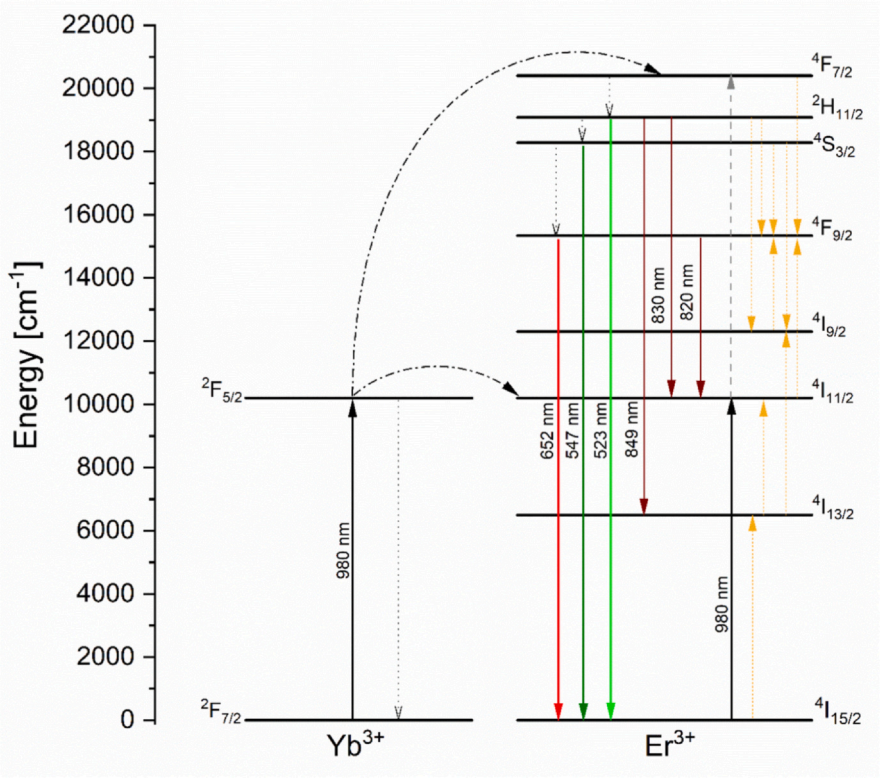

Fig. 12. Energy level scheme with proposed up-conversion processes occurring in 1 mol% Er^{3+}, 20 mol% Yb^{3+}:$YV_xP_{1-x}O_4$.

4. Conclusion

The thulium-ytterbium and erbium-ytterbium co-doped yttrium orthovanadate-phosphate system ($YV_xP_{1-x}O_4$, $0 \le x \le 1$) has been synthesized via co-precipitation method. Applied synthesis route leads to obtaining pure tetragonal nanocrystals. Analysis of yttrium orthovanadate-phosphate system's crystal phase purity, morphology as well as spectroscopic properties were studied extensively. The regularity in spectroscopic and structural properties of solid solutions ($YV_xP_{1-x}O_4$) associated with changing vanadium concentration has been described in detail. An influence of vanadium(V) concentration on up-conversion processes was characterized by performed measurements.

Declaration of Competing Interest

The authors declare that they have no known competing financial interests or personal relationships that could have appeared to influence the work reported in this paper.

Acknowledgment

The authors would like to thank E. Bukowska for performing XRD measurements, D. Szymański for SEM images and the National Science Centre in Poland (NCN - Narodowe Centrum Nauki) for the financial support within the Project „*Preparation and modulation of spectroscopic properties of YXZO4, where X and Z - P^{5+}, V^{5+}, As^{5+}, doped with 's^2-like' ions and co-doped with rare earth ions*" (No. UMO-2019/33/B/ST5/02247).

References

[1] M. Runowski, A. Shyichuk, A. Tymiński, T. Grzyb, V. Lavin, S. Lis, Multifunctional optical sensors for nanomanometry and nanothermometry: high-pressure and high-temperature upconversion luminescence of lanthanide-doped phosphates - LaPO4 /YPO4:Yb3+ – Tm3+, ACS Appl. Mater. Interface Appl. Mater. Interfaces 10 (2018) 17269–17279, https://doi.org/10.1021/acsami.8b02853

[2] M. Soharab, I. Bhaumik, R. Bhatt, A. Saxena, A.K. Karnal, Effect of Yb co-doping on the spectral properties of Er: YVO4 single crystal: a Judd Ofelt analysis, J. Lumin. 200 (2018) 280–286, https://doi.org/10.1016/j.jlumin.2018.03.050

[3] Y. Cheng, K. Sun, Green, blue, red, near-infrared up-conversion luminescence of Yb3+/Er3+/Tm3+ co-doped YVO4 nanoparticles, J. Nanopart. Res. 20 (2018) 168, https://doi.org/10.1007/s11051-018-4268-5

[4] Y. Cheng, K. Sun, Sol – gel synthesis and upconversion luminescent properties of Yb3+, Er3+, Eu3+ triply-doped in YVO4 phosphors, J. Fluoresc. 28 (2018) 285–291, https://doi.org/10.1007/s10895-017-2191-2

[5] J. Zhang, Y. Wang, Z. Xu, H. Zhang, P. Dong, L. Guo, F. Li, S. Xin, W. Zeng, Preparation and drug-delivery properties of hollow YVO4:Ln3+ and mesoporous YVO4:Ln3+@nSiO2@mSiO2 (Ln ¼ Eu, Yb, Er, and Ho), J. Mater. Chem. B 1 (2013) 330–338, https://doi.org/10.1039/c2tb00045h

[6] G. Dantelle, R. Calderon-Villajos, C. Zaldo, C. Cascales, T. Gacion, Nanoparticulate coatings with efficient up-conversion properties (doi:dx.doi.org/), ACS Appl. Mater. Interfaces 6 (2014) 22483–22489, https://doi.org/10.1021/am5065377

[7] Y. Zhang, Y. Li, P. Li, G. Hong, Y. Yu, Preparation and upconversion luminescence of YVO4: Er3+, Yb3+, Int. J. Miner. Metall. Mater. 17 (2010) 225–228, https://doi.org/10.1007/s12613-010-0218-7

[8] S.K. Omanwar, S.R. Jaiswal, N.S. Sawala, K.A. Koparkar, V.B. Bhatkar, Ultra-violet to visible quantum cutting in YPO4: Gd3+, Tb3+ phosphor via down conversion, Mater. Discov. 7 (2017) 15–20, https://doi.org/10.1016/j.md.2017.05.003

[9] A. Tang, P. Ding, N. Song, S. Tang, L. Shi, Y. Zhao, Silicate micro-spheres modified with YPO4: Pr3+ particles: possessing light diffusion and blue-light down-conversion properties, Mater. Lett. 161 (2015) 395–398, https://doi.org/10.1016/j.matlet.2015.08.152

[10] K.Y. Li, L.Y. Liu, R.Z. Wang, Z. Xiao, H. Yan, Broadband sensitization of down-conversion phosphor YPO4 by optimizing TiO2 substitution in host lattice co-doped with Pr3+-Yb3+ ion-couple, J. Appl. Phys. (2014) 115, https://doi.org/10.1063/1.4869659 123103.

[11] W.O. Milligan, D.F. Mullica, Structural investigations of YPO4, ScPO4, and LuPO4, Inorg. Chem. Acta 60 (1982) 39–43, https://doi.org/10.1016/S0020-1693(00)91148-4

[12] B.C. Chakoumakos, M.M. Abraham, L.A. Boatner, Crystal structure refinements of zircon-type MVO4 (M = Sc, Y, Ce, Pr, Nd, Tb, Ho, Er, Tm, Yb, Lu), J. Solid State Chem. 109 (1994) 197–202, https://doi.org/10.1006/jssc.1994.1091

[13] F. Auzel, Upconversion and anti-stokes processes with f and d ions in solids, Chem. Rev. 104 (2004) 139–173, https://doi.org/10.1021/cr020357g

[14] J.R. Rustad, Density functional calculations of the enthalpies of formation of rare-earth orthophosphates†, Am. Mineral. 97 (2012) 791–799, https://doi.org/10.2138/am.2012.3948

[15] G. Strada, M. Schwendimann, La struttura cristallina di alcuni fosfati ed arseniati di metalii trivalenti. II. Arseniato e fosfato di ittrio, Gazetta Chim. Ital. 64 (1934) 662–674.

[16] R.C. Ropp, B. Carroll, Yttrium phosphate-yttrium vanadate solid solutions and Vegard's law, Inorg. Chem. 14 (1975) 2199–2202, https://doi.org/10.1021/ic50151a034
[17] G. Pan, H. Song, Q. Dai, R. Qin, X. Bai, B. Dong, L. Fan, F. Wang, Microstructure and optical properties of Eu3+ activated YV 1-xPxO4 phosphors, J. Appl. Phys. (2018) 104, https://doi.org/10.1063/1.3003130
[18] V. Biju, N. Sugathan, V. Vrinda, S.L. Salini, Estimation of lattice strain in nanocrystalline silver from X-ray diffraction line broadening, J. Mater. Sci. 43 (2008) 1175–1179, https://doi.org/10.1007/s10853-007-2300-8
[19] J. Eckert, J. Holzer, C. Krill, W. Johnson, Reversible grain size changes in ball-milled nanocrystalline Fe–Cu alloys, J. Mater. Res. 7 (1992) 1980–1983, https://doi.org/10.1557/JMR.1992.1980
[20] A.A. Nazarov, A.E. Romanov, R.Z. Valiev, On the nature of high internal stresses in ultrafine grained materials, Nanostruct. Mater. 4 (1994) 93–101, https://doi.org/10.1016/0965-9773(94)90131-7
[21] W. Qin, J.A. Szpunar, Origin of lattice strain in nanocrystalline materials, Philos. Mag. Lett. 85 (2005) 649–656, https://doi.org/10.1080/09500830500474339
[22] H.D. Nguyen, S. il Mho, I.H. Yeo, Preparation and characterization of nanosized (Y,Bi)VO4:Eu3+ and Y(V,P)O4:Eu3+ red phosphors, J. Lumin. (2009) 1754–1758, https://doi.org/10.1016/j.jlumin.2009.04.054
[23] M. Pollnau, D.R. Gamelin, S.R. Lüthi, H.U. Güdel, M.P. Hehlen, Power dependence of upconversion luminescence in lanthanide and transition-metal-ion systems, Phys. Rev. B 61 (2000) 3337–3346, https://doi.org/10.1103/PhysRevB.61.3337
[24] X. Wang, Q. Zhu, J.G. Li, Z. Hu, G. Zhu, C. Wang, La2O2S:Tm/Yb as a novel phosphor for highly pure near-infrared upconversion luminescence, Scr. Mater. 149 (2018) 121–124, https://doi.org/10.1016/j.scriptamat.2018.02.031
[25] A.K. Soni, V.K. Rai, Intrinsic optical bistability and frequency upconversion in Tm3+-Yb3+ - codoped Y2WO6 phosphor, Dalt. Trans. 43 (2014) 13563–13570, https://doi.org/10.1039/c4dt01266f
[26] X. Pei, Y. Hou, S. Zhao, Z. Xu, F. Teng, Frequency upconversion of Tm3+ and Yb3+ codoped YLiF4 synthesized by hydrothermal method, Mater. Chem. Phys. 90 (2005) 270–274, https://doi.org/10.1016/j.matchemphys.2004.03.013
[27] X.B. Chen, W.M. Du, N. Sawanobori, G.Y. Zhang, Z.F. Song, Initial experimental comparative investigation of direct and indirect up-conversion sensitization of the 1G4 level of Tm, Yb co-doped material, Opt. Commun. 181 (2000) 171–181, https://doi.org/10.1016/S0030-4018(00)00636-2
[28] L. Shi, C. Li, Q. Shen, Z. Qiu, White upconversion emission in Er3+/Yb3+/Tm3+codoped LiTaO3 polycrystals, J. Alloys Compd. 591 (2014) 105–109, https://doi.org/10.1016/j.jallcom.2013.12.234
[29] G.Y. Chen, Y. Liu, Y.G. Zhang, G. Somesfalean, Z.G. Zhang, Q. Sun, F.P. Wang, Bright white upconversion luminescence in rare-earth-ion-doped Y2O3 nanocrystals, Appl. Phys. Lett. 91 (2007) 1–4, https://doi.org/10.1063/1.2787893
[30] L. Li, H. Lin, X. Zhao, Y. Wang, X. Zhou, C. Ma, X. Wei, Effect of Yb3+ concentration on upconversion luminescence in Yb3+, Tm3+ co-doped Lu2O3 nanophosphors, J. Alloys Compd. 586 (2014) 555–560, https://doi.org/10.1016/j.jallcom.2013.10.122
[31] W. Wei, Y. Zhang, R. Chen, J. Goggi, N. Ren, L. Huang, K.K. Bhakoo, H. Sun, T.T.Y. Tan, Cross relaxation induced pure red upconversion in activator-and sensitizer-rich lanthanide nanoparticles, Chem. Mater. 26 (2014) 5183–5186, https://doi.org/10.1021/cm5022382
[32] G.G. Demirkhanyan, R.B. Kostanyan, F.P. Safaryan, T.V. Sanamyan, Cross-relaxation processes from the 4S3/2 level of the Er 3+ ion in Lu3Als012, Plenum Publ. Corp. 48 (1988) 1987–1989.

P4: *Emission Enhancement and Energy Transfers in $YV_{0.5}P_{0.5}O_4$ Nanoparticles Codoped with Eu^{3+} and Bi^{3+} Ions*

Marta Wujczyk, Sara Targonska, Philippe Boutinaud, John M. Reeks, Adam Watras, Rafal J. Wiglusz

Inorganic Chemistry, 2022, 61, 31, 12237-12248
DOI: 10.1021/acs.inorgchem.2c01465
IF: 5.436

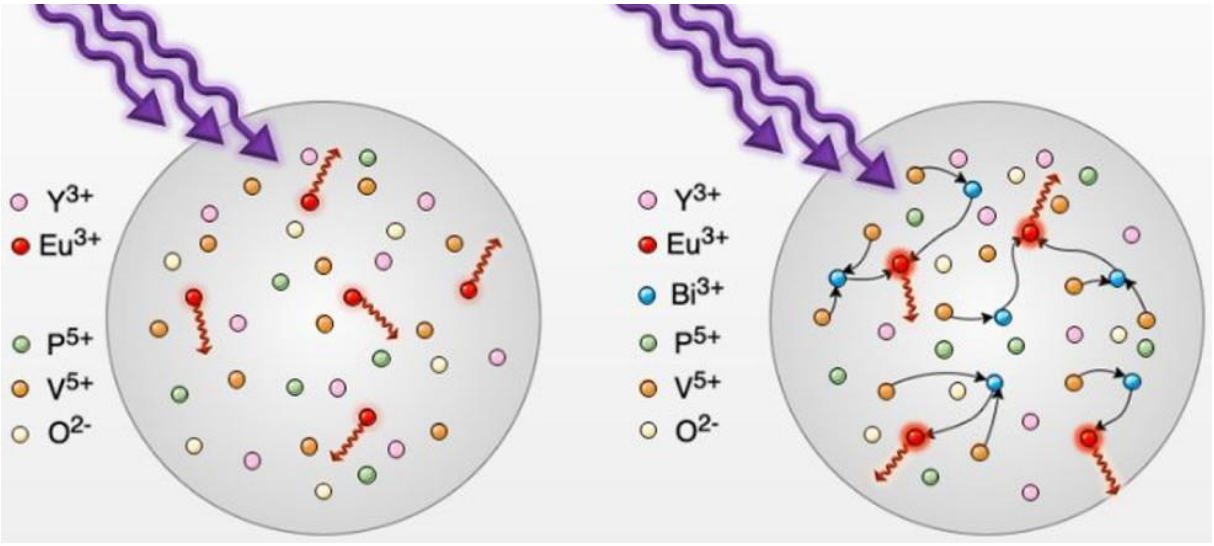

The motivation for the study entitled "*Emission Enhancement and Energy Transfers in $YV_{0.5}P_{0.5}O_4$ Nanoparticles Codoped with Eu^{3+} and Bi^{3+} ions*" was related the need to further investigate disordered solid solution system, and its influence on energy transfers occurring between RE^{3+} and s^2 ions.

The study aimed to analyse the impact of disordered structure on the luminescence and occurring energy transfers. The Eu^{3+} ions were used as the RE^{3+} ions, due to their ability to be applied as a luminescent probe. [102] The Bi^{3+} ions were used as the s^2 type ions. Bismuth ions are often used as an activator in YVO_4 systems causing an indirect enhancement of Eu^{3+} ions. [103]

The solid-state solutions of $YV_{0.5}P_{0.5}O_4$ were obtained through co-precipitation synthesis method. The crystal phase purity and elemental composition of the materials were determined using XRD and ICP-OES techniques. A narrowing of the XRD peaks was observed with increasing Bi^{3+} ions concentrations. In case of Eu^{3+} ions the FWHM (Full Width at Half Maximum) of the peaks remained constant, as no evident correlation was observed. Structural changes were also confirmed by infrared spectroscopy measurements. The TEM and SEM images revealed particle aggregates. It can be noted, that size of the particle increased with increasing Bi^{3+} content.

The main focus was put on the analysis of the luminescence properties in light of structure reordering for Bi^{3+} rich materials. Emission, excitation and luminescence decay time measurements were performed at room temperature. Emission spectra upon 395 nm excitation showed typical to Eu^{3+} ions emission , consisting of the $^5D_0 \rightarrow {}^7F_J$ ($J = 0, 1, 2, 3, 4$). Emission excitation spectra revealed three broad bands assigned to the O-Eu, the O-V, and the B-V charge transfers. Additionally, inner 4*f*-4*f* Eu^{3+} transition bands were observed. Performed was an emission spectra measurement for excitation in the aforementioned CT bands. Except of Eu^{3+} 4*f*-4*f* transition bands observed were broad band transitions. These bands were assigned to the Bi-V MMCT and perturbed vanadate groups emissions. Decay profiles were collected upon two excitations 397 nm and 355 nm, related to the $^7F_0 \rightarrow {}^5L_6$ and Bi-V MMCT respectively. Additionally, low temperature (5 K) emission and emission excitation spectra were measured. Obtained results vary from the room-temperature counterparts. In emission excitation spectra measured at 5 K, a red-shift of the Bi-V band is observed. Additionally, it is indicated that at 5 K Eu^{3+} ions emission is resulting from Bi-V sensitization pathway. Emission spectra, present changes in Stark components of the respective $^5D_0 \rightarrow {}^7F_J$ transitions. Hence,

presence of more than one Eu^{3+} site is assumed. The Bi^{3+} ions induced re-ordering of the structure directly affects changes of the ${}^5D_0 \rightarrow {}^7F_J$ transitions shapes.

In summary, the bismuth ions compensate P-V ionic size mismatch and re-ordering of the structure is observed for Bi^{3+} rich solid-state solutions. The presence of Eu^{3+} ions has no apparent effect on the structure of the solid solution. As expected, the presence of Bi^{3+} ions increased the emission intensity of Eu^{3+} ions. Upon non-direct excitation energy transfer occurs inefficiently, as it becomes apparent with presence of the Bi-V MMCT or vanadium groups broad emission bands.

The dissertation author contributed to the process of creating the scientific article with:

- Synthesis of the $YV_{0.5}P_{0.5}O_4$: Eu^{3+}, Bi^{3+} materials;
- Analysis of the XRD patterns;
- Analysis of the SEM and TEM images;
- Analysis of the ICP-OES elemental composition;
- Measurement and initial analysis of emission, emission excitation, and decay profiles;
- Preparation of the graphics and charts, excluding Figures 3, 7, and 12;
- Co-writing and co-editing the manuscript.

Inorganic Chemistry

pubs.acs.org/IC

Article

Emission Enhancement and Energy Transfers in $YV_{0.5}P_{0.5}O_4$ Nanoparticles Codoped with Eu^{3+} and Bi^{3+} Ions

Marta Wujczyk,* Sara Targonska, Philippe Boutinaud, John M. Reeks, Adam Watras, and Rafal J. Wiglusz*

Cite This: *Inorg. Chem.* 2022, 61, 12237−12248

Read Online

ACCESS | Metrics & More | Article Recommendations

ABSTRACT: In this study, solid-state solutions of yttrium orthovanadate-phosphate with varying concentrations of codopants (Eu^{3+}, Bi^{3+}) have been obtained via coprecipitation. An ionic radii mismatch between V^{5+} and P^{5+} substituents is manifested in broad XRD lines. The sharpening of the XRD lines is observed with increasing bismuth ions concentration in the Eu^{3+} codoped $YV_{0.5}P_{0.5}O_4$ matrix. The difference in the number of the Stark components for the $^5D_0 \rightarrow {}^7F_J$ transitions indicates changes in the lattice and a number of possible Eu^{3+} sites. A thorough, systematic spectroscopic analysis of $YV_{0.5}P_{0.5}O_4$: *x* mol % Eu^{3+}, *y* mol % Bi^{3+} was conducted at room temperature and 5 K. Metal-to-metal energy transfers occurring between Eu^{3+}, V^{5+}, and Bi^{3+} optically active ions have been investigated. Additionally, efficiency of the Bi^{3+}-Eu^{3+} energy transfer (ET) was calculated.

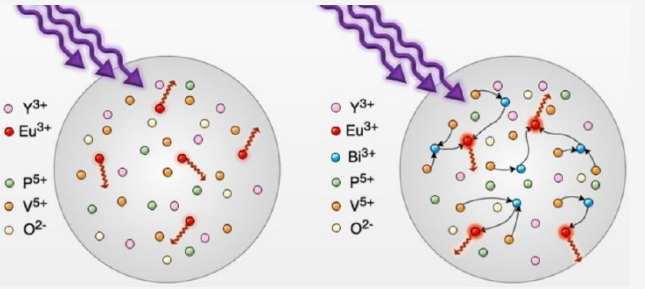

1. INTRODUCTION

The yttrium orthovanadate and yttrium orthophosphate matrices, doped with europium ions, are popular luminescent phosphors. This is due to their potential applications as laser host materials, polarizers, solar cells, light emitting diodes, host materials for optically active ions, etc.[1−7]

YVO_4 and YPO_4 crystallize in the zircon tetragonal system, within the space group $I4_1/amd$.[8,9] Hence, a solid-state solution of yttrium orthovanadate-phosphate can be formed.[10] Considering $YP_{0.5}V_{0.5}O_4$, its unit cell is composed of 50 mol % vanadium tetrahedral and 50 mol % phosphate tetrahedral groups, statistically substituted. Furthermore, in this work, yttrium ions in the lattice are statistically substituted with europium and bismuth ions.

In the present work, the fraction of the YPO_4−YVO_4−$BiVO_4$−$BiPO_4$ pseudoquaternary diagram (more precisely the shaded area of the $YP_{0.5}V_{0.5}O_4$−$BiVO_4$−$BiPO_4$ pseudo ternary subdiagram) is investigated (Figure 1). The bond valence sums (BVS) were obtained from VESTA,[11] and bond valence parameters were compiled in ref 12. The compounds in the shaded area have a disordered zircon-like crystal structure due to the inner structural characteristics of YPO_4 and YVO_4. Optically active europium ions are incorporated in $YP_{0.5}V_{0.5}O_4$ and $(Y,Bi)P_{0.5}V_{0.5}O_4$ for two purposes: to collect information on the local crystal structure and to investigate energy transfer processes involving Bi^{3+}. This paper constitutes an extension of previous reports[2,13−16] with more systematic, thorough spectroscopic analysis. Previous works[2,13,14] focus on parameters affecting the Eu^{3+} emission intensity in micron-sized[14] and nanosized[2,13] systems. It was previously established that codoping YVO_4:Eu^{3+} with P^{5+}, Bi^{3+}, and Gd^{3+} greatly enhances the europium ions' emission intensity. The compositions which maximize Eu^{3+} emission intensity are typically $Y_{0.9}Bi_{0.05}Eu_{0.05}$-$P_{0.5}V_{0.5}O_4$[13] or $Y_{0.45}Gd_{0.45}Bi_{0.05}Eu_{0.05}P_{0.5}V_{0.5}O_4$.[2] The reasons for this remain obscure.

Trivalent bismuth ion is known as an attractive activator in zircon vanadates.[15,17−23] Furthermore, it has been observed that Bi^{3+} is an efficient luminescence sensitizer for trivalent lanthanide ions.[3,24−28] In this study bismuth and europium ions are chosen as codopants, bismuth ions improve the photoluminescence intensity of Eu^{3+}. This phenomenon occurs as a result of UV excitation. This is due to the CT transitions from the Bi^{3+} 6s energy level to the 5d levels of the vanadate and subsequent energy transfer (ET) to Eu^{3+} ions 4f orbitals.[24,29−33]

This work emphasizes characterization of the luminescent properties of these two dopants incorporated into $YV_{0.5}P_{0.5}O_4$. This matrix has a disordered structure as a result of phosphate and vanadate units being randomly dispersed throughout the lattice. This occurs because the vanadate units are ∼8% larger

Received: April 28, 2022
Published: July 28, 2022

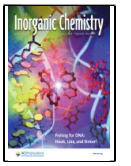

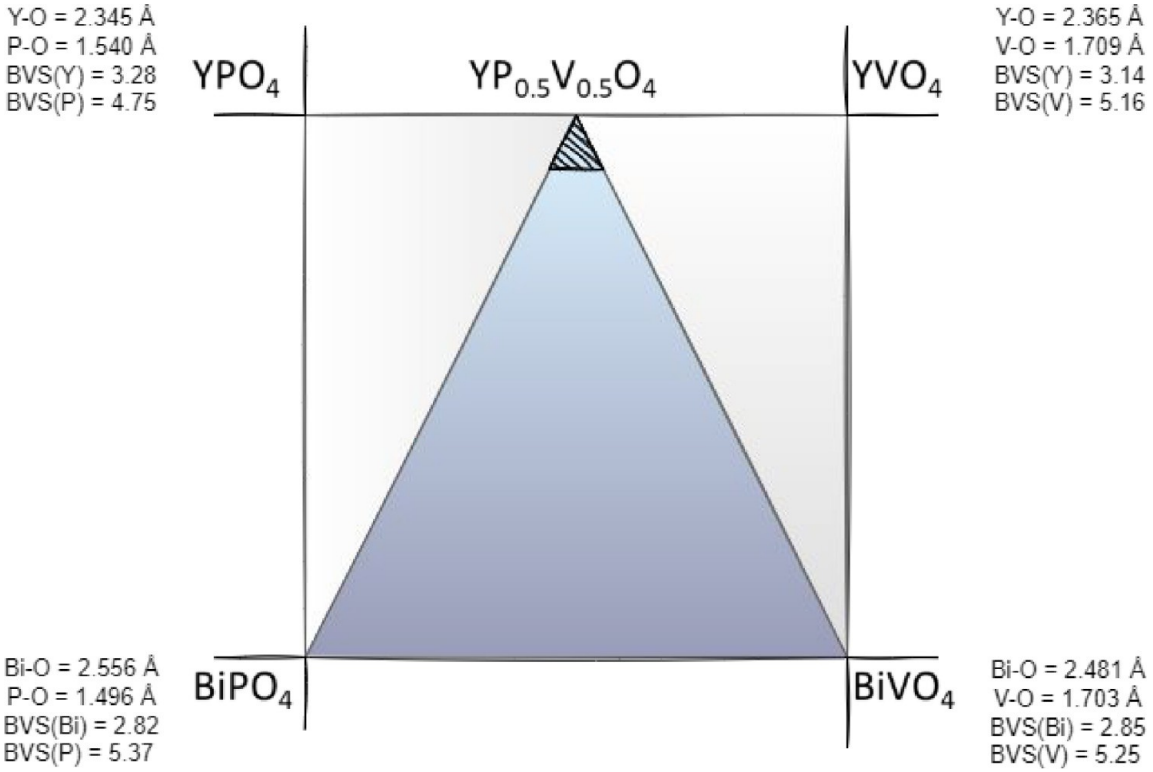

Figure 1. YPO_4–YVO_4–$BiVO_4$–$BiPO_4$ pseudoquaternary diagram. BVS = bond valence sum.

than the phosphates. The extent to which this disorder contributes to the efficiency of Bi^{3+}-Eu^{3+} ET will be investigated in this work. To this end, two series of materials were synthesized. The first one was doped with varying amounts of bismuth ions, while the second was doped with varying amounts of europium ions. The chemical compositions involved doping and codoping $YV_{0.5}P_{0.5}O_4$ with xBi^{3+}, yEu^{3+} where x = 0, 1, 3, 5, 10, 15 mol % and y = 0.5, 1, 2, 5 mol %. The solid state solutions were obtained by the wet chemistry synthesis-coprecipitation method with additional heat-treatment at 800 °C for 3 h.

2. EXPERIMENTAL METHODS

2.1. Materials Synthesis. Yttrium orthovanadate-phosphate powders, codoped with europium and bismuth ions, were obtained by the coprecipitation method. The concentrations of vanadium and phosphorus were fixed to 50 mol % each. Two series of materials were obtained: one in a function of bismuth concentration with fixed concentration of europium and vice versa. First, the concentration of europium ions was set to 1 mol %, while bismuth ion concentration changed from 0, 1, 3, 5, 10 up to 15 mol %. In the second series, the concentration of bismuth ions was set to 10 mol %, with concentrations of europium ion varying from 0.5, 1, 2, up to 5 mol %. Stoichiometric amounts of analytical grade Y_2O_3 (Alfa Aesar, 99.99%), Bi_2O_3 (Sigma-Aldrich, 99.9%), Eu_2O_3 (Alfa Aesar, 99.99%), $(NH_4)_2HPO_4$ (ACROS Organics, >98%) and NH_4VO_3 (Sigma-Aldrich, 99.5%) were used in this synthesis process.

The lanthanide and bismuth oxides were converted into nitrate salts through digestion with an excess of 65% HNO_3. Thereafter, the formed lanthanide and bismuth nitrates were recrystallized, and the HNO_3 excess was removed. Using deionized water as a solvent, separate aqueous solutions of diammonium phosphate and ammonium metavanadate were made. The vanadium and phosphorus ion sources (NH_4VO_3 and $(NH_4)_2HPO_4$) were mixed, followed by the nitrates ($Y(NO_3)_3$, $Bi(NO_3)_3$, $Eu(NO_3)_3$). The liquid mixture was stirred for 1.5 h at approximately 70 °C. Aqueous ammonia was used to maintain a pH of 9 during the reaction. The as-prepared precipitates were then washed and centrifuged at least three times, until neutral pH was reached. They were then dried for 24 h at 70 °C. The powders were finally crystallized by heat-treatment at 800 °C for 3 h in air.

2.2. ICP, XRD, SEM, and TEM Analyses. The crystal structure of synthesized materials was characterized by the X-ray Diffraction (XRD) technique using an X'Pert PRO X-ray diffractometer (Cu Kα1, 1.54060 Å) (PANalytical). Measured XRD patterns were compared to standards of YVO_4 (no. 78074) and YPO_4 (no. 79754) found in the Inorganic Crystal Structure Database (ICSD). Microstructural analyses (particle size, morphology) were performed by electron microscopy. SEM was carried out using an FEI Nova NanoSEM 230. High resolution transmission electron microscopy (HR-TEM) was performed using a Philips CM-20 Super Twin microscope. ICP-OES measurements were conducted on Thermo Scientific ICAP 7000 SERIES.

2.3. Spectroscopic Analysis. The Nicolet iS50 FT-IR from Thermo Scientific was used to collect infrared spectra at 300 K of samples processed in KBr pellets. The room-temperature emission spectra utilized excitation at 397, 340, and 300 nm. These spectra were collected using a FLS1000 photoluminescence spectrometer from Edinburgh Instruments. The same apparatus was used to collect the excitation spectra. The $^5D_0 \rightarrow {}^7F_2$ transition at 619 nm was monitored at room temperature for the excitation spectra measurements. Emission spectra were also recorded in response to the 266 nm excitation of a laser diode (CW) at room temperature and detected using the Hamamatsu PMA-12 photonic multichannel analyzer. The emission decay profiles were measured at 300 K using either a Ti:sapphire tunable laser or a Nd:YAG laser, a Hamamatsu R928 photomultiplier, a Jobin-Yvon THR 1000 spectrophotometer, and a digital LeCroy WaveSurfer oscilloscope. Excitation and emission spectra were collected at low temperature (5 K) using a temperature-controlled, continuous-flow liquid helium cryostat: Oxford Model CF 1204. Low temperature excitation spectra were measured with a Dongwoo Optron DM151i monochromator and a 150W ozone free lamp. The low temperature emission spectra were measured using a Dongwoo Optron DM750 monochromator, an Electro-Optical System INC PbS photodiode, or a Hamamatsu R928 photomultiplier.

https://doi.org/10.1021/acs.inorgchem.2c01465
Inorg. Chem. 2022, 61, 12237−12248

Table 1. Elemental Composition of the Europium and Bismuth Codoped $YV_{0.5}P_{0.5}O_4$ in Molar Percentages

	$YV_{0.5}P_{0.5}O_4$								
element	0.5% Eu^{3+} 10% Bi^{3+}	1% Eu^{3+} 10% Bi^{3+}	2% Eu^{3+} 10% Bi^{3+}	5% Eu^{3+} 10% Bi^{3+}	1% Eu^{3+} 1% Bi^{3+}	1% Eu^{3+} 3% Bi^{3+}	1% Eu^{3+} 5% Bi^{3+}	1% Eu^{3+} 10% Bi^{3+}	1% Eu^{3+} 15% Bi^{3+}
Y	89.08	98.73	87.83	84.97	97.95	95.47	92.42	88.91	83.66
V	49.70	49.63	50.05	49.65	50.32	50.55	49.79	49.78	50.06
P	49.79	49.54	49.89	50.27	50.54	48.73	49.84	49.47	49.74
Eu	0.52	1.01	1.95	4.98	1.03	1.03	1.03	1.02	1.05
Bi	10.06		10.01	10.10	0.96	3.03	4.97	9.98	14.94

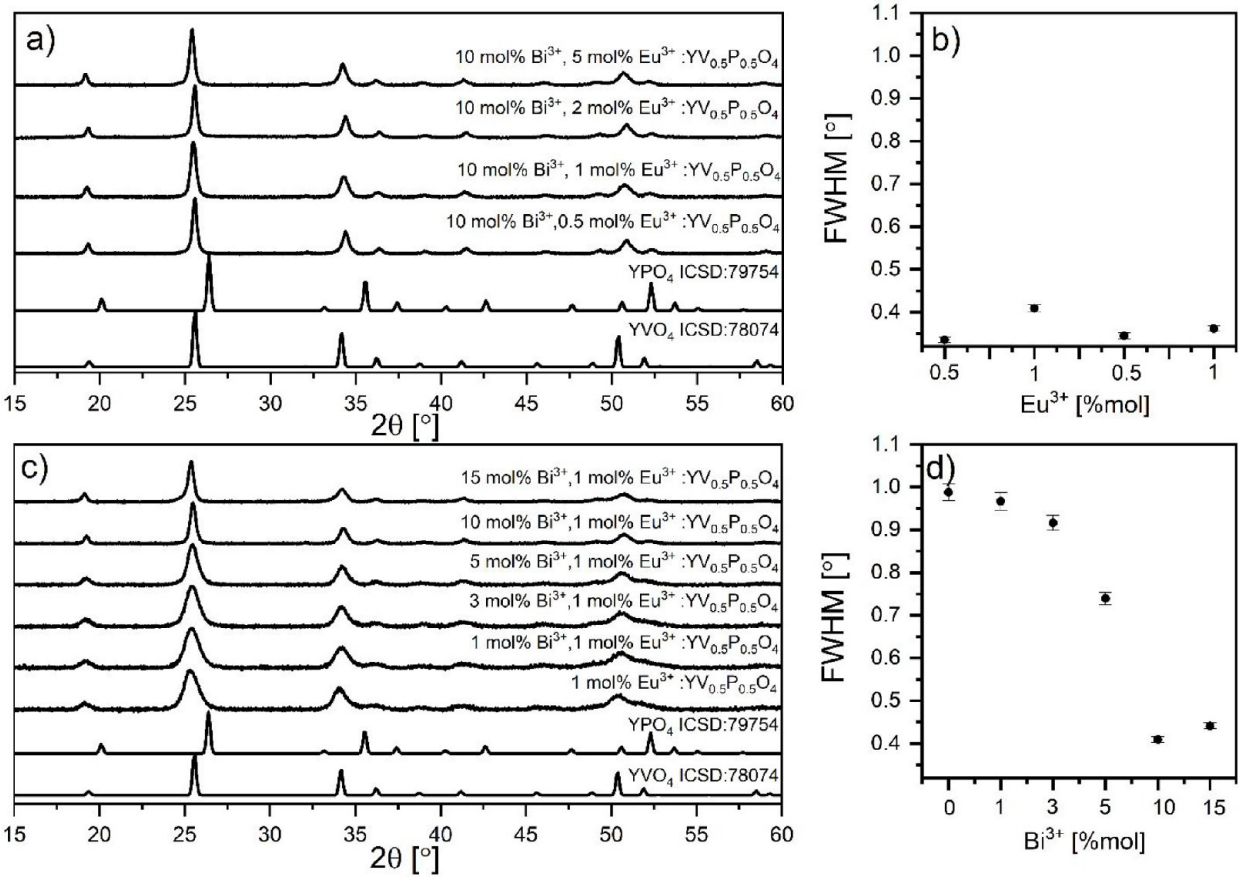

Figure 2. Diffractograms (a, c) and fwhm analysis (b, d) obtained for x mol % Bi^{3+}, 1 mol % Eu^{3+}: $YV_{0.5}P_{0.5}O_4$ and 10 mol % Bi^{3+}, y mol % Eu^{3+}: $YV_{0.5}P_{0.5}O_4$.

3. RESULTS AND DISCUSSION

3.1. Structure and Morphology. The chemical composition of all samples, analyzed by ICP-OES, is given in Table 1. It is verified that the nominal compositions are congruous with actual compositions.

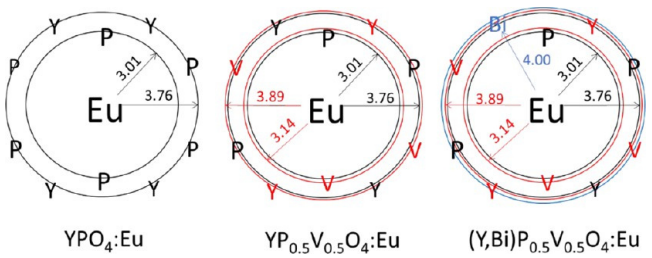

Figure 3. Cation coordination spheres of Eu^{3+} in zircon-like YPO_4, $YP_{0.5}V_{0.5}O_4$, and $(Y,Bi)P_{0.5}V_{0.5}O_4$. Oxygen atoms are not represented.

XRD results confirmed the crystal phase purity of $YV_{0.5}P_{0.5}O_4$ doped derivatives (Figure 2). The XRD peaks are broadened and further confirm the structural disorder, as observed earlier.[10,12,20] This broadening originates from the size difference between V^{5+} (0.36 Å, C.N. 4) and P^{5+} (0.17 Å, C.N. 4), when statistically distributed in $YV_xP_{1-x}O_4$ solid solution. The lattice strains are influenced by changes in grain size. This is a result of point defects, vacancies,[34] and varying composition[35] as well as dislocations near the grain-boundaries[36] caused by the incompatibility of phosphorus and vanadium atoms. The observed changes in the fwhm of the XRD peaks may indicate the presence of lattice strains.[37]

Co-doping with Eu^{3+} does not impact the lattice and, by extension, the width of the XRD peaks. In contrast, it is found that codoping with Bi^{3+} contributes to narrowing of the XRD peaks (Figure 2c). This is clearly evidenced by Figure 2b,d. Additionally, increasing the Eu^{3+} amount in 10 mol % Bi^{3+}

https://doi.org/10.1021/acs.inorgchem.2c01465
Inorg. Chem. 2022, 61, 12237−12248

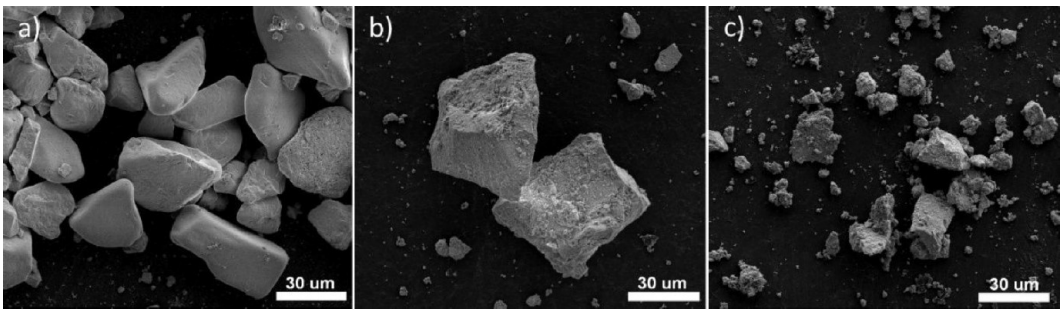

Figure 4. SEM images obtained for $YV_{0.5}P_{0.5}O_4$: 1 mol % Eu^{3+}, xBi^{3+}, where x = 5 mol % a), 10 mol % b), and 15 mol % c).

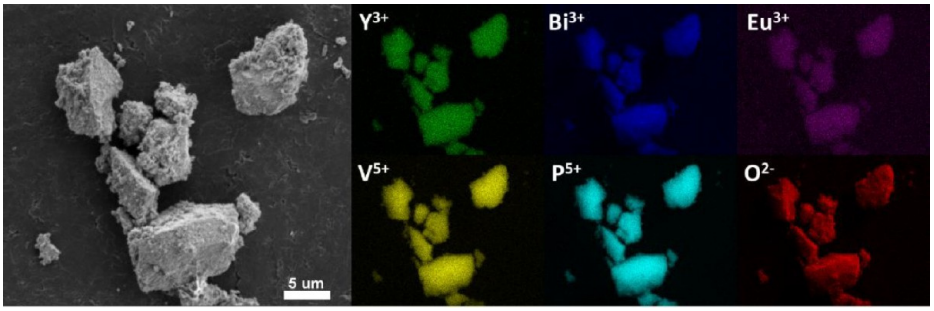

Figure 5. EDS maps obtained for 1 mol % Eu^{3+}, 10 mol % Bi^{3+}: $YV_{0.5}P_{0.5}O_4$.

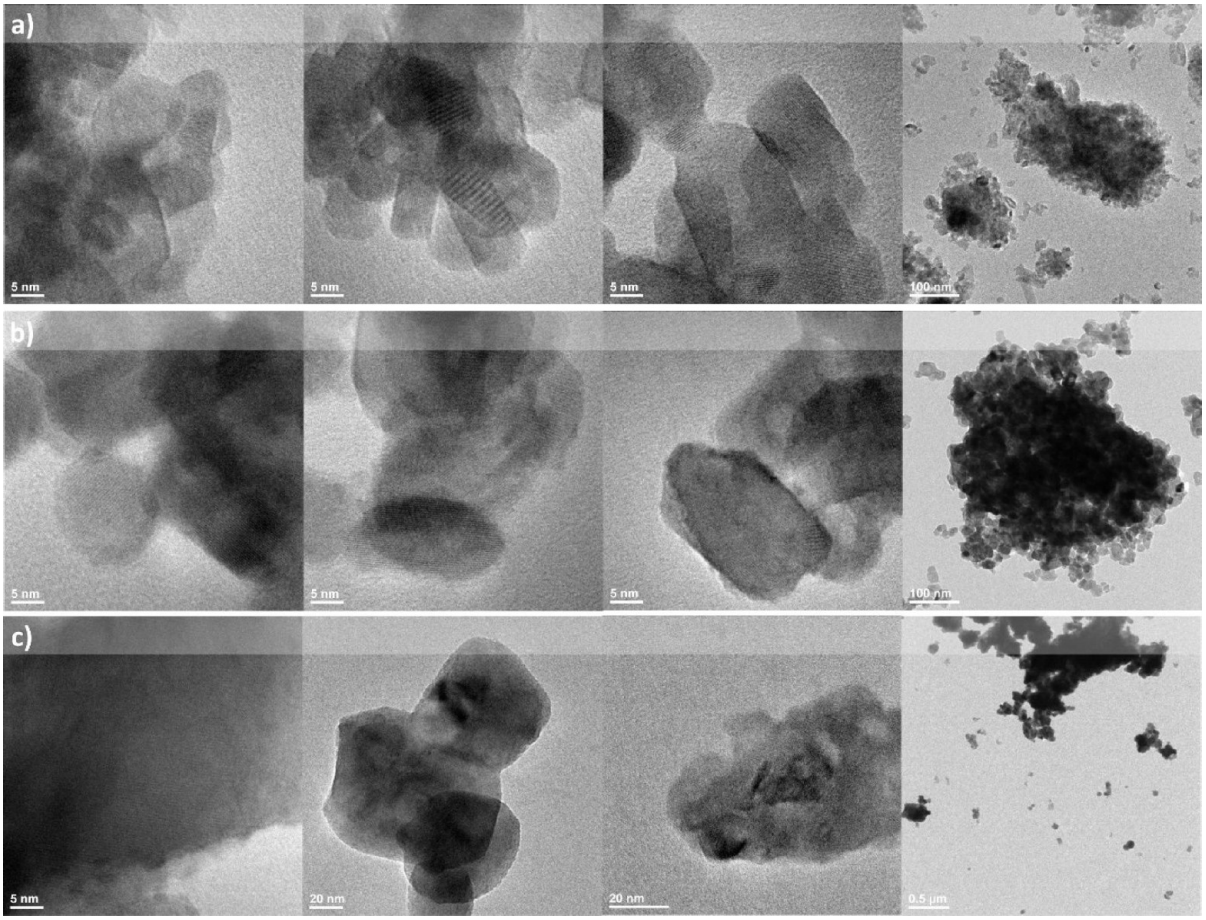

Figure 6. TEM images of $YV_{0.5}P_{0.5}O_4$ doped with 1 mol % Eu^{3+} and 1 mol % Bi^{3+} a), 1 mol % Eu^{3+} and 5 mol % Bi^{3+} b), and 1 mol % Eu^{3+} and 15 mol % Bi^{3+} (c).

codoped samples does not affect the XRD peak widths significantly.

By considering Eu^{3+} as a local luminescent structural probe, we find three possible environments experienced by Y^{3+} ions in

https://doi.org/10.1021/acs.inorgchem.2c01465
Inorg. Chem. 2022, 61, 12237−12248

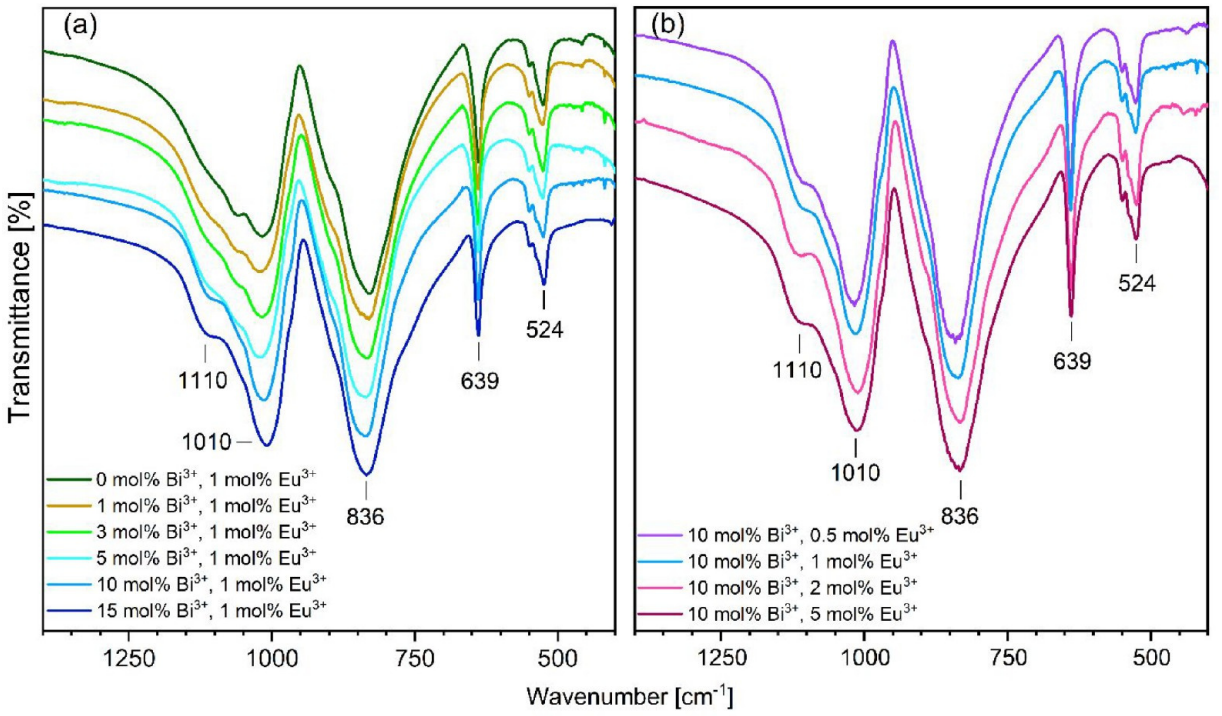

Figure 7. Fourier transformed infrared spectra of (a) codoped with Bi^{3+} and 1 mol % Eu^{3+} $YV_{0.5}P_{0.5}O_4$, with varying Bi^{3+} concentrations and (b) codoped with 10 mol % Bi^{3+} and Eu^{3+}, with varying Eu^{3+} concentrations.

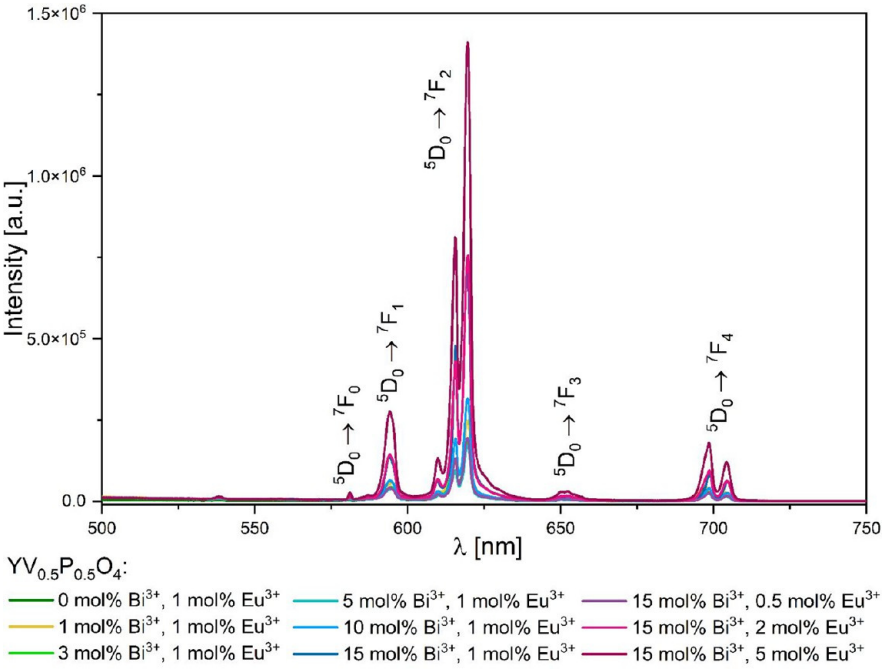

Figure 8. Emission spectra for x mol % Bi^{3+}, y mol % Eu^{3+}: $YV_{0.5}P_{0.5}O_4$ under 397 nm excitation at room temperature.

the compounds. This is depicted in Figure 3. In YPO_4, the Eu^{3+} ions are surrounded by eight O atoms, thus forming a dodecahedron with D_{2d} point symmetry. The first cation coordination consists of two P^{5+} at 3.01 Å and respectively four P^{5+} and four Y^{3+} at 3.76 Å in a second coordination. The exact charge (the BVS - Bond Valence Sum) carried by these cations is given in Figure 1. Incorporation of 50% V^{5+} creates two additional spheres at 3.14 and 3.89 Å (marked as red in Figure 3) with statistical occupancy. Incorporation of Bi^{3+} results in a third sphere (marked as blue in Figure 3) at 4.00 Å. The probability of finding a Bi^{3+} ion in this position is $P(x) = 1-(1-x)^4$ wherein x is the molar percentage of Bi^{3+}, e.g., $P(0.1) = 35\%$. The bismuth ions (1.17 Å at C.N. 8) substitute yttrium ions (1.02 Å at C.N. 8) in a statistical manner. Since Bi^{3+} is about 15% larger than Y^{3+}, its incorporation in the crystal lattice counterbalances (at least partly) the ionic radius mismatch between V^{5+} and P^{5+}. This inverse relationship between $V^{5+}-P^{5+}$ and $Bi^{3+}-Y^{3+}$ ionic radii mismatches reduces the lattice strains in $YV_{0.5}P_{0.5}O_4$ and thereby

https://doi.org/10.1021/acs.inorgchem.2c01465
Inorg. Chem. 2022, 61, 12237−12248

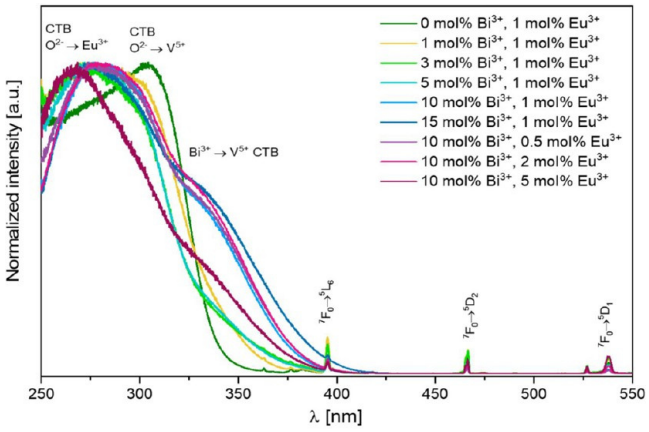

Figure 9. Excitation spectra for x mol % Bi^{3+}, y mol % Eu^{3+}: $YV_{0.5}P_{0.5}O_4$ materials measuring the intensity of the $^5D_0 \rightarrow {}^7F_2$ transition at 619 nm at room temperature.

sharpens the XRD lines as the Bi^{3+} concentration is raised (Figure 2c).

SEM images of $YV_{0.5}P_{0.5}O_4$: 1 mol % Eu^{3+}, x mol % Bi^{3+} materials are depicted in Figure 4. The powders look micrometric regardless of bismuth ion concentration. As the bismuth content is raised, the particles become smaller, and their surfaces become rougher. EDS maps (Figure 5) obtained for 1 mol % Eu^{3+}, 10 mol % Bi^{3+}: $YV_{0.5}P_{0.5}O_4$ confirm random distribution of the constituents.

The TEM images in Figure 6 demonstrate that the aggregates consist in fact of nanosized particles. Analysis of the SEM (Figure 5) and TEM (Figure 6) images reveals a wide distribution of particle sizes among the samples, although we note that the particles size increases as the Bi^{3+} content is raised (i.e., 19, 31, and 62 nm for doping rates of 1, 5, and 15 mol %, respectively). Differences in particles sizes contribute to the narrowing of the XRD peaks in addition to the reordering of the crystal structure. This work sheds a light into a complex structure of Eu^{3+}, Bi^{3+}: $YV_{0.5}P_{0.5}O_4$. However, to individuate or quantify the role of each effect, further crystallographic research needs to be conducted. Additionally, d-spacing values were calculated by the means of FFT processing in ImageJ software. d-Spacing was calculated to be d_{101} = 0.45 nm for $YV_{0.5}P_{0.5}O_4$ samples codoped with 1 mol % Eu^{3+} and 1 mol % Bi^{3+} and 1 mol % Eu^{3+} and 5 mol % Bi^{3+}, as well as 1 mol % Eu^{3+} and 15 mol % Bi^{3+}. Also d_{200} values were calculated. For samples codoped with 1 mol % Eu^{3+} and 1 mol % Bi^{3+}, d_{200} was 0.35 nm. However, 5 mol % and 15 mol % Bi^{3+}-doped samples had a d_{200} value of 0.33 nm. All d-spacing values coincide with d_{101} and d_{200} values from standard patterns of YVO_4 (d_{101} = 0.47132 nm, d_{200} = 0.35591 nm) and YPO_4 (d_{101} = 0.45379 nm, d_{200} = 0.34474 nm).

3.2. Spectroscopic Properties. The FT-IR spectra of $YV_{0.5}P_{0.5}O_4$ codoped with Eu^{3+} and Bi^{3+} are shown in Figure 7. There are five strong absorption bands in the range of 1300−400 cm^{-1}. The peaks at 524 cm^{-1} and at 639 cm^{-1} represent an antisymmetric bending vibration of $\nu_4(PO_4)^{3-}$. The antisymmetric stretching vibration of $\nu_3(PO_4)^{3-}$ can be found at 1010 cm^{-1} and at 1110 cm^{-1}.[38,39] The peak at 836 cm^{-1} is ascribed to the vibration mode of the $(VO_3)^-$ group. The weak peak detected at 502 cm^{-1} is related to the Y−O vibration.[40] This mode is not observed for the samples with more than 10 mol % of codopant ions concentration. The Bi−O modes are on the verge of our measurement range.[41,42]

Room temperature measurements revealed that all compounds exhibit red emission typical of Eu^{3+} upon direct *4f-4f* excitation at 397 nm (Figure 8). This emission increases in intensity with increasing Eu^{3+} and Bi^{3+} concentrations. The highest observed emission intensity is in samples containing 10 mol % Bi^{3+}, 5 mol % Eu^{3+}: $YV_{0.5}P_{0.5}O_4$.

The excitation spectra for x mol % Bi^{3+}, y mol % Eu^{3+}: $YV_{0.5}P_{0.5}O_4$ materials for the $^5D_0 \rightarrow {}^7F_2$ transition at 619 nm are shown in Figure 9. Three broad transitions are observed at 266, 300, and ≈340 nm (shoulder). They correspond to the $O^{2-} \rightarrow Eu^{3+}$, $O^{2-} \rightarrow V^{5+}$, and $Bi^{3+} \rightarrow V^{5+}$ charge transfers, respectively.[2,13,14,33] The intrinsic *4f-4f* excitation lines of Eu^{3+} (namely $^7F_0 \rightarrow {}^5L_6$, the $^7F_0 \rightarrow {}^5D_2$, and $^7F_0 \rightarrow {}^5D_1$ transitions) are comparatively much less intense.

Figure 10 depicts the emission spectra after excitation in the charge transfer bands. These intensities are normalized to the $^5D_0 \rightarrow {}^7F_1$ transition of Eu^{3+}. In addition to characteristic emission lines of Eu^{3+}, broad emission signals are observed. Upon 340 nm excitation, the broad signal represents the emission of the Bi−V metal-to-metal CT,[15] whereas upon 300 nm excitation, the broad signal is more surely due to perturbed vanadate groups. Upon 266 nm excitation, these bandlike emissions possibly overlap. The presence of these emission bands indicates an incomplete sensitization of Eu^{3+} luminescence. Two possible sensitization paths are identified. They involve the $(VO_4)^{3-}$ units or the Bi−V self-trapped excitons as energy donors and the Eu^{3+} ions as energy acceptors. Decay profiles were collected to quantify the efficiency of these energy transfers.

Decay profiles are presented in Figure 11 for 397 nm excitation (inner $^7F_0 \rightarrow {}^5L_6$ Eu^{3+} transition) or 355 nm excitation (Bi−V MMCT). Corresponding average values of the luminescence lifetimes t_{av}, were calculated as $t_{av} = \int I(t)t\,dt / (\int I(t)\,dt)$. In this case, $I(t)$ represents the emission intensity at time t. These values are provided in Table 2. A plot is proposed in Figure 12 for discussion.

The parameter η in Table 2 is related to the efficiency of the ET from Bi^{3+}-to-Eu^{3+} in the codoped compounds. It is obtained from the equation

$$\eta = 1 - \frac{\tau_{doped}}{\tau_{undoped}}$$

where τ_{doped} is the time constant in the presence of the Eu^{3+} acceptor, and $\tau_{undoped}$ is the time constant without Eu^{3+} (i.e., only Bi^{3+}).

Figure 12(a) pertains to the inner $^7F_0 \rightarrow {}^5L_6$ excitation of Eu^{3+}. The left-hand side of the vertical dashed line corresponds to 1 mol % Eu^{3+} doped samples with increasing Bi^{3+} concentrations (compound A to compound H, excluding compound B, in Table 2). Here, an increase in emission lifetime with increasing bismuth concentration is observed up to 3 mol % Bi^{3+} (compound D). These samples (A,C,D,E) also exhibit lower emission intensity relative to samples with higher Bi^{3+} concentrations. This suggests a lower radiative probability from the $^5D_0$ state in these cases. Raising the Bi^{3+} amount further contributes to enhance the Eu^{3+} emission intensity, and it correlates with a shortening of the lifetime. This effect has already been observed in YPO_4:Sm^{3+}, Bi^{3+} and is ascribed to an increased refractive index of the host lattice.[43] In this case, the radiative probability is increased, contributing to a lower emission lifetime. A synergetic effect with the reordering of the crystal structure is not excluded. This requires further

https://doi.org/10.1021/acs.inorgchem.2c01465
Inorg. Chem. 2022, 61, 12237−12248

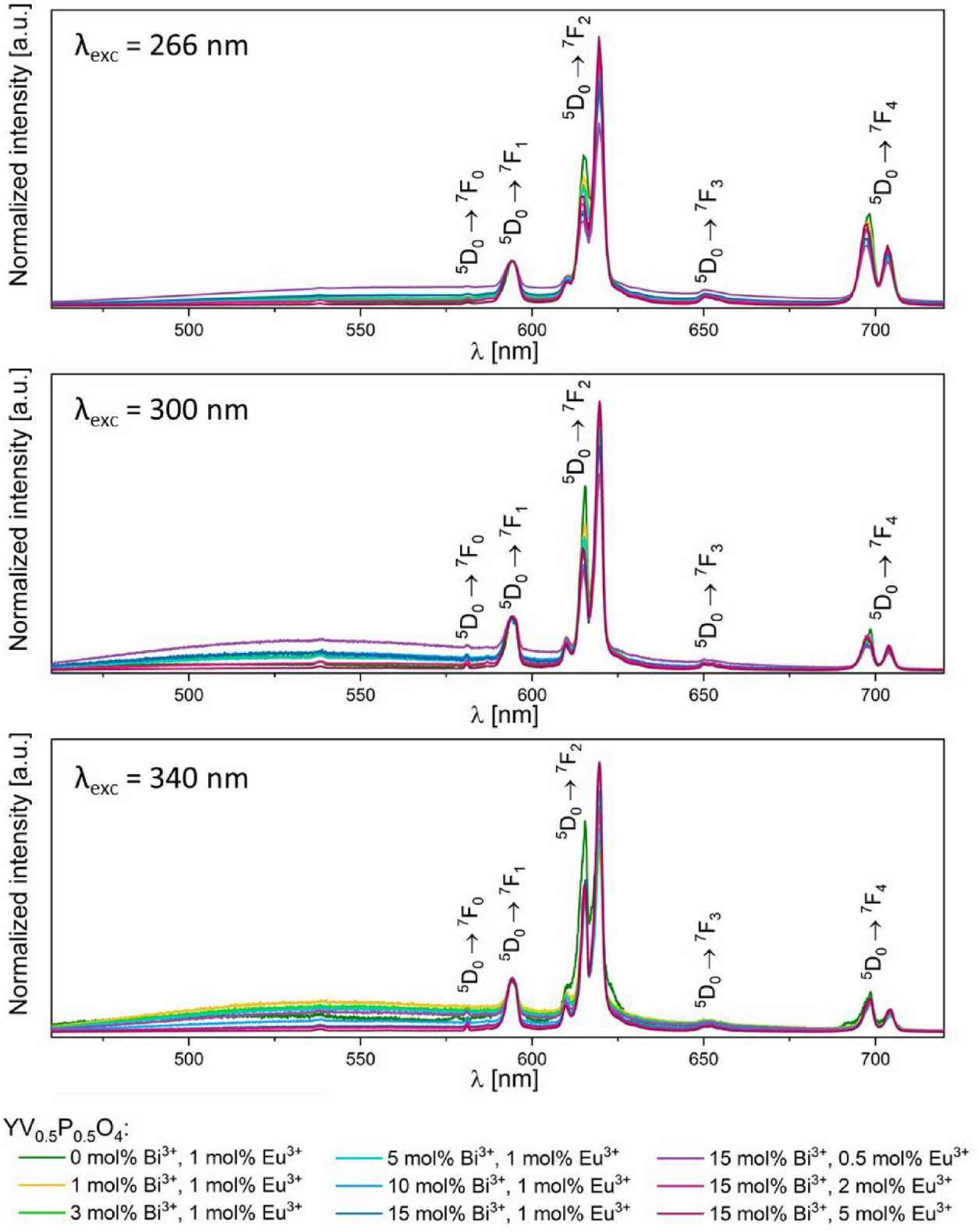

Figure 10. Emission spectra for *x* mol % Bi^{3+}, *y* mol % Eu^{3+}: $YV_{0.5}P_{0.5}O_4$ under 266, 300, and 340 nm excitation normalized to the $^5D_0 \rightarrow {}^7F_1$ transition of Eu^{3+}.

investigation. The right-hand side of the figure shows the effect of Eu^{3+} content for a fixed amount of Bi^{3+}. In this case, the emission lifetime does not vary significantly because the medium's refractive index is unchanged. Here, the increase in emission intensity is ascribed to the larger Eu^{3+} content that remains beyond the quenching concentration.[44,45]

Part (b) of Figure 12 relates to an excitation in the Bi−V MMCT band, the intensity of which exceeds by far that of the $^7F_0 \rightarrow {}^5L_6$ transition (Figure 9). In this situation, the Eu^{3+}

https://doi.org/10.1021/acs.inorgchem.2c01465
Inorg. Chem. 2022, 61, 12237−12248

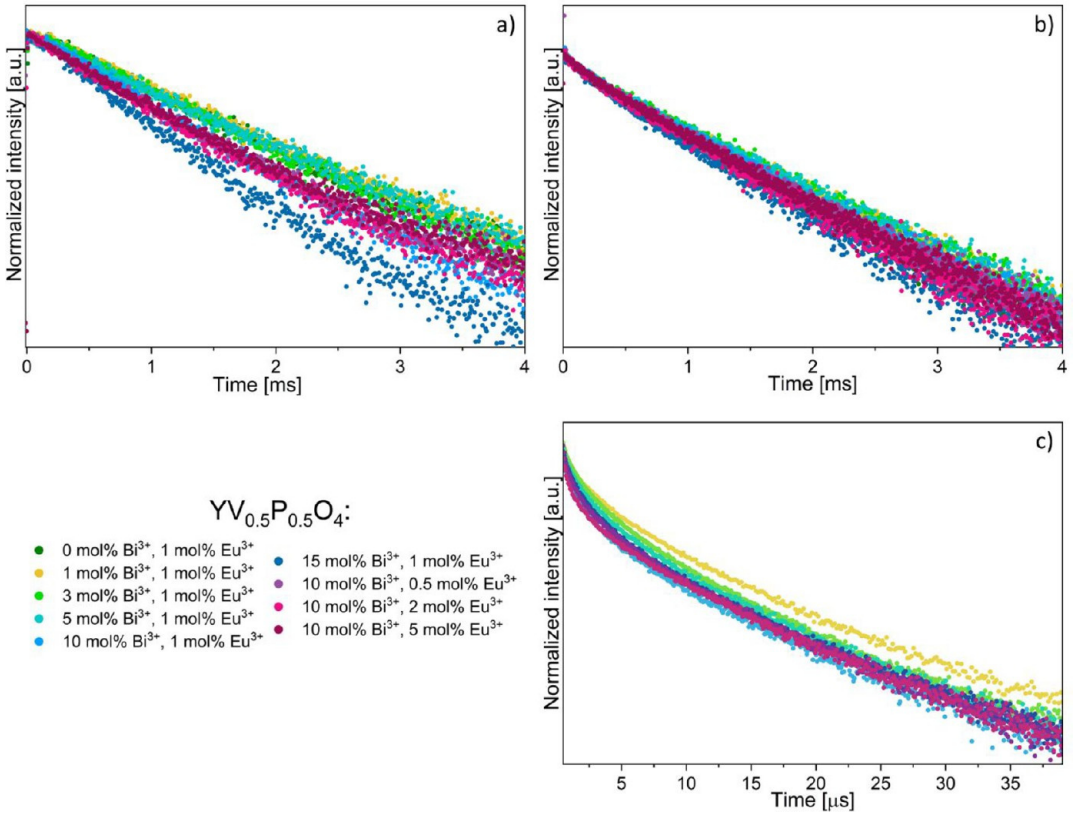

Figure 11. Decay time profiles measured for $^5D_0 \rightarrow {}^7F_2$ transition monitored at 619 nm λ_{exc} = 397 nm (a), $^5D_0 \rightarrow {}^7F_2$ transition, λ_{em} = 619 nm and λ_{exc} = 355 nm (b), and decay profiles measured for MMCT-Bi transition λ_{em} = 540 nm and λ_{exc} = 355 nm (c).

Table 2. Calculated Average Decay (t_{av}) and Rise (t_{rise}) Times for *x* mol % Bi^{3+}, *y* mol % Eu^{3+}: $YV_{0.5}P_{0.5}O_4$ Pumped with 397 and 355 nm Wavelengths[a]

		$^5D_0 \rightarrow {}^7F_2$ (Eu^{3+}) transition at 619 nm		Bi−V MMCT transition at 540 nm	
		λ_{exc} = 397 nm	λ_{exc} = 355 nm	λ_{exc} = 355 nm	
label	$YV_{0.5}P_{0.5}O_4$	t_{av} [ms]	t_{av} [ms]	t_{av} [μs]	η (%)
A	1 mol % Eu^{3+}	1.5	1.1		
B	1 mol % Bi^{3+}			7.0	
C	1 mol % Bi^{3+}, 1 mol % Eu^{3+}	1.6	1.2	6.9	1.1
D	3 mol % Bi^{3+}, 1 mol % Eu^{3+}	1.9	1.2	5.8	16.5
E	5 mol % Bi^{3+}, 1 mol % Eu^{3+}	1.6	1.2	5.8	17.2
F	10 mol % Bi^{3+}, 1 mol % Eu^{3+}	1.3	1.1	5.5	20.7
G	15 mol % Bi^{3+}, 1 mol % Eu^{3+}	1.1	0.9	5.6	19.5
H	10 mol % Bi^{3+}, 0.5 mol % Eu^{3+}	1.1	1.1	5.7	17.9
I	10 mol % Bi^{3+}, 2 mol % Eu^{3+}	1.0	1.0	5.9	16.2
J	10 mol % Bi^{3+}, 5 mol % Eu^{3+}	1.1	1.0	6.1	12.9

[a]Each sample composition was assigned a label to facilitate the discussion below.

emission is produced after an energy transfer whose efficacy is given in Table 2. Efficacy is 20% in the Bi^{3+}-rich compounds F and G but tends to fall off in compounds containing more than 1% Eu^{3+}: η is for instance comparable in compound D (3 mol % Bi^{3+}, 1 mol % Eu^{3+}) and in compound I (10 mol % Bi^{3+}, 2 mol % Eu^{3+}). Nevertheless, the emission intensity of compound J amounts to 6.5 times that of compound D, which demonstrates a synergy between Bi^{3+} and Eu^{3+} contents in $YV_{0.5}P_{0.5}O_4$. Furthermore, with respect to both 355 and 397 nm excitations, compound J exhibits the highest emission intensity related to direct Eu^{3+} excitation.

At sufficiently low temperatures, vibronic interactions can be frozen out. Thus, the luminescence spectra can give more detailed information regarding the electronic transitions of Eu^{3+} and can now be used as a structural probe. In 2008, Pan et. al[46] conducted investigations regarding the spectroscopic properties of Eu^{3+} in $Y(V,P)O_4$ solid solution by laser-selective excitation. This work identified three symmetry sites in the yttrium orthovanadate-phosphate mixed compounds due to disorder generated by the distribution of (PO_4) and (VO_4) tetrahedra. The Judd−Ofelt intensity parameters further confirmed that significant changes in ligand polarizability contribute to differences in local environments experienced by Eu^{3+}.[46]

Figure 13 illustrates the excitation spectra collected at 5 K corresponding to the 619 nm emission which represents the Eu^{3+} $^5D_0 \rightarrow {}^7F_2$ transition. Low temperature excitation spectra depict noticeable differences when compared to the room temperature spectra. These major differences are as follows:

(1) differences in relative intensity of the intrinsic $^7F_0 \rightarrow {}^5L_6$ transitions of Eu^{3+} to the CT excitation bands in compounds containing low amounts of Bi^{3+} (<5 mol %). This indicates a less efficient sensitization at 5 K. Furthermore, it demonstrates that in these conditions, the

https://doi.org/10.1021/acs.inorgchem.2c01465
Inorg. Chem. 2022, 61, 12237−12248

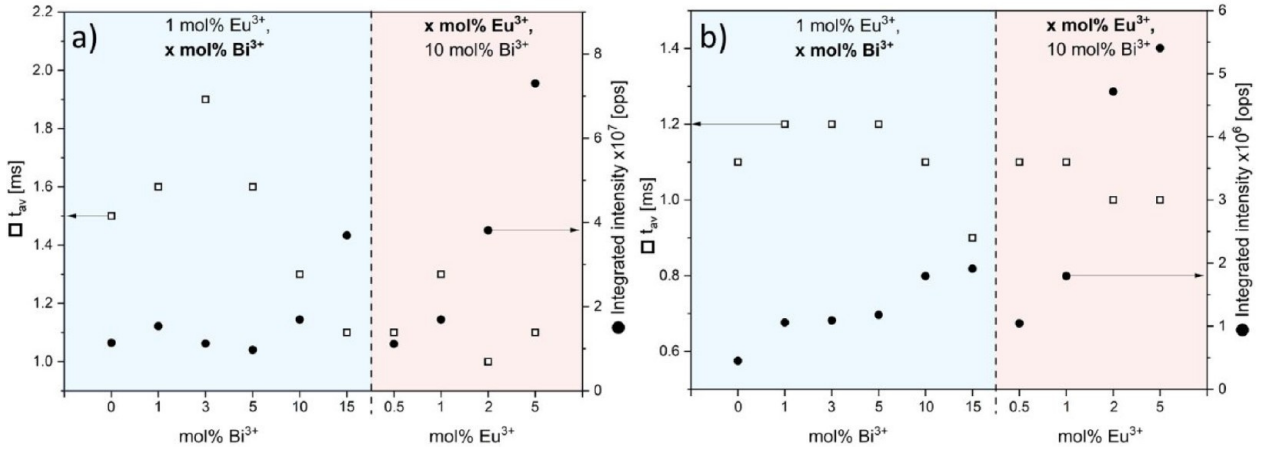

Figure 12. Integrated $^5D_0 \rightarrow {}^7F_2$ emission intensity (●) and average emission lifetime of Eu^{3+} (□) for the different compounds listed in Table 2 in correspondence with λ_{exc} = 397 nm (a) and λ_{exc} = 355 nm (b).

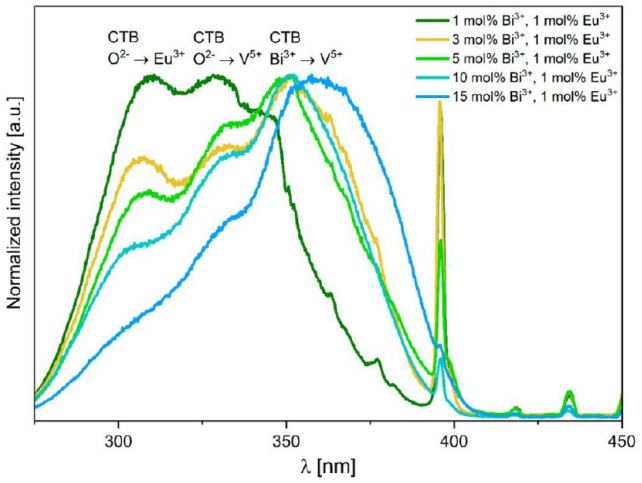

Figure 13. Excitation spectra for x mol % Bi^{3+}, 1 mol % Eu^{3+}: $YV_{0.5}P_{0.5}O_4$ materials monitoring the 619 nm emission corresponding to the $^5D_0 \rightarrow {}^7F_2$ transition at T = 5 K.

Table 3. Stark Components (in nm) of Eu^{3+} in YVO_4,[47] YPO_4,[47] and $Y_{1-x}Bi_xV_{0.5}P_{0.5}O_4$ (x = 0.01, and 0.10)[b]

$^5D_0 \rightarrow$	YPO_4	YVO_4	$Y_{0.98}Eu_{0.01}Bi_{0.01}V_{0.5}P_{0.5}O_4$	$Y_{0.89}Eu_{0.01}Bi_{0.10}V_{0.5}P_{0.5}O_4$
$^7F_0$	581.0	581.9		
$^7F_1$	592.7	593.5		
	596.1	595.0	594.7[a]	594.5[a]
$^7F_2$	613.4	615.5	610.5	609.9
	617.6	617.3	613.7	615.4
	619.3	619.4	615.3	618.8
	620.2	622.4	619.0	619.9
			619.9	
$^7F_4$	691.6	690.5	696.7	698.4
	694.4	696.7	698.6	704.0
	696.2	698.5	703.4	
	697.3	699.1		
	699.3	701.2		
	703.5	704.5		
	704.7	708.2		

[a]Centroid position. [b]Data were taken at 5 K.

Bi-to-Eu energy transfer is efficiently phonon assisted. However, even at 5 K the Bi-to-Eu energy transfer regains efficacy when the Bi^{3+} concentration is 10 mol %. This coincides with the increased presence of a broad excitation band which peaks at ≈360 nm and extends up to ≈400 nm, currently attributed to Bi−V MMCT.

(2) the presence of structures on the Bi−V MMCT excitation with maxima identified at ≈350, 330, and 307 nm. The relative intensity of these excitation maxima strongly depends on the Bi^{3+} content in the compound. There is a notable red shift in the excitation spectra as Bi^{3+} concentration increases. This shift of the Bi−V excitation edge with increasing the Bi content has been noted in previous studies, e.g., in ref32.

(3) the absence of excitation features pertaining to $O^{2-} \rightarrow Eu^{3+}$ and $O^{2-} \rightarrow V^{5+}$ charge transfers. This suggests these transitions are not involved in the sensitization process of Eu^{3+} at 5 K. Therefore, only the Bi−V MMCT operates as a sensitizing channel for Eu^{3+} at 5 K.

The emission spectra for 1, 3, 5, 10, 15 mol % Bi^{3+}, 1 mol % Eu^{3+}: $YV_{0.5}P_{0.5}O_4$ were collected at 5 K. These samples were excited in the CT bands and at 395 nm (Figure 14). The wavelengths of the Stark components observed in $Y_{0.98}Eu_{0.01}Bi_{0.01}V_{0.5}P_{0.5}O_4$ and $Y_{0.89}Eu_{0.01}Bi_{0.10}V_{0.5}P_{0.5}O_4$ are compiled in Table 3 and compared to reference data on Eu^{3+} in YPO_4 and YVO_4.[47]

Data related to the $^5D_0 \rightarrow {}^7F_4$ transition of Eu^{3+} are incomplete, when compared to the reference zircon compounds YPO_4:Eu^{3+} and YVO_4:Eu^{3+}. The $^5D_0 \rightarrow {}^7F_1$ transitions are also poorly resolved despite the low temperature. Thereby the results are discussed based on the $^5D_0 \rightarrow {}^7F_2$ transitions. Two different signatures are noted for the Eu^{3+} transitions in $Y_{0.98}Eu_{0.01}Bi_{0.01}V_{0.5}P_{0.5}O_4$ depending on the excitation wavelength. This indicates the presence of more than one Eu^{3+} type site in this crystal structure, which agrees with the conclusions of Pan et al.[46] In $Y_{0.89}Eu_{0.01}Bi_{0.10}V_{0.5}P_{0.5}O_4$, however, only four Stark components (instead of five) corresponding to the $^5D_0 \rightarrow {}^7F_2$ transition were observed. The spectrum in the $^5D_0 \rightarrow {}^7F_4$ region looks also simpler. This simplification of the spectral signatures is consistent with the progressive crystal structure reordering of $YP_{0.5}V_{0.5}O_4$ concomitant with an increase in Bi^{3+} concentration. This is previously observed in XRD results (Figure 2). Compared to YPO_4:Eu^{3+} and YVO_4:Eu^{3+}, the $^5D_0 \rightarrow {}^7F_2$ spectrum of $Y_{0.89}Eu_{0.01}Bi_{0.10}V_{0.5}P_{0.5}O_4$ is more split (265 cm^{-1}

https://doi.org/10.1021/acs.inorgchem.2c01465
Inorg. Chem. 2022, 61, 12237−12248

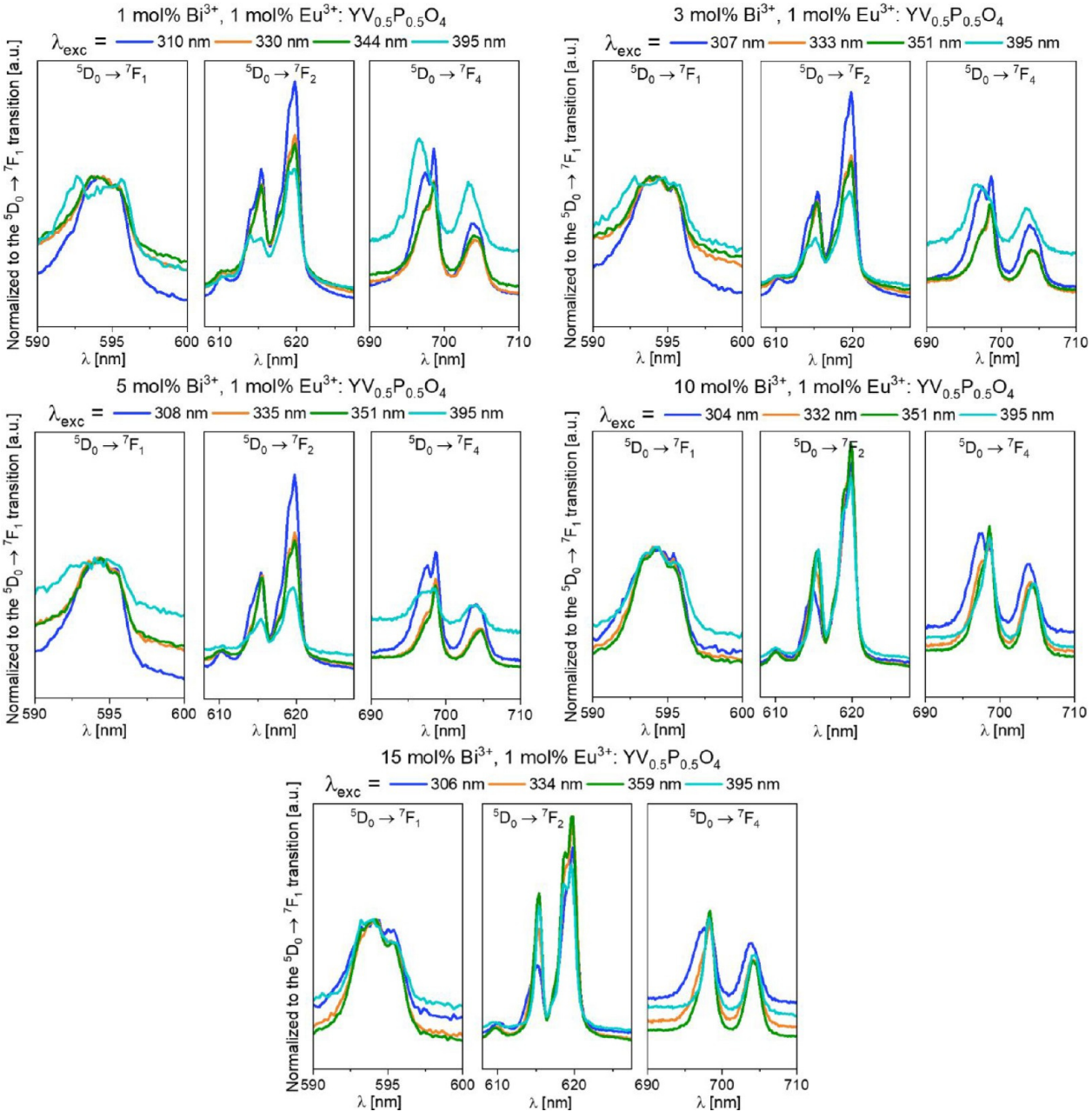

Figure 14. Emission spectra of 1 mol % Eu^{3+} in $Y_{1-x}Bi_xV_{0.5}P_{0.5}O_4$ (x = 0.01 to 0.15) upon various excitation wavelengths at 5 K. Spectra normalized to the $^5D_0 \rightarrow {}^7F_1$ transition of Eu^{3+}.

against 178−180 cm^{-1}), and its energy barycenter is upshifted. This is due to the presence of the Bi^{3+} ion in the second cationic neighborhood of Eu^{3+}, as we have depicted in Figure 3. Owing to the BVS values given in Figure 1, it is concluded that the formal charge carried by bismuth is below that of yttrium, with the consequence that the formal charge carried by phosphorus and vanadium atoms in the Bi-doped compounds is enhanced with respect to the Bi-free compounds. This, in turn, affects the formal charge carried by the oxygen atoms in the first coordination of Eu^{3+} by reinforcing the crystal field and softening the nephelauxetic effect.

4. CONCLUSION

The pure crystal phase of x mol % Bi^{3+}, y mol % Eu^{3+}: $YV_{0.5}P_{0.5}O_4$ was formed using a coprecipitation synthesis method. It is observed that codoping with Bi^{3+} is followed by narrowing of the XRD peaks, but codoping with Eu^{3+} does not significantly affect the widths of the peaks. The insufficient energy transfer to Eu^{3+}, resulting from the Bi−V MMCT and the $^3T_{1,2} \rightarrow {}^1A_1$ $(VO_4)^{3-}$ broad transition bands, is observed. Yet, Eu^{3+} ion emission is enhanced by increasing Bi^{3+} ion concentration. Further reaffirmed is the presence of more than one Eu^{3+} site due to $(PO_4)^{3-}$ and $(VO_4)^{3-}$ substitution. Additionally, an ordering of the crystal structure of $YP_{0.5}V_{0.5}O_4$ with increasing the Bi^{3+} content can be observed. It is supposed that at low temperature the sensitizing pathway of Eu^{3+} is less efficient in comparison to the room temperature, and mainly the Bi−V MMCT contribution is noticeable. Based on luminescent decay times, the Bi−Eu ET efficiency was found to be the highest for bismuth-rich compounds.

https://doi.org/10.1021/acs.inorgchem.2c01465
Inorg. Chem. 2022, 61, 12237−12248

AUTHOR INFORMATION

Corresponding Authors

Rafal J. Wiglusz − *Institute of Low Temperature and Structure Research, 50-422 Wroclaw, Poland*; orcid.org/0000-0001-8458-1532; Email: r.wiglusz@intibs.pl

Marta Wujczyk − *Institute of Low Temperature and Structure Research, 50-422 Wroclaw, Poland*; Phone: +48 (071) 3954159/274; Email: m.wujczyk@intibs.pl; Fax: +48 (071) 3441029

Authors

Sara Targonska − *Institute of Low Temperature and Structure Research, 50-422 Wroclaw, Poland*

Philippe Boutinaud − *Université Clermont Auvergne, Clermont Auvergne INP, CNRS, ICFC, F-63000 Clermont-Ferrand, France*

John M. Reeks − *Institute of Low Temperature and Structure Research, 50-422 Wroclaw, Poland*

Adam Watras − *Institute of Low Temperature and Structure Research, 50-422 Wroclaw, Poland*; orcid.org/0000-0003-4736-0356

Complete contact information is available at: https://pubs.acs.org/10.1021/acs.inorgchem.2c01465

Notes

The authors declare no competing financial interest.

ACKNOWLEDGMENTS

Regarding financial support, the authors acknowledge the National Science Centre Poland (NCN) within the project: 'Preparation and modulation of spectroscopic properties of $YXZO_4$, where X and Z − P^{5+}, V^{5+}, As^{5+}, doped with "s^2 -like" ions and codoped with rare-earth ions' (UMO-2019/33/B/ST5/02247). We express gratitude toward M. Sc. E. Bukowska for XRPD measurements and results, M. Sc. A. Hojenska for ICP measurements, PhD. D. Szymanski for measurements involving SEM-EDS, M. Sc. P. Wozniak for results and images from TEM measurements, and PhD. R. Lisiecki and PhD. B. Macalik for spectroscopic measurements at low temperature.

REFERENCES

(1) Huang, X. Y.; Wang, J. X.; Yu, D. C.; Ye, S.; Zhang, Q. Y.; Sun, X. W. Spectral conversion for solar cell efficiency enhancement using YVO_4:Bi^{3+}, Ln^{3+}(Ln Dy, Er, Ho, Eu, Sm, and Yb) phosphors. *J. Appl. Phys.* **2011**, *109*, 113526.

(2) Pu, Y.; Tang, K.; Zhu, D.-C.; Han, T.; Zhao, C.; Peng, L.-L. Synthesis and Luminescence Properties of (Y, Gd)(P, V)O_4:Eu^{3+}, Bi^{3+}Red Nano-phosphors with Enhanced Photoluminescence by Bi^{3+}, Gd^{3+} Doping. *Nano-Micro Lett.* **2013**, *5*, 117−123.

(3) Chen, L.; Chen, K. J.; Lin, C. C.; Chu, C. I.; Hu, S. F.; Lee, M. H.; Liu, R. S. Combinatorial approach to the development of a single mass YVO_4: Bi^{3+},Eu^{3+} Phosphor with red and green dual colors for high color rendering white light-emitting diodes. *J. Comb. Chem.* **2010**, *12*, 587−594.

(4) Wang, D.; Tie, S.; Wan, X. White light emitting from YVO_4/Y_2O_3:Eu^{3+}, Bi^{3+} composite phosphors for UV light-emitting diodes. *Ceram. Int.* **2015**, *41*, 7766−7772.

(5) Rambabu, U.; Do Han, S. Broad band down conversion from ultra violet light to near infrared emission in YVO_4:Bi^{3+}, Yb^{3+} as spectral conversion phosphor for c-Si solar cells. *Ceram. Int.* **2013**, *39*, 1603−1612.

(6) Khan, S. A.; Jalil, A.; Ullah Khan, Q.; Irfan, R. M.; Mehmood, I.; Khan, K.; Kiani, M.; Dong, B.; Khan, N. Z.; Yu, J. L.; Zhu, L.; Agathopoulos, S. New physical insight into crystal structure, luminescence and optical properties of YPO_4:Dy^{3+}\$Eu^{3+}$\$Tb^{3+}$ single-phase white-light-emitting phosphors. *J. Alloys Compd.* **2020**, *817*, 152687.

(7) Zheng, Y.; Li, F.; Wang, Y.; Zhang, K.; Peng, K. High-stability single-frequency green laser with a wedge Nd:YVO_4 as a polarizing beam splitter. *Opt. Commun.* **2010**, *283*, 309−312.

(8) Milligan, W. O.; Mullica, D. F. Structural Investigations of YPO_4, $ScPO_4$, and $LuPO_4$. *Inorganica Chem. Acta.* **1982**, *60*, 39−43.

(9) Chakoumakos, B. C.; Abraham, M. M.; Boatner, L. A. Crystal Structure Refinements of Zircon-Type MVO_4 (M = Sc, Y, Ce, Pr, Nd, Tb, Ho, Er, Tm, Yb, Lu). *J. Solid State Chem.* **1994**, *109*, 197−202.

(10) Wujczyk, M.; Watras, A.; Szyszka, K.; Wiglusz, R. J. Influence of vanadium concentration on up-conversion luminescence in Er^{3+}−Yb^{3+} and Tm^{3+}−Yb^{3+} ions pair co-doped $YV_xP_{1-x}O_4$ solid state solution. *J. Alloys Compd.* **2021**, *884*, 161022.

(11) Momma, K.; Izumi, F. An integrated three-dimensional visualization system VESTA using wxWidgets. *J. Appl. Crystallogr.* **2008**, *41*, 653−658.

(12) Brese, N. E.; O'Keeffe, M. Bond-valence parameters for solids. *Acta Crystallogr. Sect. B* **1991**, *47*, 192−197.

(13) Nguyen, H. D.; il Mho, S.; Yeo, I. H. Preparation and characterization of nanosized (Y,Bi)VO_4:Eu^{3+} and Y(V,P)O_4:Eu^{3+} red phosphors. *J. Lumin.* **2009**, *129*, 1754−1758.

(14) Sun, J.; Xian, J.; Xia, Z.; Du, H. Synthesis, structure and luminescence properties of Y(V,P)O_4:Eu^{3+},Bi^{3+} phosphors. *J. Lumin.* **2010**, *130*, 1818−1824.

(15) Cavalli, E.; Angiuli, F.; Mezzadri, F.; Trevisani, M.; Bettinelli, M.; Boutinaud, P.; Brik, M.G. Tunable luminescence of Bi^{3+}-doped $YP_XV_{1-X}O_4(0 \le X \le 1)$. *J. Phys.: Condens. Matter* **2014**, *26*, 385503.

(16) Boutinaud, P. Optical processes in (Y,Bi)VO_4 doped with Eu^{3+} or Pr^{3+}. *J. Phys.: Condens. Matter* **2014**, *26*, 405501.

(17) Blasse, G.; Bril, A. Investigations on Bi^{3+}-Activated Phosphors. *J. Chem. Phys.* **1968**, *48*, 217−222.

(18) Boulon, G. Processus de photoluminescence dans les oxydes et les orthovanadates de terres rares polycristallins activés par l'ion Bi^{3+}. *J. Phys. (Paris)* **1971**, *32*, 333−347.

(19) Moncorgé, R.; Boulon, G. Investigations of the absorption and emission properties along with energy transfer in pure and Bi^{3+} doped YVO_4. *J. Lumin.* **1979**, *18−19*, 376−380.

(20) Kang, F.; Peng, M.; Zhang, Q.; Qiu, J. Abnormal anti-quenching and controllable multi-transitions of Bi^{3+} luminescence by temperature in a yellow-emitting $LuVO_4$:Bi^{3+} phosphor for UV-converted white LEDs. *Chem. - A Eur. J.* **2014**, *20*, 11522−11530.

(21) Kang, F.; Sun, G.; Boutinaud, P.; Gao, F.; Wang, Z.; Lu, J.; Li, Y. Y.; Xiao, S. Tuning the Bi^{3+}-photoemission color over the entire visible region by manipulating secondary cations modulation in the $ScV_xP_{1-x}O_4$:Bi^{3+} $(0 \le x \le 1)$ solid solution. *J. Mater. Chem. C* **2019**, *7*, 9865−9877.

(22) Krasnikov, A.; Tsiumra, V.; Vasylechko, L.; Zazubovich, S.; Zhydachevskyy, Y. Photoluminescence origin in Bi^{3+} - doped YVO_4, $LuVO_4$, and $GdVO_4$ orthovanadates. *J. Lumin.* **2019**, *212*, 52−60.

(23) Krasnikov, A.; Mihokova, E.; Nikl, M.; Zazubovich, S.; Zhydachevskyy, Y. Luminescence spectroscopy and origin of luminescence centers in bi-doped materials. *Crystals.* **2020**, *10*, 208.

(24) Chen, D.; Yu, Y.; Huang, P.; Lin, H.; Shan, Z.; Zeng, L.; Yang, A.; Wang, Y. Color-tunable luminescence for Bi^{3+}/Ln^{3+}: YVO_4 (Ln = Eu, Sm, Dy, Ho) nanophosphors excitable by near-ultraviolet light. *Phys. Chem. Chem. Phys.* **2010**, *12*, 7775−7778.

(25) Huang, X. Y.; Wang, J. X.; Yu, D. C.; Ye, S.; Zhang, Q. Y.; Sun, X. W. Spectral conversion for solar cell efficiency enhancement using YVO_4:Bi^{3+},Ln^{3+} (Ln Dy, Er, Ho, Eu, Sm, and Yb) phosphors. *J. Appl. Phys.* **2011**, *109*, 113526.

(26) Liu, R.; Jin, Y.; Liu, L.; Liu, Y.; Tu, D. Molten salt synthesis and color manipulation of YVO_4:Bi^{3+},Eu^{3+} phosphors. *J. Alloys Compd.* **2020**, *826*, 154187.

(27) Natarajan, V.; Dhobale, A. R.; Lu, C. H. Preparation and characterization of tunable YVO_4: Bi^{3+}, Sm^{3+} phosphors. *J. Lumin.* **2009**, *129*, 290−293.

(28) Xue, J.; Wang, X.; Jeong, J. H.; Yan, X. Spectral and energy transfer in Bi^{3+}-Re^{N+} (n = 2, 3, 4) co-doped phosphors: Extended optical applications. *Phys. Chem. Chem. Phys.* **2018**, *20*, 11516−11541.
(29) Shao, J.; Yan, J.; Li, X.; Li, S.; Hu, T. Novel fluorescent label based on YVO_4: Bi^{3+}, Eu^{3+} for latent fingerprint detection. *Dye. Pigment.* **2019**, *160*, 555−562.
(30) Hara, H.; Takeshita, S.; Isobe, T.; Sawayama, T.; Niikura, S. A unique photofunction of YVO_4:Bi^{3+},Eu^{3+} nanophosphor: Photoluminescent indication for photochemical decomposition of polyurethane. *Mater. Sci. Eng. B Solid-State Mater. Adv. Technol.* **2013**, *178*, 311−315.
(31) Iso, Y.; Takeshita, S.; Isobe, T. Effects of YVO_4: Bi^{3+}, Eu^{3+} Nanophosphors Spectral Down-Shifter on Properties of Monocrystalline Silicon Photovoltaic Module. *J. Electrochem. Soc.* **2012**, *159*, J72−J76.
(32) Takeshita, S.; Isobe, T.; Sawayama, T.; Niikura, S. Effects of the homogeneous Bi^{3+} doping process on photoluminescence properties of YVO_4:Bi^{3+},Eu^{3+} nanophosphor. *J. Lumin.* **2009**, *129*, 1067−1072.
(33) Takeshita, S.; Isobe, T.; Sawayama, T.; Niikura, S. Low-temperature wet chemical precipitation of YVO_4:Bi^{3+},Eu^{3+} nanophosphors via citrate precursors. *Prog. Cryst. Growth Charact. Mater.* **2011**, *57*, 127−136.
(34) Qin, W.; Szpunar, J. A. Origin of lattice strain in nanocrystalline materials. *Philos. Mag. Lett.* **2005**, *85*, 649−656.
(35) Eckert, J.; Holzer, J.; Krill, C.; Johnson, W. Reversible grain size changes in ball-milled nanocrystalline Fe−Cu alloys. *J. Mater. Res.* **1992**, *7*, 1980−1983.
(36) Nazarov, A. A.; Romanov, A. E.; Valiev, R. Z. On the nature of high internal stresses in ultrafine grained materials. *Nanostructured Mater.* **1994**, *4*, 93−101.
(37) Biju, V.; Sugathan, N.; Vrinda, V.; Salini, S. L. Estimation of lattice strain in nanocrystalline silver from X-ray diffraction line broadening. *J. Mater. Sci.* **2008**, *43*, 1175−1179.
(38) Prasad, A. I.; Parchur, A. K.; Juluri, R. R.; Jadhav, N.; Pandey, B. N.; Ningthoujam, R. S.; Vatsa, R. K. Bi-functional properties of Fe_3O_4@YPO_4:Eu hybrid nanoparticles: Hyperthermia application. *Dalt. Trans.* **2013**, *42*, 4885−4896.
(39) Wu, J.; Jia, H.; Li, M.; Jia, H.; Liu, Z. Influence of pH on nanophosphor YPO_4:2%Sm^{3+} and luminescent properties. *Appl. Phys. A Mater. Sci. Process.* **2020**, *126*, 1−8.
(40) Wu, J.; Li, M.; Jia, H.; Liu, Z.; Jia, H.; Wang, Z. Morphology formation mechanism and fluorescence properties of nano-phosphor YPO_4:Sm^{3+} excited by near-ultraviolet light. *J. Alloys Compd.* **2020**, *821*, 153535.
(41) Chahine, A.; Et-Tabirou, M.; Pascal, J. L. FTIR and Raman spectra of the Na_2O-CuO-Bi_2O_3-P_2O_5 glasses. *Mater. Lett.* **2004**, *58*, 2776−2780.
(42) Boda, R.; Shareefuddin, M.; Chary, M. N.; Sayanna, R. FTIR and Optical Properties of Europium Doped Lithium Zinc Bismuth Borate Glasses. *Mater. Today Proc.* **2016**, *3*, 1914−1922.
(43) Angiuli, F.; Cavalli, E.; Boutinaud, P.; Mahiou, R. Emission properties of Sm^{3+}/Bi^{3+}-doped YPO_4 phosphors. *J. Lumin.* **2013**, *135*, 239−242.
(44) Yahiaoui, Z.; Hassairi, M. A.; Dammak, M. Synthesis and Optical Spectroscopy of YPO_4:Eu^{3+} Orange−Red Phosphors. *J. Electron. Mater.* **2017**, *46*, 4765−4773.
(45) Chang, Y. S.; Huang, F. M.; Tsai, Y. Y.; Teoh, L. G. Synthesis and photoluminescent properties of YVO_4:Eu^{3+} nano-crystal phosphor prepared by Pechini process. *J. Lumin.* **2009**, *129*, 1181−1185.
(46) Pan, G.; Song, H.; Dai, Q.; Qin, R.; Bai, X.; Dong, B.; Fan, L.; Wang, F. Microstructure and optical properties of Eu^{3+} activated $YV_{1-x}P_xO_4$ phosphors. *J. Appl. Phys.* **2008**, *104*, 084910.
(47) Linares, C.; Louat, A.; Blanchard, M. Rare-Earth - Oxygen Bonding in the $LnMO_4$ Xenotime Structure: Spectroscopic Investigation and Comparative Study of Ligand Field Models. In *New Concepts*; Struct. Bond.; 1977; pp 179−207,.

https://doi.org/10.1021/acs.inorgchem.2c01465
Inorg. Chem. 2022, 61, 12237−12248

Conclusions

The designed and applied experiments allowed for the desired objective to be achieved. Solid solutions of yttrium orthovanadate-arsenate, yttrium orthovanadate-phosphate, and yttrium orthovanadate were obtained. The materials were doped with rare earth ions: Eu^{3+}, Tb^{3+}, Er^{3+}, Tm^{3+}, Yb^{3+}, and s^2-type ions: Bi^{3+} ions. The impact of structural changes on the spectroscopic properties was noted and analysed. A customise set of measurements and conditions, was chosen to investigate the materials under study.

The use of different synthesis conditions, varying dopants concentrations, matrix composition, multiple excitation wavelengths, and many other variables allowed for the following conclusions to be drawn:

- The co-precipitation method produces phase-pure zircon-type $YXZO_4$ solid solutions. The structural changes become apparent with a shift of XRD planes.

- Mismatch in V^{5+} and P^{5+} ion size caused the broadening of XRD peaks, indicating an occurrence of defects and stress in the crystal structure.

- The introduction of a larger ion (Bi^{3+}) into the structure caused its re-ordering, which became apparent by the narrowing of the XRD peaks.

- The use of the co-precipitation method allowed the control of a broad range of pH conditions during the synthesis.

- The dependence of particle size and shape on the pH conditions of the synthesis was demonstrated. It was observed that with increasing pH a decrease in particle size occurs.

- The effect of structural changes on the luminescence properties of Eu^{3+}, Tb^{3+}, Er^{3+}-Yb^{3+}, and Tm^{3+}-Yb^{3+} ions was observed.

- The structural changes became apparent through a change in emission intensity, the shape of the transitions, and the contribution of individual transitions to total emission.

- The concentration threshold at which complete quenching of ion luminescence occurs is 65 mol% V^{5+}.

- The occurrence of Tb-As charge transfer in As^{5+} rich $YV_xAs_{1-x}O4$: 1 mol% Tb^{3+} materials was suggested.

- The low position of the Tb-V MMCT state is responsible for quenching the luminescence of Tb^{3+} ions.

- The up-conversion processes taking place in $YV_xP_{1-x}O_4$ solid-state solutions were determined as: ETU, ESA, cooperative sensitization, and cross-relaxation mechanisms.

- Enhancement of the Eu^{3+} emission was attained by (VO_4) groups and Bi^{3+}-V^{5+} MMCT state, the latter especially at low temperatures.

- Based of low-temperature measurements, it was suggested that the shape of the 4*f*-4*f* bands of the europium ion is simplified with increasing bismuth ion concentration. This relationship agrees with the re-ordering of the structure visible in powder diffractograms.

Scientific achievements

List of scientific papers

1. Adam Watras, **Marta Wujczyk**, Michael Roecken, Katarzyna Kucharczyk, Krzysztof Marycz, Rafal J. Wiglusz, *Investigation of pyrophosphates KYP_2O_7 co-doped with lanthanide ion useful in theranostics*, Nanomaterials, 2019, 9, 1597, 10.3390/nano9111597.
2. **Marta Wujczyk**, Adam Watras, Rafal J. Wiglusz, *The study of the influence of pH on the structural and spectroscopic properties of nanocrystalline Eu^{3+} ion-doped yttrium orthovanadate*, Dalton Transactions, 2021, 50, 3724-3733, 0.1039/D0DT04052E. **(P1)**
3. **Marta Wujczyk**, Adam Watras, Philippe Boutinaud, Marco Bettinelli, Sara Targonska, Jorma Hölsä, Rafal J. Wiglusz, *Emission Quenching and First Evidence of Tb^{3+}-to-As^{5+} Charge Transfer in Terbium(III) Ion-Doped $YV_xAs_{1-x}O_4$ Solid-State Solution*, Journal of Physical Chemistry C, 2020, 124, 17364-17371, 10.1021/acs.jpcc.0c04668. **(P2)**
4. Zbigniew Rybak, Maciej Janeczek, Maciej Dobrzynski, **Marta Wujczyk**, Albert Czerski, Piotr Kuropka, Agnieszka Noszczyk-Nowak, Maria Szymonowicz, Aleksandra Sender-Janeczek, Katarzyna Wiglusz, Rafal J. Wiglusz, *Study of Flebogrif®—A New Tool for Mechanical Sclerotherapy—Effectiveness Assessment Based on Animal Model*, Nanomaterials, 2021, 11, 544, 10.3390/nano11020544.
5. Aleksandra Kuzan, **Marta Wujczyk**, Rafal J. Wiglusz, *The Study of the Aorta Metallomics in the Context of Atherosclerosis*, Biomolecules, 2021, 11, 946, 10.3390/biom11070946.
6. **Marta Wujczyk**, Adam Watras, Katarzyna Szyszka and Rafal J. Wiglusz, *Influence of Vanadium Concentration on Up-conversion Luminescence in Er^{3+}-Yb^{3+} and Tm^{3+}-Yb^{3+} Ions Pair Co-Doped $YV_xP_{1-x}O_4$ Solid State Solution*, Journal of Alloys and Compounds, 2021, 884, 161022, 10.1016/j.jallcom.2021.161022. **(P3)**
7. Katarzyna Herman, **Marta Wujczyk**, Maciej Dobrzynski, Dorota Diakowska, Katarzyna Wiglusz and Rafal J. Wiglusz, *In vitro assessment of long-term fluoride ion release from nanofluorapatite*, Materials, 2021, 14, 3747, 10.3390/ma14133747.

8. Sara Targonska, Monika Dobrzynska-Mizera, **Marta Wujczyk**, Justyna Rewak-Soroczynska, Monika Knitter, Katarzyna Dopierala, Jacek Andrzejewski, Rafal J. Wiglusz, *New way to obtain the poly(L-lactide-co-D,L-lactide) blend filled with nanohydroxyapatite as biomaterial for 3D printed bone-reconstruction implants*, European Polymer Journal, 2022, 165, 110997, 10.1016/j.eurpolymj.2022.110997.
9. **Marta Wujczyk**, Sara Targonska, Philippe Boutinaud, John M. Reeks, Adam Watras, Rafal J. Wiglusz, *Emission Enhancement and Energy Transfers in $YV_{0.5}P_{0.5}O_4$ Nanoparticles Codoped with Eu^{3+} and Bi^{3+} Ions*, Inorganic Chemistry, 2022, 61, 12237-12248, 10.1021/acs.inorgchem.2c01465. **(P4)**
10. Wojciech M. Piotrowski, **Marta Kardach**, Paulina Sobierajska, Adam Watras, John M. Reeks, Vasyl Kinzhybalo, Lukasz Marciniak, Rafal J. Wiglusz, *Tunable luminescence thermal stability in $YV_xAs_{1-x}O_4:Eu^{3+}$ through the introduction of As^{5+} ions for remote temperature sensing applications*, Journal of Materials Chemistry C, Journal of Materials Chemistry C, 2023, 10.1039/D2TC03909E.

Participation in scientific conferences

1. Presenting author
    a. Oral speech – *12th International Conference on Excited States of Transitions Elements*, 8–13 September 2019, Kudowa Zdroj, Poland, *Investigation of $YV_xAs_{1-x}O_4$ solid state solution for terbium quenching mechanism*, M. Wujczyk, A. Watras, P. Boutinaud, M. Bettinelli, S. Targonska, R. J. Wiglusz.
    b. Poster – *8th International Symposium on Optical Materials*, June 9–14, 2019, Wroclaw, Poland, *The study of the structural and spectroscopic properties of nano-sized YVO_4 doped with Eu^{3+} ions obtained at different pH values*, M. Wujczyk, A. Watras, R. J. Wiglusz.
    c. Oral speech – *PHOBIA ANNUAL NANOPHOTONICS INTERNATIONAL COFERENCE PANIC 2020*, 12–14 October 2020, *Influence of Vanadium(V) Concentration on Up-conversion Luminescence in $YV_xP_{1-x}O_4$ Co-Doped with Er^{3+}-Yb^{3+} and Tm^{3+}-Yb^{3+} Ions*, M. Wujczyk, A. Watras, K. Szyszka and R. J. Wiglusz.

d. Poster – *Open Readings 2022*, 15–18 March 2022, *Emission Enhancement by energy transfer in $YP_{0.5}V_{0.5}O_4$: Bi^{3+}, Eu^{3+}*, M. Wujczyk, S. Targonska, P. Boutinaud, A. Watras, R. J. Wiglusz.

e. Oral speech – *1st International Conference on Advanced Materials for Bio-Related Applications*, AMBRA, 16–19 May 2022, Wroclaw, Poland, *Spectroscopic Investigation of Biocompatible Bismuth(III) and Europium(III) Doped Yttrium Orthovanadate-phosphate*, M. Wujczyk, S. Targonska, N. Nowak, P. Boutinaud, J. M. Reeks, A. Watras, R. J. Wiglusz.

2. Co-author

a. Oral speech – *8th International Workshop on Photoluminescence in Rare Earths: Photonic Materials and Devices*, 4–6 September 2019, Nice, France, *Spectroscopic investigation of the $YV_xAs_{1-x}O_4$ doped with Tb^{3+} ions*, M. Wujczyk, A. Watras, P. Boutinaud, M. Bettinelli and R.J. Wiglusz.

b. Poster – *51. Ogólnopolska Szkoła Chemii*, Wroclaw, November 2019, *Jak z promieniowania NIR może powstać promieniowanie VIS, czyli o zjawiskach konwersji energii w górę w nanomateriałach*, P. Nowakowska, M. Wujczyk, A. Watras, R. J. Wiglusz.

c. Poster – *Photoluminescence in rare earth doped materials*, PRE'22, 11–14 September 2022, Szczawnica, Poland, *Luminescence properties of YVO_4 nanoparticles co-doped with Eu^{3+} and Sb^{3+} ions*, J. M. Reeks, M. Wujczyk, P. Sobierajska, A. Patej, A. Watras, R. J. Wiglusz.

Education

- 2013 – 2017 – Bachelor of Science at Wroclaw University of Science and Technology, field of study: *Chemistry*, major: *Chemical Technology*, research: *Chromatographic analysis of natural triglycerides.*
- 2017 – 2018 – Master of Science at the Wroclaw University of Science and Technology, field of study: *Materials Engineering*, major: *Advanced Functional Materials*, research: *Synthesis and investigation of the spectroscopic properties of KYP_2O_7 pyrophosphate co-doped with Er^{3+} and Yb^{3+} ions.*

- 2018 – present – Doctoral Studies at the Wlodzimierz Trzebiatowski Institute of Low Temperature and Structural Research, Polish Academy of Sciences in Wroclaw, field of study: *Chemistry*, major: *Multidisciplinary doctoral studies – nanotechnology in biomedicine*, research: *Preparation and investigation of spectroscopic properties of $YXZO_4$, where X and Z – P^{5+}, V^{5+}, As^{5+}, doped with rare-earth ions and co-doped with s^2 type ions*.

Research projects

1. Fellowship in the project*, Multidisciplinary doctoral studies – nanotechnology in biomedicine*, contract no. with the National Centre for Research and Development: POWR.03.02.00-00-I030/17-00, co-financed by the European Union.
2. Fellowship in the project*, Preparation and modulation of spectroscopic properties of $YXZO_4$, where X and Z – P^{5+}, V^{5+}, As^{5+}, doped with 's^2-like' ions and co-doped with rare earth ions*, OPUS 17, contract no. UMO-2019/33/B/ST5/02247.
3. Fellowship in the project*, Preparation and characterization of biocomposites based on nanoapatites for theranostic,* OPUS 10, contract no. UMO-2015/19/B/ST5/01330.

Training courses

1. *Cryptosporidium spp. – transmission, detection and identification*, 4th International Forum on Medical and Veterinary Parasitology at the Institute of Genetics and Microbiology, University of Wroclaw, led by prof. Martin Kvać of the Institute of Parasitology, Biology Centre of the AS CR, Ceske Budejovice.
2. December 10th, 2021 – *Protection of inventions in Poland and worldwide*.
3. *Scientific research methodology and commercialization of results*:
    a. December 6th–7th 2021, *Leadership.*
    b. December 9th, 2021, *Public speaking.*
    c. February 1st, 2022, *Disciplined entrepreneurship.*
    d. February 28th, 2022, *Research methods for nano and micromaterials - IR and Raman.*
4. September 5th–23rd 2022, Internship at StemCells Spin S.A.

5. December 5th–17th 2022, Scientific trip to Université Clermont Auvergne, Clermont Auvergne INP, CNRS, ICFC, F-63000 Clermont-Ferrand, France, for spectroscopic studies of $YZXO_4$ systems where Z and X are P^{5+}, V^{5+} and As^{5+} doped with and co-doped with RE^{3+} ions and ns^2 ions.

Prizes

1. Scholarship for the best doctoral students of the Institute of Low Temperature and Structural Research, Polish Academy of Sciences in Wroclaw for the academic year:
    a. 2019/2020.
    b. 2021/2022.
2. Distinction of the oral presentation entitled *Spectroscopic Investigation of Biocompatible Bismuth(III) and Europium(III) Doped Yttrium Orthovanadate-phosphate* during *the 1st International Conference on Advanced Materials for Bio-Related Applications*, AMBRA, 16–19 May 2022, Wroclaw, Poland.

Patent applications

1. Co-authorship in the invention and preparation of the invention description, entitled *Tissue filler formulation for aesthetic medicine*.

Summary

Researchers in the field of spectroscopy are constantly looking for luminophores with the best possible luminescent properties, in particular high quantum efficiency. The yttrium orthovanadates and yttrium orthophosphates are thoroughly researched for their structural and spectroscopic properties due to good chemical, physical and mechanical properties. Therefore, they find applications in many branches of science. However, some aspects are still unresolved and unsystematised. These compounds belong to the group of materials with the general formula $REXO_4$. This group of compounds also includes yttrium orthoarsenate. The scientific interest concerning yttrium orthoarsenate was the highest between 1960 and 1990. Since then, no more than ten scientific publications have been published, and less than half of them focus on YAsO4 as a luminescent material. The materials crystallize in the same crystal system, space and point group. The difference between these materials becomes apparent in the size of the elementary cell. Therefore, it is possible to obtain a continuous solid solution, for example, from $YAsO_4$ to YVO_4. The physicochemical properties of such solid solutions are not known to the extent that their components are, for example, yttrium orthophosphate.

In this dissertation, with the special attention structural and spectroscopic properties of $YXZO_4$ solid solutions, doped rare earth ions and s^2-type ions were analysed. In each article, to synthesise the materials, the co-precipitation was used. Employing measurement techniques such as XRD, SEM, TEM, and ICP-OES allowed the crystallographic structure, morphology, and elemental composition to be determined. The spectroscopic measurements allowed for the precise determination of the occurring mechanisms, the influence of the matrix composition and the synthesis conditions on the luminescence properties at room and low temperatures.

The dissertation includes four scientific publications. Designed and conducted studies provide information on the processes and dependencies occurring in solid solutions of $YXZO_4$-type materials doped with RE^{3+} (Eu^{3+}, Tb^{3+}, Er^{3+}, Yb^{3+}, Tm^{3+}) and s^2-type (Bi^{3+}) ions. An additional aim of the papers presented in the thesis is to respond to the challenges of science and to provoke further research theses in the area of $YXZO_4$-type compounds.

Streszczenie

Naukowcy z dziedziny spektroskopii nieustannie poszukują luminoforów o jak najlepszych właściwościach luminescencyjnych, w szczególności o wysokiej wydajności kwantowej. Ortowanadany i ortofosforany itru należą do materiałów poznanych pod względem właściwości strukturalnym oraz spektroskopowych ze względu na dobre właściwości chemiczne, fizyczne i mechaniczne. Stąd też znajdują zastosowanie w wielu gałęziach nauki. Jednak niektóre zagadnienia pozostają wciąż nie rozwiązane i nie usystematyzowane. Te związki zaliczyć można do grupy materiałów o ogólnym wzorze $REXO_4$. Do grupy wspomnianych związków należy również ortoarsenian itru. Największe zainteresowanie naukowców ortoarsenianem itru przypadło na lata 1960-1990. Od tamtego czasu wydanych zostało nie więcej niż dziesięć publikacji naukowych, z których mniej niż połowa skupia uwagę na zastosowaniu $YAsO_4$ jako materiału luminescencyjnego. Wymienione substancje krystalizują w tym samym układzie krystalograficznym, grupie przestrzennej i grupie punktowej. Różnica pomiędzy nimi uwidacznia się rozmiarze komórki elementarnej. Możliwe zatem jest otrzymanie roztworu stałego przechodzącego w sposób ciągły, na przykład od $YAsO_4$ do YVO_4. Właściwości fizykochemiczne tak powstałych roztworów stałych nie są poznane w stopniu odpowiadającym ich składnikom, na przykład ortofosforanowi itru.

W pracy doktorskiej szczególna uwaga poświęcona została analizie właściwości strukturalnych oraz spektroskopowych jonów ziem rzadkich oraz jonów typu s^2 domieszkujących roztwory stałe ortoarsenianu itru, ortowanadanu itru oraz ortofosforanu itru. Materiały każdorazowo zostały zsyntezowane z zastosowaniem metody współstrąceniowej. Za pomocą technik pomiarowych takich jak: XRD, SEM, TEM oraz ICP-OES określono strukturę krystalograficzną, morfologię, a także potwierdzono skład elementarny. Przeprowadzone pomiary spektroskopowe pozwoliły na dokładne określenie zachodzących mechanizmów, wpływu składu matrycy, a także warunków syntezy na właściwości luminescencyjne w temperaturze pokojowej oraz niskiej.

W skład rozprawy doktorskiej wchodzą cztery publikacje naukowe. Zaprojektowane i przeprowadzone badania niosą informację o procesach, i zależnościach zachodzących w roztworach stałych materiałów typu $YXZO_4$ domieszkowanych jonami RE^{3+} (Eu^{3+}, Tb^{3+}, Er^{3+}, Yb^{3+}, Tm^{3+}) i typu-s^2 (Bi^{3+}). Dodatkowym celem zaprezentowanych w rozprawie artykułów jest odpowiedź na wyzwania nauki, a także prowokowanie stawiania kolejnych tez badawczych w obszarze związków typu $YXZO_4$.

Bibliography

[1] A.T. Aldred, Crystal Chemistry of ABO_4 Compounds, in: Geochemical Behav. Disposed Radioact. Waste, 1984: pp. 305–314. https://doi.org/10.1021/bk-1984-0246.ch018.

[2] A. Strzep, A. Watras, K. Zawisza, P. Boutinaud, R.J. Wiglusz, Forgotten and resurrected chernovite-(Y): $YAsO_4$ doped with Eu^{3+} ions as a potential nanosized luminophore, Inorg. Chem. 56 (2017) 10914–10925. https://doi.org/10.1021/acs.inorgchem.7b01089.

[3] U. Kolitsch, D. Holtstam, Crystal chemistry of $REEXO_4$ compounds (X = P,As, V). II. Review of $REEXO_4$ compounds and their stability fields, Eur. J. Mineral. 16 (2004) 117–126. https://doi.org/10.1127/0935-1221/2004/0016-0117.

[4] A. Brahim, F. Mohamed Mongi, H. Amor, Cerium arsenate, $CeAsO_4$, Acta Crystallogr. Sect. E Struct. Reports Online. 58 (2002) i98–i99. https://doi.org/10.1107/S1600536802018664.

[5] A.K. Pradhan, R.N.P. Choudhary, B.M. Wanklyn, Raman and infrared spectra of YAsO4, Phys. Status Solidi. 139 (1987) 337–345. https://doi.org/10.1002/pssb.2221390134.

[6] H. Lai, A. Bao, Y. Yang, Y. Tao, H. Yang, Y. Zhang, L. Han, UV luminescence property of YPO_4:RE (RE=Ce^{3+}, Tb^{3+}), J. Phys. Chem. C. 112 (2008) 282–286. https://doi.org/10.1021/jp074103g.

[7] A. Tymiński, T. Grzyb, Are rare earth phosphates suitable as hosts for upconversion luminescence? Studies on nanocrystalline $REPO_4$ (RE=Y, La, Gd, Lu) doped with Yb^{3+} and Eu^{3+}, Tb^{3+}, Ho^{3+}, Er^{3+} or Tm^{3+} ions, J. Lumin. 181 (2017) 411–420. https://doi.org/10.1016/j.jlumin.2016.09.028.

[8] B. Kahouadji, L. Guerbous, D.J. Jovanović, M.D. Dramićanin, M. Samah, L. Lamiri, L. Benchallal, M.M. Cincović, Annealing effect on the photoluminescence properties of Ce^{3+} doped YPO_4 nanophosphors, Opt. Mater. (Amst). 91 (2019) 35–41. https://doi.org/10.1016/j.optmat.2019.02.052.

[9] P.C. de Sousa Filho, O.A. Serra, Reverse microemulsion synthesis, structure, and luminescence of nanosized $REPO_4$:Ln^{3+} (RE = La, Y, Gd, or Yb, and Ln = Eu, Tm, or Er), J. Phys. Chem. C. 115 (2011) 636–646. https://doi.org/10.1021/jp109988a.

[10] Q. Liu, Y. Su, H. Yu, W. Han, YPO_4 nanocrystals: preparation and size-induced lattice symmetry enhancement, J. Rare Earths. 26 (2008) 495–500. https://doi.org/10.1016/S1002-0721(08)60125-8.

[11] L. van Pieterson, M.F. Reid, R.T. Wegh, S. Soverna, A. Meijerink, $4f^n \rightarrow 4f^{n-1}5d$ transitions of the light lanthanides: Experiment and theory, Phys. Rev. B. 65 (2002) 045113. https://doi.org/10.1103/PhysRevB.65.045113.

[12] L. van Pieterson, M.F. Reid, G.W. Burdick, A. Meijerink, $4f^n \rightarrow 4f^{n-1}5d$ transitions of the heavy lanthanides: Experiment and theory, Phys. Rev. B. 65 (2002) 045114. https://doi.org/10.1103/PhysRevB.65.045114.

[13] G. Blasse, A. Bril, Study of energy transfer from Sb^{3+}, Bi^{3+}, Ce^{3+} to Sm^{3+}, Eu^{3+}, Tb^{3+}, Dy^{3+}, J. Chem. Phys. 47 (1967) 1920–1926. https://doi.org/10.1063/1.1712219.

[14] A. Lecointre, A. Bessière, A.J.J. Bos, P. Dorenbos, B. Viana, S. Jacquart, Designing a red persistent luminescence phosphor: the example of YPO_4:Pr^{3+},Ln^{3+} (Ln = Nd, Er, Ho,

Dy), J. Phys. Chem. C. 115 (2011) 4217–4227. https://doi.org/10.1021/jp108038v.

[15] M. Runowski, A. Shyichuk, A. Tymiński, T. Grzyb, V. Lavín, S. Lis, Multifunctional Optical Sensors for Nanomanometry and Nanothermometry: High-Pressure and High-Temperature Upconversion Luminescence of Lanthanide-Doped Phosphates - $LaPO_4/YPO_4:Yb^{3+}$-Tm^{3+}, ACS Appl. Mater. Interfaces. 10 (2018) 17269–17279. https://doi.org/10.1021/acsami.8b02853.

[16] S. Majeed, M. Bashir, S.A. Shivashankar, Dispersible crystalline nanobundles of YPO_4 and Ln (Eu, Tb)-doped YPO_4: rapid synthesis, optical properties and bio-probe applications, J. Nanoparticle Res. 17 (2015) 309. https://doi.org/10.1007/s11051-015-3113-3.

[17] U. Keller, K.J. Weingarten, F.X. Kartner, D. Kopf, B. Braun, I.D. Jung, R. Fluck, C. Honninger, N. Matuschek, J. Aus der Au, Semiconductor saturable absorber mirrors (SESAM's) for femtosecond to nanosecond pulse generation in solid-state lasers, IEEE J. Sel. Top. Quantum Electron. 2 (1996) 435–453. https://doi.org/10.1109/2944.571743.

[18] R.A. Fields, M. Birnbaum, C.L. Fincher, Highly efficient $Nd:YVO_4$ diode-laser end-pumped laser, Appl. Phys. Lett. 51 (1987) 1885. https://doi.org/https://doi.org/10.1063/1.98500.

[19] A.A. Kaminskii, K. Ueda, H.J. Eichler, Y. Kuwano, H. Kouta, S.N. Bagaev, T.H. Chyba, J.C. Barnes, G.M.A. Gad, T. Murai, J. Lu, Tetragonal vanadates YVO_4 and $GdVO_4$ – new efficient $\chi(3)$-materials for Raman lasers, Opt. Commun. 194 (2001) 201–206. https://doi.org/10.1016/S0030-4018(01)01274-3.

[20] J.R. O'Connor, Unusual crystal-field energy levels and efficient laser properties of YVO_4:Nd, Appl. Phys. Lett. 9 (1966) 407–409. https://doi.org/10.1063/1.1754631.

[21] M. Bradler, P. Baum, E. Riedle, Femtosecond continuum generation in bulk laser host materials with sub-μJ pump pulses, Appl. Phys. B. 97 (2009) 561–574. https://doi.org/10.1007/s00340-009-3699-1.

[22] T. Taira, A. Mukai, Y. Nozawa, T. Kobayashi, Single-mode oscillation of laser-diode-pumped $Nd:YVO_4$ microchip lasers, Opt. Lett. 16 (1991) 1955. https://doi.org/10.1364/OL.16.001955.

[23] A.K. Levine, F.C. Palilla, A new, highly efficent red-emitting cathogoluminescent phosphor (YVO_4:Eu) for color television, Appl. Phys. Lett. 5 (1964) 118–120. https://doi.org/10.1063/1.1723611.

[24] P. Yang, S. Huang, D. Kong, J. Lin, H. Fu, Luminescence functionalization of SBA-15 by $YVO_4:Eu^{3+}$ as a novel drug delivery system, Inorg. Chem. 46 (2007) 3203–3211. https://doi.org/10.1021/ic0622959.

[25] J. Shen, L.D. Sun, J.D. Zhu, L.H. Wei, H.F. Sun, C.H. Yan, Biocompatible bright YVO_4:Eu nanoparticles as versatile optical bioprobes, Adv. Funct. Mater. 20 (2010) 3708–3714. https://doi.org/10.1002/adfm.201001264.

[26] L. Chen, K.-J. Chen, C.-C. Lin, C.-I. Chu, S.-F. Hu, M.-H. Lee, R.-S. Liu, Combinatorial approach to the development of a single mass $YVO_4:Bi^{3+},Eu^{3+}$ phosphor with red and green dual colors for high color rendering white light-emitting diodes, J. Comb. Chem. 12 (2010) 587–594. https://doi.org/10.1021/cc100063x.

[27] I.E. Kolesnikov, E. V. Golyeva, A.A. Kalinichev, M.A. Kurochkin, E. Lähderanta, M.D.

Mikhailov, Nd^{3+} single doped YVO_4 nanoparticles for sub-tissue heating and thermal sensing in the second biological window, Sensors Actuators B. 243 (2017) 338–345. https://doi.org/10.1016/j.snb.2016.12.005.

[28] M. Runowski, P. Woźny, S. Lis, V. Lavín, I.R. Martín, Optical vacuum sensor based on lanthanide upconversion—luminescence thermometry as a tool for ultralow pressure sensing, Adv. Mater. Technol. 5 (2020) 1901091. https://doi.org/10.1002/admt.201901091.

[29] M. Puchalska, E. Zych, A. Watras, Cooperative up-conversion processes in $SrAl_4O_7$:Yb and $SrAl_4O_7$:Yb,Tb and their dependence on charge compensation by Na, J. Lumin. 183 (2017) 185–192. https://doi.org/10.1016/j.jlumin.2016.11.022.

[30] H. Zhang, X. Fu, S. Niu, G. Sun, Q. Xin, Photoluminescence of nanocrystalline YVO_4:Tm_xDy_{1-x} prepared by a modified Pechini method, Mater. Lett. 61 (2007) 308–311. https://doi.org/10.1016/j.matlet.2006.04.095.

[31] X. Wu, Y. Tao, C. Song, C. Mao, L. Dong, J. Zhu, Morphological control and luminescent properties of YVO_4:Eu nanocrystals, J. Phys. Chem. B. 110 (2006) 15791–15796. https://doi.org/10.1021/jp060527j.

[32] G. Jia, Y. Song, M. Yang, Y. Huang, L. Zhang, H. You, Uniform YVO_4:Ln^{3+} (Ln=Eu, Dy, and Sm) nanocrystals: Solvothermal synthesis and luminescence properties, Opt. Mater. (Amst). 31 (2009) 1032–1037. https://doi.org/10.1016/j.optmat.2008.11.012.

[33] L. Sun, Y. Zhang, J. Zhang, C. Yan, C. Liao, Y. Lu, Fabrication of size controllable YVO_4 nanoparticles via microemulsion-mediated synthetic process, Solid State Commun. 124 (2002) 35–38. https://doi.org/10.1016/S0038-1098(02)00449-0.

[34] H. Wu, H. Xu, Q. Su, T. Chen, M. Wu, Size- and shape-tailored hydrothermal synthesis of YVO_4 crystals in ultra-wide pH range conditions, J. Mater. Chem. 13 (2003) 1223–1228. https://doi.org/10.1039/b210713a.

[35] S. Zhang, Y. Liang, X.-Y. Gao, H.-T. Liu, Hydrothermal synthesis and microstructural, optical properties characterization of YVO_4 phosphor powder, Acta Phys. Pol. A. 125 (2014) 105–110. https://doi.org/10.12693/APhysPolA.125.105.

[36] F.C. Palilla, A.K. Levine, M. Rinkevics, Rare earth activated phosphors based on yttrium orthovanadate and related compounds, J. Electrochem. Soc. 112 (1965) 776. https://doi.org/10.1149/1.2423693.

[37] F. Kang, X. Yang, M. Peng, L. Wondraczek, Z. Ma, Q. Zhang, J. Qiu, Red photoluminescence from Bi^{3+} and the influence of the oxygen-vacancy perturbation in $ScVO_4$: a combined experimental and theoretical study, J. Phys. Chem. C. 118 (2014) 7515–7522. https://doi.org/10.1021/jp4081965.

[38] L. Vegard, Die konstitution der mischkristalle und die raumfullung der atome, Zeitschrift Phys. Phys. 5 (1921) 17–26. https://doi.org/10.1007/BF01349680.

[39] M.N. Magomedov, On the deviation from the Vegard's law for the solid solutions, Solid State Commun. 322 (2020) 114060. https://doi.org/10.1016/j.ssc.2020.114060.

[40] A.R. Denton, N.W. Ashcroft, Vegard's law, Phys. Rev. A. 43 (1991) 3161–3164. https://doi.org/10.1103/PhysRevA.43.3161.

[41] K.T. Jacob, S. Raj, L. Rannesh, Vegard's law: a fundamental relation or an

approximation?, Int. J. Mater. Res. 98 (2007) 776–779. https://doi.org/10.3139/146.101545.

[42] T. Minakova, S. Mjakin, V. Bakhmetyev, M. Sychov, I. Zyatikov, I. Ekimova, V. Kozik, Y. Chen, I. Kurzina, Highly Efficient $YVPO_4$ Luminescent Materials Activated by Europium, Crystals. 9 (2019) 658. https://doi.org/doi:10.3390/cryst9120658.

[43] G. Pan, H. Song, Q. Dai, R. Qin, X. Bai, B. Dong, L. Fan, F. Wang, Microstructure and optical properties of Eu^{3+} activated $YV_{1-x}P_xO_4$ phosphors, J. Appl. Phys. 104 (2008). https://doi.org/10.1063/1.3003130.

[44] E. Cavalli, F. Angiuli, F. Mezzadri, M. Trevisani, M. Bettinelli, P. Boutinaud, M.G. Brik, Tunable luminescence of Bi^{3+}-doped $YP_xV_{1-x}O_4$ ($0 \leq x \leq 1$), J. Phys. Condens. Matter. 26 (2014) 385503. https://doi.org/10.1088/0953-8984/26/38/385503.

[45] L.A. Kolahalam, I.V. Kasi Viswanath, B.S. Diwakar, B. Govindh, V. Reddy, Y.L.N. Murthy, Review on nanomaterials: Synthesis and applications, Mater. Today Proc. 18 (2019) 2182–2190. https://doi.org/10.1016/j.matpr.2019.07.371.

[46] K. An, G.A. Somorjai, Size and shape control of metal nanoparticles for reaction selectivity in catalysis, ChemCatChem. 4 (2012) 1512–1524. https://doi.org/10.1002/cctc.201200229.

[47] W.P. Halperin, Quantum size effects in metal particles, Rev. Mod. Phys. 58 (1986) 533–606. https://doi.org/10.1103/RevModPhys.58.533.

[48] E. Roduner, Size matters: why nanomaterials are different, Chem. Soc. Rev. 35 (2006) 583. https://doi.org/10.1039/b502142c.

[49] C. Dhand, N. Dwivedi, X.J. Loh, A.N. Jie Ying, N.K. Verma, R.W. Beuerman, R. Lakshminarayanan, S. Ramakrishna, Methods and strategies for the synthesis of diverse nanoparticles and their applications: a comprehensive overview, RSC Adv. 5 (2015) 105003–105037. https://doi.org/10.1039/C5RA19388E.

[50] S. Yáñez-Vilar, M. Sánchez-Andújar, C. Gómez-Aguirre, J. Mira, M.A. Señarís-Rodríguez, S. Castro-García, A simple solvothermal synthesis of MFe_2O_4 (M=Mn, Co and Ni) nanoparticles, J. Solid State Chem. 182 (2009) 2685–2690. https://doi.org/10.1016/j.jssc.2009.07.028.

[51] S. Cimitan, S. Albonetti, L. Forni, F. Peri, D. Lazzari, Solvothermal synthesis and properties control of doped ZnO nanoparticles, J. Colloid Interface Sci. 329 (2009) 73–80. https://doi.org/10.1016/j.jcis.2008.09.060.

[52] P. Rai, H.-M. Song, Y.-S. Kim, M.-K. Song, P.-R. Oh, J.-M. Yoon, Y.-T. Yu, Microwave assisted hydrothermal synthesis of single crystalline ZnO nanorods for gas sensor application, Mater. Lett. 68 (2012) 90–93. https://doi.org/10.1016/j.matlet.2011.10.029.

[53] S. Targonska, K. Szyszka, J. Rewak-Soroczynska, R.J. Wiglusz, A new approach to spectroscopic and structural studies of the nano-sized silicate-substituted hydroxyapatite doped with Eu^{3+} ions, Dalt. Trans. 48 (2019) 8303–8316. https://doi.org/10.1039/C9DT01025D.

[54] M. Parashar, V.K. Shukla, R. Singh, Metal oxides nanoparticles via sol–gel method: a review on synthesis, characterization and applications, J. Mater. Sci. Mater. Electron. 31 (2020) 3729–3749. https://doi.org/10.1007/s10854-020-02994-8.

[55] J.D. Mackenzie, E.P. Bescher, Chemical Routes in the Synthesis of Nanomaterials Using the Sol–Gel Process, Acc. Chem. Res. 40 (2007) 810–818. https://doi.org/10.1021/ar7000149.

[56] Ö.A. Yıldırım, C. Durucan, Synthesis of zinc oxide nanoparticles elaborated by microemulsion method, J. Alloys Compd. 506 (2010) 944–949. https://doi.org/10.1016/j.jallcom.2010.07.125.

[57] L. Song, Y. Dong, Q. Shao, J. Jiang, Preparation of $Y_3Al_5O_{12}$:Ce nanophosphors using salt microemulsion method and their luminescent properties, J. Mater. Sci. 53 (2018) 15196–15203. https://doi.org/10.1007/s10853-018-2623-7.

[58] C.E. Rivera-Enríquez, A. Fernández-Osorio, J. Chávez-Fernández, Luminescence properties of α- and β-Zn_2SiO_4:Mn nanoparticles prepared by a co-precipitation method, J. Alloys Compd. 688 (2016) 775–782. https://doi.org/10.1016/j.jallcom.2016.07.266.

[59] P. Sobierajska, R.J. Wiglusz, Influence of the grain sizes on Stokes and anti-Stokes fluorescence in the Yb^{3+} and Tb^{3+} ions co-doped nanocrystalline fluorapatite, J. Alloys Compd. 785 (2019) 808–818. https://doi.org/10.1016/j.jallcom.2019.01.146.

[60] L. Zhang, Y. Li, Q. Zhang, G. Shi, H. Wang, Fast Synthesis of Highly Dispersed Anatase TiO_2 Nanocrystals in a Microfluidic Reactor, Chem. Lett. 40 (2011) 1371–1373. https://doi.org/10.1246/cl.2011.1371.

[61] S. Cattaneo, S. Althahban, S.J. Freakley, M. Sankar, T. Davies, Q. He, N. Dimitratos, C.J. Kiely, G.J. Hutchings, Synthesis of highly uniform and composition-controlled gold–palladium supported nanoparticles in continuous flow, Nanoscale. 11 (2019) 8247–8259. https://doi.org/10.1039/C8NR09917K.

[62] A. De Bettencourt-Dias, Luminescence of lanthanide ions in coordination compounds and nanomaterials, 2014. https://doi.org/10.1002/9781118682760.

[63] M.S. Tremblay, D. Sames, Synthesis of luminescent heterometallic bis-lanthanide complexes via selective, sequential metallation, Chem. Commun. (2006) 4116. https://doi.org/10.1039/b607949k.

[64] P.A. Tanner, Lanthanide luminescence in solids, 2010. https://doi.org/10.1007/4243_2010_6.

[65] G.H. Dieke, Spectra and Energy Levels of Rare Earth Ions in Crystals, 1968.

[66] P. Hamm, J. Helbing, G. Liu, B. Jacquier, Thermo Spectronic, H.C. Swart, J.J. Terblans, O.M. Ntwaeaborwa, R.E. Kroon, E. Coetsee, I.M. Nagpure, V.V.V. Kumar, V.V.V. Kumar, V.V.V. Kumar, Spectroscopic Properties of Rare Earths in Optical Materials, Springer Science + Susiness Media, 2005. https://doi.org/10.1007/3-540-28209-2.

[67] P. Dorenbos, The $4f \leftrightarrow 4f^{n-1}5d$ transitions of the trivalent lanthanides in halogenides and chalcogenides, J. Lumin. 91 (2000) 91–106. https://doi.org/10.1016/S0022-2313(00)00197-6.

[68] S.J. Dhoble, V.B. Pawade, H.C. Swart, V. Chopra, Spectroscopy of lanthanide doped oxide materials, Woodhead Publishing Series in Electronic and Optical Materials, 2020. https://doi.org/10.1016/C2018-0-02471-8.

[69] J. Lakde, C.M. Mehare, K.K. Pandey, N.S. Dhoble, S.J. Dhoble, Recent development of Eu3+-doped phosphor for white LED application: A review, J. Phys. Conf. Ser. 1913

(2021) 012029. https://doi.org/10.1088/1742-6596/1913/1/012029.

[70] Z. Ju, R. Wei, X. Gao, W. Liu, C. Pang, Red phosphor $SrWO_4:Eu^{3+}$ for potential application in white LED, Opt. Mater. (Amst). 33 (2011) 909–913. https://doi.org/10.1016/j.optmat.2011.01.025.

[71] K. Marycz, P. Sobierajska, A. Smieszek, M. Maredziak, K. Wiglusz, R.J. Wiglusz, Li+ activated nanohydroxyapatite doped with Eu^{3+} ions enhances proliferative activity and viability of human stem progenitor cells of adipose tissue and olfactory ensheathing cells. Further perspective of nHAP:Li^{+}, Eu^{3+} application in theranostics, Mater. Sci. Eng. C. 78 (2017) 151–162. https://doi.org/10.1016/j.msec.2017.04.041.

[72] S.J. Park, J.Y. Kim, J.H. Yim, N.Y. Kim, C.H. Lee, S.J. Yang, H.K. Yang, The effective fingerprint detection application using $Gd_2Ti_2O_7:Eu^{3+}$ nanophosphors, J. Alloys Compd. 741 (2018) 246–255. https://doi.org/10.1016/j.jallcom.2018.01.116.

[73] F. Wang, Y. Zhang, X. Fan, M. Wang, One-pot synthesis of chitosan/$LaF_3:Eu^{3+}$ nanocrystals for bio-applications, Nanotechnology. 17 (2006) 1527–1532. https://doi.org/10.1088/0957-4484/17/5/060.

[74] B.K. Gupta, D. Haranath, S. Saini, V.N. Singh, V. Shanker, Synthesis and characterization of ultra-fine $Y_2O_3:Eu^{3+}$ nanophosphors for luminescent security ink applications, Nanotechnology. 21 (2010) 055607. https://doi.org/10.1088/0957-4484/21/5/055607.

[75] G. Yuan, M. Li, M. Yu, C. Tian, G. Wang, H. Fu, In situ synthesis, enhanced luminescence and application in dye sensitized solar cells of $Y_2O_3/Y_2O_2S:Eu^{3+}$ nanocomposites by reduction of $Y_2O_3:Eu^{3+}$, Sci. Rep. 6 (2016) 37133. https://doi.org/10.1038/srep37133.

[76] X. Zhang, L. Zhou, M. Gong, High-brightness Eu^{3+}-doped $Ca_3(PO_4)_2$ red phosphor for NUV light-emitting diodes application, Opt. Mater. (Amst). 35 (2013) 993–997. https://doi.org/10.1016/j.optmat.2012.12.023.

[77] K. Binnemans, Interpretation of europium(III) spectra, Coord. Chem. Rev. 295 (2015) 1–45. https://doi.org/10.1016/j.ccr.2015.02.015.

[78] R. Wangkhem, T. Yaba, N. Shanta Singh, R.S. Ningthoujam, Red emission enhancement from $CaMoO_4:Eu^{3+}$ by co-doping of Bi^{3+} for near UV/blue LED pumped white pcLEDs: Energy transfer studies, J. Appl. Phys. 123 (2018) 124303. https://doi.org/10.1063/1.5021285.

[79] A.D. Sontakke, A. Tarafder, K. Biswas, K. Annapurna, Sensitized red luminescence from Bi^{3+} co-doped Eu^{3+}: $ZnO–B_2O_3$ glasses, Phys. B Condens. Matter. 404 (2009) 3525–3529. https://doi.org/10.1016/j.physb.2009.05.053.

[80] X.-Q. Su, B. Yan, Matrix-inducing synthesis and luminescence of microcrystalline red phosphors $YVO_4:Pb^{2+},Eu^{3+}$ derived from the in situ coprecipitation of hybrid precursors, Inorg. Mater. 42 (2006) 59–63. https://doi.org/10.1134/S0020168506010122.

[81] R. Reisfeld, N. Lieblich, Energy transfer between Pb^{2+} and Eu^{3+} in germanate glass, J. Electrochem. Soc. 121 (1974) 1338. https://doi.org/10.1149/1.2401682.

[82] N. Bodenschatz, R. Wannemacher, J. Heber, D. Mateika, Electronically resonant optical cross relaxation in YAG: Tb^{3+}, J. Lumin. 47 (1990) 159–167. https://doi.org/10.1016/0022-2313(90)90027-9.

[83] K.-S. Sohn, Y.Y. Choi, H.D. Park, Y.G. Choi, Analysis of Tb^{3+} luminescence by direct transfer and migration in YPO_4, J. Electrochem. Soc. 147 (2000) 2375. https://doi.org/10.1149/1.1393539.

[84] V. Singh, A.R. Kadam, S.J. Dhoble, H. Jeong, VUV and UV photoluminescence of green emitting $Sr_2P_2O_7:Tb^{3+}$ phosphors for PDP applications, Optik (Stuttg). 243 (2021) 167396. https://doi.org/10.1016/j.ijleo.2021.167396.

[85] R.R.F. Fonseca, R.D.L. Gaspar, I.M. Raimundo, P.P. Luz, Photoluminescent Tb^{3+}-based metal-organic framework as a sensor for detection of methanol in ethanol fuel, J. Rare Earths. 37 (2019) 225–231. https://doi.org/10.1016/j.jre.2018.07.006.

[86] J.-X. Wu, B. Yan, Luminescent hybrid Tb^{3+} functionalized metal–organic frameworks act as food preservative sensor and water scavenger for NO_2^-, Ind. Eng. Chem. Res. 57 (2018) 7105–7111. https://doi.org/10.1021/acs.iecr.8b00762.

[87] M. Yamazaki, Y. Yamamoto, S. Nagahama, N. Sawanobori, M. Mizuguchi, H. Hosono, Long luminescent glass: Tb^{3+}-activated $ZnO-B_2O-SiO_2$ glass, J. Non. Cryst. Solids. 241 (1998) 71–73. https://doi.org/10.1016/S0022-3093(98)00775-3.

[88] X. Sun, M. Gu, S. Huang, X. Jin, X. Liu, B. Liu, C. Ni, Luminescence behavior of Tb^{3+} ions in transparent glass and glass-ceramics containing CaF_2 nanocrystals, J. Lumin. 129 (2009) 773–777. https://doi.org/10.1016/j.jlumin.2009.02.017.

[89] K. Rawat, A.K. Vishwakarma, K. Jha, Thermally stable $Ca_2Ga_2SiO_7:Tb^{3+}$ green emitting phosphor for tricolor w-LEDs application, Mater. Res. Bull. 124 (2020) 110750. https://doi.org/10.1016/j.materresbull.2019.110750.

[90] G. Blasse, B.C. Grabmaier, Luminescent Materials, Springer-Verlag, 1994. https://doi.org/10.1017/CBO9781107415324.004.

[91] D. Li, H. Ågren, G. Chen, Near infrared harvesting dye-sensitized solar cells enabled by rare-earth upconversion materials, Dalt. Trans. 47 (2018) 8526–8537. https://doi.org/10.1039/C7DT04461E.

[92] A.A. Setlur, A.M. Srivastava, The nature of Bi^{3+} luminescence in garnet hosts, Opt. Mater. (Amst). 29 (2006) 410–415. https://doi.org/10.1016/j.optmat.2005.09.076.

[93] G. Boulon, B. Moine, J.C. Bourcet, R. Reisefeld, Y. Kalisky, Time resolved spectroscopy about $^3P_1$ and $^3P_0$ levels in Bi^{3+} doped germanate glasses, J. Lumin. 18–19 (1979) 924–928. https://doi.org/10.1016/0022-2313(79)90265-5.

[94] C.W.M. Timmermans, G. Blasse, The luminescence of some oxidic bismuth and lead compounds, J. Solid State Chem. 52 (1984) 222–232. https://doi.org/10.1016/0022-4596(84)90005-7.

[95] P. Boutinaud, Revisiting the spectroscopy of the Bi^{3+} ion in oxide compounds, Inorg. Chem. 52 (2013) 6028–6038. https://doi.org/10.1021/ic400382k.

[96] H.T.-D. Z. Trzaska-Durski, Podstawy krystalografii strukturalnej i rentgenowskiej, Wydawnictwo Naukowe PWN, Warszawa, 1994.

[97] C.Y. Tang, Z. Yang, Transmission Electron Microscopy (TEM), in: Membr. Charact., Elsevier, 2017: pp. 145–159. https://doi.org/10.1016/B978-0-444-63776-5.00008-5.

[98] V.A. Fassel, R.N. Kniseley, Inductively coupled plasma. Optical emission spectroscopy, Anal. Chem. 46 (1974) 1110A-1120a. https://doi.org/10.1021/ac60349a023.

[99] L.M. Ng, R. Simmons, Infrared Spectroscopy, Anal. Chem. 71 (1999) 343–350. https://doi.org/10.1021/a1999908r.

[100] B.H. Stuart, Infrared spectroscopy: fundamentals and applications, John Wiley & Sons, 2004.

[101] G. Blasse, A. Bril, Photoluminescent Efficiency of Phosphors with Electronic Transitions in Localized Centers, J. Electrochem. Soc. 115 (1968) 1067. https://doi.org/10.1149/1.2410880.

[102] G. Jia, P.A. Tanner, C.-K. Duan, J. Dexpert-Ghys, Eu^{3+} spectroscopy: a structural probe for yttrium orthoborate phosphors, J. Phys. Chem. C. 114 (2010) 2769–2775. https://doi.org/10.1021/jp910329k.

[103] S. Takeshita, T. Isobe, S. Niikura, Low-temperature wet chemical synthesis and photoluminescence properties of YVO_4: Bi^{3+}, Eu^{3+} nanophosphors, J. Lumin. 128 (2008) 1515–1522. https://doi.org/10.1016/j.jlumin.2008.02.012.